Rui António Henrique Fernandes da Rocha

Image segmentation and reconstruction of 3D surfaces from carotid ultrasound images.

Tese submetida à
Faculdade de Engenharia da Universidade do Porto
para a obtenção do grau de
Doutor em Engenharia Electrotécnica e de Computadores

Dissertação realizada sob a supervisão do
Professor Doutor Aurélio Joaquim de Castro Campilho
e do Professor Doutor Jorge Alves da Silva
Departamento de Engenharia Electrotécnica e de Computadores
Faculdade de Engenharia da Universidade do Porto

Julho de 2007

Dedicated to my family

ACKNOWLEDGMENTS

The author would like to thank:

Dr. Elsa Azevedo and Dr. Rosa Santos, from the Faculty of Medicine of the Hospital de S. João do Porto, for providing most of the images and the manual segmentations used to validate the results.

Dr. Gabriela Lopes from the SMIC (Serviço Médico de Imagem Computorizada), for some of the images used in this work.

Professor João Sanches and Master José Seabra, from the Department of Electrical and Computer Engineering of the Instituto Superior Técnico de Lisboa, for sharing a few 3D volumes.

Professor Aaron Fenster, from the Imaging Research Laboratories, Robarts Research Institute, London, Ontario, Canada, for sharing one of the used 3D volumes.

The Division of Signal and Image of the INEB (Instituto de Engenharia Biomédica) of the University of Porto, for providing the material conditions to do the work.

My supervisors, Professor Aurélio Campilho and Professor Jorge Alves da Silva, from the Department of Electrical and Computer Engineering of the Faculty of Engineering of the University of Porto, for their friendship, guidance, support and inspiration.

ABSTRACT

A new algorithm is proposed for the automatic segmentation of the common carotid wall in ultrasound images. It uses the random sample consensus (RANSAC) method to estimate the most significant cubic splines or ellipses fitting the edge map of a longitudinal or a transversal section, respectively. Periodic spline fitting is also investigated for transversal sections. The geometric model (spline or ellipse) consensus is evaluated through a new gain function, which integrates the responses to different discriminating characteristics of the carotid boundary: the proximity of the geometric model to any edge pixel and to valley shaped edge pixels; the consistency between the orientation of the normal to the geometric model and the intensity gradient; and the distance to a rough estimate of the lumen boundary.

To obtain an edge map with reduced noise and a good localization of the edges, a new robust non-linear smoothing filter was conceived. It preserves weaker intensity edges if they have low curvature, which is a common characteristic of anatomical structures. The smoothing filter combines the image curvature with an edge detector, known as the instantaneous coefficient of variation (ICOV), more suited to ultrasound imaging than the intensity gradient norm. Robust statistics methods are used to improve the automatic stopping of the smoothing and to produce sharper boundaries.

For the detection of the lumen boundary, a new dynamic programming model was conceived for longitudinal sections and adapted to transversal sections, where the boundary is a closed curve. It looks for the path that maximizes the accumulated ICOV strength, previously normalized in the direction normal to the lumen axis. A hybrid geometric active contour is also introduced. It uses a smooth thresholding surface and the image intensity topology to reduce some segmentation errors, left by the dynamic programming algorithm, and to guide the smoothing of the detected lumen boundary.

A new approach and several implementation details are investigated for the automatic reconstruction of 3D surfaces of the common carotid. The surfaces are computed from the wall and lumen boundary contours segmented in each frame of a data set acquired with a 3D ultrasound freehand system.

A level set algorithm is proposed for the computation of new slices from the reconstructed 3D surfaces. A cross sectional area minimization approach is introduced to compute reliable estimates of slices normal to the longitudinal axis of the carotid artery.

Statistics for the segmentation results are computed for each case, using an image data base manually segmented by a medical expert as the ground truth.

RESUMO

Um novo algoritmo é proposto para a segmentação automática da parede da carótida comum em imagens de ultrasons. Este usa o método do consenso de amostra aleatória (RANSAC-random sample consensus) para estimar os splines cúbicos ou as elipses com ajuste mais significativo ao mapa de contornos de uma secção longitudinal ou transversal, respectivamente. O ajuste de splines periódicos é também investigado para secções transversais. O consenso do modelo geométrico (spline ou elipse) é avaliado através de uma nova função de ganho, que integra as respostas a diferentes características discriminantes da fronteira da carótida: a proximidade do modelo geométrico de qualquer pixel de contorno e de pixels de contornos com forma de vale; a consistência entre a orientação da normal ao modelo geométrico e o gradiente de intensidade; e a distância a uma estimativa grosseira da fronteira do lúmen.

Para obter um mapa de contornos com ruído reduzido e uma boa localização dos contornos, foi concebido um novo e robusto filtro não linear de suavização. Este preserva contornos de intensidade mais fraca se tiverem baixa curvatura, uma característica comum de estruturas anatómicas. O filtro de suavização combina a curvatura da imagem com um detector de contornos, conhecido por coeficiente de variação instantânea (ICOV-instantaneous coefficient of variation), mais adequado a imagens de ultrasons do que a norma do gradiente de intensidade. São usados métodos de estatística robusta para melhorar a paragem automática da suavização e para produzir fronteiras de maior contraste.

Para a detecção da fronteira do lúmen, foi concebido um novo modelo de programação dinâmica para secções longitudinais e adaptado para secções transversais, onde a fronteira é uma curva fechada. O algoritmo procura o caminho que maximiza o valor acumulado do ICOV, previamente normalizado na direcção normal ao eixo do lúmen. Um contorno geométrico híbrido é também introduzido. Este usa uma superfície suave de limiarização e a topologia da intensidade da imagem para reduzir alguns erros de segmentação, deixados pelo algoritmo de programação dinâmica, e para guiar a suavização da fronteira do lúmen detectada.

Uma nova abordagem e diversos detalhes de implementação são investigados para a reconstrução automática de superfícies 3D da carótida comum. As superfícies são calculadas a partir dos contornos da parede da carótida e da fronteira do lúmen segmentados em cada imagem do conjunto de dados adquirido com um sistema de ultrasons 3D de mãos livres.

É proposto um algoritmo baseado em conjuntos de nível para o cálculo de novas fatias a partir das superfícies 3D reconstruídas. Uma abordagem de minimização da

área transversal é introduzida para calcular estimativas fiáveis de fatias normais ao eixo longitudinal da artéria da carótida.

São calculadas estatísticas para os resultados da segmentação, para cada caso, usando como referência uma base de dados de imagens segmentadas manualmente por um médico especialista.

RÉSUMÉ

Un algorithme nouveau est proposé pour la segmentation de la carotide commune sur images ultrasonores. On utilise la méthode du consensus à échantillons aléatoires (RANSAC-Random Sample Consensus) pour estimer la courbe spline cubique ou l'ellipse qui est adaptée à carte des contours détectés sur une coupe longitudinale ou transversale, respectivement. Le consensus du modèle géométrique (spline ou ellipse) est évalué à travers d'une nouvelle fonction de gain qui intègre les réponses à différentes caractéristiques discriminantes de la frontière de la carotide: la proximité du modèle géométrique à quelqu'un pixel du contour et aux pixels qui restent en vallées, la consistance entre l'orientation de la normale au modèle géométrique et le gradient des niveaux de gris, et la distance à une approximation grossière de la frontière du lumen.

Pour obtenir une carte de contours avec moins de bruit et une localisation précise des contours, nous avons conçu un nouveau filtre de lissage non-linéaire. Il préserve les contours les plus faibles s'ils ont une courbature réduite, qui est une caractéristique commune des structures anatomiques. Le filtre de lissage combine la courbature de l'image avec un détecteur de contours, connu par coefficient de variation instantanée (ICOV-Instantaneous Coefficient of Variation). Méthodes de la statistique robuste sont utilisées pour améliorer le critère d'arrêt du lissage et la netteté des contours.

Pour la détection de la frontière du lumen, un nouveau modèle de programmation dynamique a été conçu pour les coupes longitudinales et il fut adapté aux coupes transversales, ou la frontière est une courbe fermée. Il cherche le chemin dont la force accumulée de l'ICOV, normalisée auparavant dans la direction normale à l'axe du lumen, est maximale. Il use une surface de seuillage lisse et la topologie des niveaux de gris de l'image pour réduire quelques erreurs de segmentation, dues à l'algorithme de programmation dynamique, et pour guider le lissage de la frontière du lumen détectée.

Une nouvelle approche et plusieurs détails d'implémentation sont explorés pour la reconstruction automatique de la surface 3D de la carotide commune. Les surfaces sont calculées à partir des frontières de la carotide e du lumen, obtenues par segmentation de chacune des images d'un ensemble obtenu avec un système d'échographie 3D mode main-livre.

An algorithme basé sur la méthode d'ensembles de niveau zéro (level sets) est proposé pour déterminer de nouveaux coupes sur les surfaces reconstruites. Une approche de minimisation de l'aire de la coupe transversale est introduite pour obtenir des estimations fiables de coupes normales à l'axe longitudinal de l'artère

carotide.

Mesures statistiques des résultats de la segmentation sont calculées, ayant comme référence un ensemble d'images qui ont été segmentées manuellement par un médecin spécialiste.

LIST OF ABBREVIATIONS

2D	-	Two dimensional
3D	-	Three dimensional
A-mode	-	Amplitude mode
B-mode	-	Brightness mode
CCA	-	Common carotid artery
CT	-	Computer Tomography
CVA	-	Cerebrovascular accident
DP	-	Dynamic programming
ECA	-	External carotid artery
GDM	-	Geometric deformable model
GVF	-	Gradient vector flow
ICA	-	Internal carotid artery
ICOV	-	Instantaneous coefficient of variation
IMT	-	Intima-media thickness
IVUS	-	Intravascular ultrasound
LMCE	-	Local minimum cross entropy
MAD	-	Median absolute deviation
MCE	-	Minimum cross entropy
MRI	-	Magnetic Resonance Imaging
PDE	-	Partial differential equation
PET	-	Positron Emission Tomography
RANSAC	-	Random sample consensus
ROI	-	Region of interest
SDL	-	Signed distance to the lumen boundary
SEM	-	Stochastic expectation-maximization
SMCE	-	Sequential minimum cross entropy
TV	-	Total variation

LIST OF FIGURES

CONTENTS

Chapter 1

INTRODUCTION

1.1 Motivation

The diagnosis of atherosclerosis is one of the most important medical exams for the prevention of cardiovascular events, like myocardial infarction and stroke [1, 2].

A good way to make this diagnosis is the B-mode ultrasound imaging of the carotid artery, with the advantage of requiring a cheaper technology and a much safer procedure for the patient than alternative methods, like X-ray angiography or intravascular ultrasound (IVUS). However, B-mode medical images have very poor quality, which makes them a huge challenge for automatic segmentation. In the particular case of the carotid examination, additional difficulties arise, like the possible presence of plaques in diseased vessels. Despite some previous attempts [3–11], there is still no standard procedure for the automatic detection of the carotid boundaries in B-mode images. Therefore, they have to be manually segmented by a specialist, which is time consuming and prone to subjective segmentation results.

The recent 3D ultrasound systems offer a more powerful analysis and can reveal pathologies that could be missed in a single 2D image [12]. The 3D data may be acquired with a 3D ultrasound freehand system, which is very flexible and cheaper than other 3D systems. In freehand systems, the pixels of the set of acquired B-scans are not uniformly distributed in space. This 3D data set may be interpolated onto a regular voxel array, but there are several important advantages in performing the segmentation directly in the individual 2D B-scans. For instance, B-scans are easier to interpret by medical doctors and have better quality than the interpolated 3D voxel arrays, thus allowing better segmentations and easier correction by the specialist [12]. Afterwords, the 3D surfaces can be reconstructed from the carotid boundaries segmented in each frame of the image set.

These facts explain the great interest and increasing effort, manifested by the scientific community in the last years, in the development of algorithms for the

automatic segmentation of carotid B-mode ultrasound images.

1.2 Aims

The main purpose of this work is to develop algorithms for:

1. the automatic segmentation of the carotid wall and lumen boundaries, in ultrasound B-mode images;

2. the automatic reconstruction of the 3D surfaces of the carotid wall and lumen boundary from sequences of previously segmented B-mode images, acquired with 3D ultrasound freehand systems.

1.3 Contributions

Several new algorithms are introduced for the automatic segmentation of the common carotid wall and lumen boundary, in B-mode images, as well as for the automatic reconstruction of the corresponding 3D surfaces, in particular:

1. A complete new approach for the automatic detection of the common carotid wall boundary, based on a RANSAC search of the best fit of a contour prior in the carotid image. The integration of global constraints makes it more powerful and more robust to noise than other published approaches that use local constraints.

2. A non-linear smoothing filter for ultrasound images that combines the ICOV (instantaneous coefficient of variation) edge detector with the local intensity curvature, producing better preservation of important edges than previously published filters.

3. An ICOV based dynamic programming model for the detection of the lumen boundary in longitudinal sections of the carotid, as well as its adaptation to transversal sections, where the boundary is a closed curve.

4. A hybrid geometric active contour, which uses a smooth thresholding surface and the image intensity topology to: reduce some errors left by the dynamic programming segmentation; guide the smoothing of the detected boundary.

5. Several new implementation details in the reconstruction of 3D surfaces, related to the alignment of the contours segmented in the B-scans and to the smoothing of the obtained surfaces.

6. A level set algorithm for the computation of new slices directly from the reconstructed 3D surfaces.

7. A cross sectional area minimization approach to obtain reliable estimates of surface slices normal to the carotid longitudinal axis, which are important to compute 3D measures of the blood vessel.

Some work related to the segmentation of the carotid lumen in B-mode images was published in [13].

1.4 Overview of the thesis

Chapter 2 makes a brief introduction to current ultrasound medical imaging technology, with focus on 2D imaging of the carotid artery and 3D freehand systems. It also includes a short description of atherosclerosis and discusses its diagnosis with ultrasound imaging of the carotid.

Chapter 3 gives a picture of the state of the art in automatic segmentation methodologies for ultrasound medical imaging. Their main areas of application are also referred. Specific ultrasound image properties and processing difficulties are brought to light, as well as the most successful methods used to deal with them. Both 2D and 3D approaches are analyzed, with focus on applications to the detection of atherosclerosis in B-scans of the carotid.

A detailed presentation of the proposed segmentation algorithms, for the automatic detection of the carotid wall and lumen boundary in B-mode images, is given in chapters 4 and 5, respectively. In both cases, several statistical results are given for the quantitative assessment of the segmentation performance, using as ground truth a set of images manually segmented by a medical expert.

Algorithms for the reconstruction of 3D surfaces from previously segmented B-scans are presented in chapter 6. Here, the problem of reslicing the obtained 3D surfaces is also discussed and new algorithms are proposed for this task. Examples of 3D measures of lumen stenosis and plaque area are given and tested with real 3D data sets.

Finally, in chapter 7, some conclusions are presented and topics for future research are suggested.

Chapter 2

ULTRASOUND IMAGING

Ultrasound imaging has been used in medical diagnosis for many years [14]. Recent improvements in ultrasound image resolution have strongly increased the interest of clinicians in this medical imaging modality. It is becoming a very common alternative to other imaging modalities that offer better quality images at the cost of much more expensive equipment and higher risk to the patient [12].

Ultrasound signals are sound vibrations with frequencies above 20 kHz. In vascular diagnosis, ultrasound signals have frequencies between 1 and 20 MHz [14].

In ultrasound image acquisition systems, a transducer is used to transform electronic signals into acoustic waves, and vice-versa, according to the piezoelectric principle. The transducer transmits acoustic waves in the direction of the tissues of interest and receives the echoes of the signals from different tissue structures at different depths. The resolution of the image is proportional to the frequency of the signal [14].

Ultrasound medical imaging relies on different acoustic impedances of adjacent anatomical tissues. The impedance of a medium is its resistance to the propagation of the signal, and is defined as the product of the propagation speed by the density of the medium. The echo signal received at the transducer depends on the propagation speed of the sound wave in each tissue and on their reflective and scattering properties [14].

The sound velocity depends on the medium in which it propagates. In soft human tissue the average speed is 1540 m/s [14].

A reflection of the acoustic signal occurs at smooth interfaces between mediums with different impedances. A part of the incident signal is transmitted to the next medium and another part is reflected back. The reflection is stronger for a large angle of incidence of the signal and for large differences in the impedances of the two adjacent mediums. A perpendicular angle gives the best reflection. Some well-reflecting media (e.g., air, bone and calcified tissue) can induce total reflection,

causing acoustic shadows beneath them [14].

At rough interfaces between the media, a part of the signal is reflected in several directions, a phenomenon known as backscattering that is very important in the detection of many tissues, like blood cells [14].

Acoustic signals also suffer attenuation during their propagation in a medium. The attenuation gets stronger with increasing medium depth and signal frequency. An even image over the entire imaging depth can be obtained by appropriate instrument adjustments. However, the electronic amplification of the echo signal cannot be too high because it also increases the noise [14].

The backscattered signals produced by irregular surfaces arrive at the receiver with small time differences, resulting in interference noise between the received signals [15]. This noise, known as speckle, affects the amplitude of the received signal and has multiplicative nature. Its statistical distribution depends on the number of scatterers [15, 16].

2.1 A-mode

Ultrasound imaging is based on the pulse-echo technique, consisting in the emission of short bursts of ultrasound waves (pulses) and the subsequent reception of the reflected and scattered echoes. The time between the transmission of the pulse and the reception of the echo is called pulse-echo cycle and is used to determine the distance of the echo source to the transmitter [14].

In A-mode ultrasonography, the amplitude (A) of the echo is displayed as a function of time.

2.2 B-mode

In B-mode images, the probe contains several piezoelectric elements, each of which generates an ultrasound pulse. The amplitudes of the received echoes are then rendered as levels of brightness (B) in a 2D gray scale image, like the one in Fig. 2.1.

The best B-mode images are acquired with perpendicular incidence of the pulses, which is the optimum angle of reflection. Its resolution depends on the number of piezoelectric elements in the probe and on the operating frequency [14].

The construction of B-mode images involves some image filtering and logarithmic compression of the intensity dynamic range [15], which affects the statistical

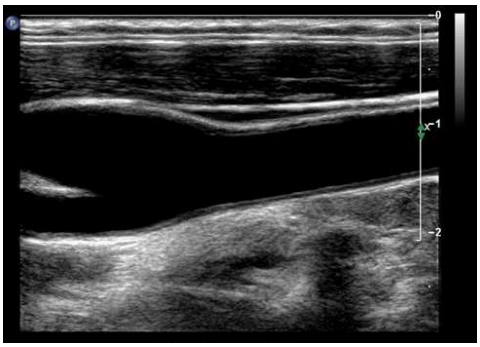

Fig. 2.1: B-mode ultrasound image.

distribution of the noise. In these images, speckle noise appears in the form of small granularities, with approximately regular spatial distribution [17].

2.3 Eco-Doppler techniques

Echo-Doppler imaging is the standard technique used in clinical practice to study the dynamics of the blood in the lumen of vessels.

Doppler sonography is based on the doppler effect, which states that the frequency of a received acoustic signal depends on the moving direction and speed of the source. The frequency of the received signal is lower or higher than the transmitted signal if the source is moving away or toward the receiver, respectively. The frequency shift is proportional to the speed of the source [14].

Color-coded duplex sonography techniques are very useful in clinical practice to perform combined morphological and hemodynamic analysis in scanned vessels. Here, the spatial distribution of the blood flow velocity is coded as a colored area, which is superimposed on the B-mode image obtained for the scanned section of the vessel. Due to hardware limitations, there is a trade-off between the quality of the B-mode component and the quality of color-coded flow component of the duplex image [14].

2.3.1 Doppler frequency-dependent mode

A color-coded flow image can be obtained by color coding the Doppler frequencies of the mean flow velocity, as illustrated in Fig. 2.2. The color coding depends on the flow direction. One color is used for flows toward the probe and another color

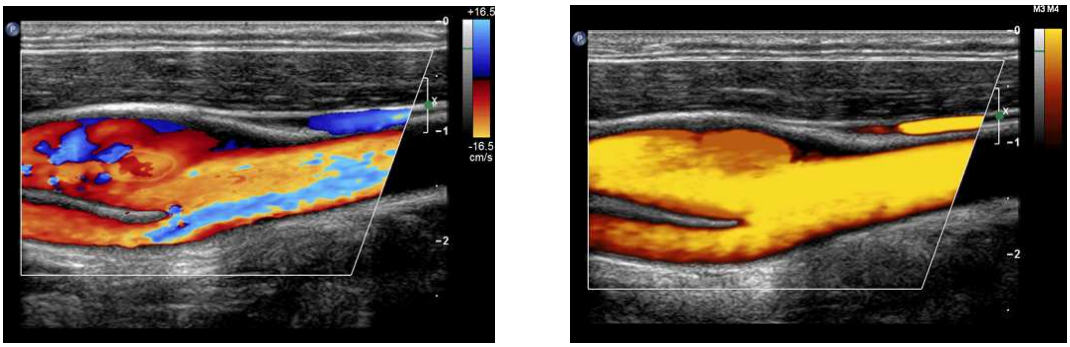

(a) (b)

Fig. 2.2: Color-coded duplex sonography: a) Doppler frequency-dependent mode; b) Doppler intensity-dependent mode.

is used for flows away from the probe. Red and blue are the two standard colors used [14].

2.3.2 Doppler intensity-dependent mode

Another form of duplex sonography is the Doppler intensity-dependent mode, also known as power-Doppler mode or energy-Doppler mode (Fig. 2.2). Here, the flow image is composed with a coding of the Doppler spectrum amplitudes. This mode is less dependent on the angle of incidence of the pulse, improving the imaging of tortuous vessels. It is also better suited for the imaging of low flow velocities [14].

2.4 3D systems

Up to date, the conventional 2D imaging is the standard mean of ultrasound medical diagnosis. However, in the last years, most of the major manufacturers have included 3D features into their medical ultrasound equipment. This development is a step forward in this medical image modality, which has stimulated the development of methodologies for the automatic processing of 3D ultrasound medical images.

3D medical ultrasound systems offer a number of advantages: volumes can be resliced at new planes that are normally inaccessible due to physical restrictions of the scanning process; the rendering of 3D surfaces and volumes may reveal pathologies that are hard to see in 2D imaging; it enables much more accurate quantification of volume than 2D techniques; 3D ultrasound systems are much cheaper than other 3D imaging modalities, like Computer Tomography (CT), Magnetic Resonance

Imaging (MRI) or Positron Emission Tomography (PET); it is not ionizing nor invasive and the risk to the patient is very small; and it allows better documentation of the examination [12].

The 3D ultrasound imaging has been applied to a number of medical areas, some of which are: cardiology; obstetrics; prostate volumes; detection of atherosclerosis in the carotid artery; breast masses; liver tissues; kidney tissues [12, 16].

Despite its advantages, 3D ultrasound diagnosis is not yet a common technique in routine clinical practice. There are some issues that have to be further improved, in particular: the inability to acquire large volumes; the sensitivity of the 3D sensors to metallic objects; long processing times; and demanding protocols for scanning. Nevertheless, it is believed that this picture will change in the near future [12].

2.4.1 Current techniques

In 3D ultrasound systems, image volumes are usually acquired by sweeping a conventional 2D probe over the area of interest and tracking the position and orientation of the resulting B-scans. Acquisition systems can be grouped according to: a) the way they determine the position of the B-scan; b) the restrictions imposed to the motion of the probe. Commercialized 3D scanning protocols can be of the following type: linear drawback; rotational; fan; linear; volume; freehand. A short description of their characteristics and typical applications can be found in [12].

2.4.2 The freehand 3D system

The most popular protocol is the 3D freehand system (Fig. 2.3) because it is the cheapest and the most flexible, since the probe is moved by hand in an arbitrary manner. Its main drawbacks are the difficulty to avoid motion artifacts and the need to attach a position sensor to the probe. Motion artifacts can be caused by movements of the patient (e.g., respiration or cardiac pulses) or an irregular pressure of the probe during the manual sweeping. The attachment of an external position sensor to the probe is not desirable because it disturbs the clinical routine. Moreover, most position sensors are magnetic devices that are sensitive to metallic objects. However, some manufactures are now beginning to commercialize new freehand probes with integrated 3D sensors.

An important issue is whether to work with voxels (3D equivalent of pixels) or directly with the non-regularly spaced data obtained with the 3D freehand system. There are many mature tools for displaying and analyzing voxel arrays [12], but this

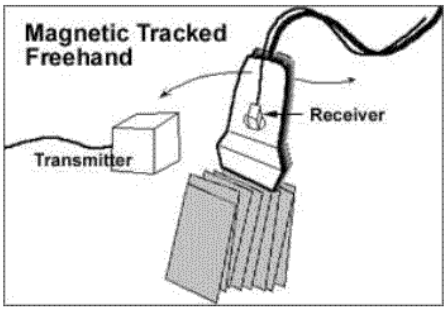

Fig. 2.3: 3D freehand ultrasound system.

approach has several problems: the B-scans have to be resampled onto a regular voxel array before any further processing; slices obtained from interpolated voxel arrays are rarely as good as the original B-scans; high resolution voxel arrays requires large storage space in memory; B-scans are more familiar to experts, facilitating the detection of boundaries between different tissues. The main disadvantage of working directly with the irregularly spaced data is the heavier computational effort that its processing demands.

2.5 Ultrasound imaging of the carotid

2.5.1 Atherosclerosis

Atherosclerosis is an inflammatory disease of blood vessels caused by the accumulation of lipoproteins in artery walls. This deposit of lipids is known as plaque (Fig.2.4) and may include calcified tissues [18].

The formation of plaque causes a stenosis (narrowing) of the artery, reducing the blood supply to the organ it feeds. If a piece of the plaque is released, it may cause the formation of a thrombus that will rapidly slow or stop the blood flow, leading to an infarction, the death of the tissues fed by the artery. Two well known types of infarction are: the myocardial infarction (heart attack); and the stroke, a cerebrovascular accident (CVA) that results in the loss of brain functions [1, 2]. These cardiovascular accidents are frequently fatal and for those who survive the therapeutic options are limited. Early diagnosis and treatment is crucial to prevent more serious stages of the disease [18].

The intima-media thickness (IMT) of extracranial carotid arteries is an index of individual atherosclerosis and is used in clinical practice for cardiovascular risk

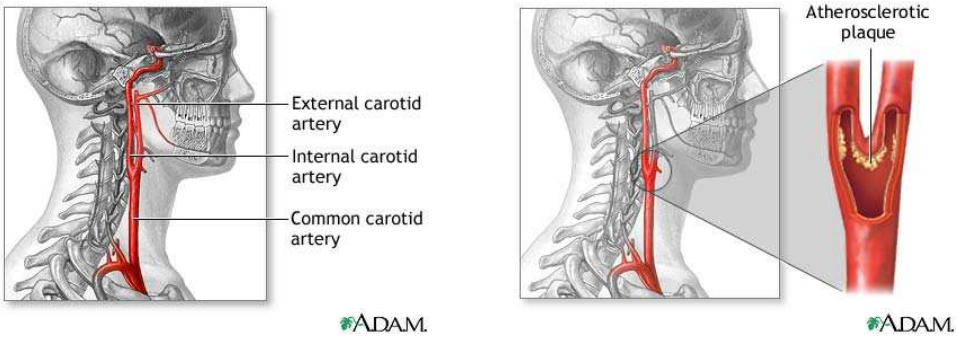

(a) (b)

Fig. 2.4: Anatomy of the carotid: a) Illustration of the common carotid artery (CCA), the internal carotid artery (ICA) and the external carotid artery (ECA); b) Illustration of a carotid bifurcation with plaque.

assessment [19].

2.5.2 Detection of atherosclerosis

Atherosclerosis may be detected with the aid of several different medical exams, like intravascular ultrasound (IVUS), X-ray angiography or standard ultrasound imaging (B-mode, Power-Doppler mode, etc).

X-ray angiography has been, up to date, the cornerstone of diagnosis and treatment planning for vascular diseases, but it requires an injection of radiopaque dye in the patient's blood, to induce a good contrast, and exposes the patient to ionizing radiation. The contrast dyes used in X-ray can produce allergic reactions and kidney failure, sometimes leading to death [18]. Another limitation is its unsuitability for 3D representations of the carotid.

IVUS seems to be the most frequent ultrasound modality used in the detection of atherosclerosis [16]. It is less aggressive than the X-ray angiography and gives better quality images than B-mode systems. Nevertheless, it is invasive, requiring the insertion of a catheter into the patient's artery, and it is unable to consider the vessel curvature and the orientation of the catheter [16, 18].

Since the carotid is a superficial artery of easy access, it is suited for B-mode ultrasound imaging, which is very attractive for its low cost and small risk to the patient [12]. Moreover, B-mode images can be acquired with a 3D ultrasound system, to obtain 3D representations of the vessel. Other standard ultrasound modes (e.g., Power-Doppler and Echo-Doppler) are also intensively used in clinical practice, as

complements to B-mode imaging. However, B-mode images give the best picture of the anatomical structure of the scanned tissues. Therefore, they are the best option for automatic segmentation of the carotid tissues.

In ultrasound images, the carotid wall is characterized by echogenic lines separated by a hypoechogenic space, an intensity valley shaped edge known as the 'double line' pattern. In longitudinal sections of the carotid, the artery wall appears as smooth open contours that extend from one image side to the other. In transversal sections the wall contour has an ellipsoidal shape. The carotid lumen appears as a dark region, sometimes speckled with brighter granularities due to noise. The plaque, when present, is localized between the artery wall and the lumen, has variable response to the echo and frequently shows a texture similar to the tissues surrounding the artery.

The bifurcation of the carotid (Fig.2.4) and the internal carotid artery (ICA) are more prone to atherosclerosis, due to stronger hemodynamic stresses in the bifurcation and branching zones. Unfortunately, it is difficult to visualize the 'double line' pattern at these locations. For these reasons, the common carotid artery (CCA) has received special focus of IMT measurements in B-mode ultrasound imaging [20], not only in the clinical practice but also in the development of segmentation algorithms, by the image processing community.

Chapter 3

STATE OF THE ART

Automatic segmentation methods have been intensively applied to a wide variety of medical imaging modalities, like X-ray, magnetic resonance imaging (MRI), X-ray computed tomography (CT) and ultrasound.

The ultrasound modality presents a huge challenge to automatic segmentation due to its very poor quality, when compared with other medical imaging modalities. Ultrasound images are characterized by [12,16,18]: strong speckle noise, non-uniform echo intensity, low contrast, movement artifacts, gaps in organ boundaries due echo dropouts and shadows. These difficulties are behind the minor attention given to ultrasound diagnosis, when compared to other image modalities. However, in the last years there has been a large increase in the interest in medical ultrasound imaging, as a result of advances in its quality and resolution, allied to several advantages relative to other modalities, like its portability, its non-invasive nature and safety for the patient, not to mention the fact that it is a much cheaper modality. This fact is well illustrated in [16], a very recent and comprehensive survey of the state of the art in the field of ultrasound image segmentation, and in the interesting paper of Gee *et al.* [12] about freehand 3D ultrasound systems.

As demonstrated in [16], unlike what happens in other imaging modalities, general methods of image segmentation usually fail in ultrasound images. It seems that the segmentation approaches that try to model the image physics have been more successful. This survey also shows that most of the effort has been focused on the segmentation of echocardiography, breast ultrasound, transrectal ultrasound (TRUS), intravascular ultrasound (IVUS), and ultrasound imaging in obstetrics and gynecology. On the other hand, the number of published works on 2D segmentation is far more extensive than 3D approaches, which are taking their first steps. The authors also make some pertinent observations about the validation in this field, namely: a) the manual delineation on clinical images is by far the most popular means of performance assessment, although it generally introduces inter- and

intra-expert variability; b) there is no standardization of performance measures, which hinders the direct comparison of different methods; c) there are no standard databases on which different groups can compare methods; d) many of the papers do not validate their results on a database and those who do it frequently use databases with less than 50 cases.

Concerning the methodology used, ultrasound segmentation algorithms may be grouped according to the considered specific constraints, in particular, the way speckle noise is dealt with, the used shape priors and the chosen image features, like the echo intensity, its gradient and texture measures. In most cases, a combination of several of these constraints gives better results. The choice of which to use is application specific.

Whether the segmentation is done in 2D or in 3D, level set active contours [21–23], also known as geometric snakes, have become the dominant tool in medical imaging, due to its many advantages, like the easy integration of regional statistics, the topological preservation and their powerful ability to accurately detect anatomical boundaries and surfaces with arbitrary shapes. This fact can be confirmed in [24], a very interesting survey and comparative analysis of parametric and geometric snakes applied to medical image processing. However, their success in ultrasound images usually depends on the ability to incorporate some shape prior restriction into the evolution of the active contour. Otherwise, the snake will often leak through gaps in the boundaries of the tissues.

This review will focus on the work done on the segmentation of ultrasound images of the carotid. For a wider and detailed perspective of the methodologies used in other fields of ultrasound image segmentation we suggest Noble's survey [16].

There are a number of very interesting examples of shape-based segmentation [25–39], most of which have been applied with success to ultrasound images. Shape priors are very popular in ultrasound images because large parts of the data are often missing or corrupted by strong noise. But, as pointed out in [16], the application of shape constraints to disease cases (like carotids with plaque) is still an open issue. In the particular case of the carotid artery, we may also be faced with the large variability of the shape, which depends not only on its deformation due to pressure but also on the position and orientation of the acquired slices. In fact, unlike most other applications where the whole organ is imaged, different B-scans of the carotid may correspond to different parts of the artery, with quite different anatomy. In the segmentation of 3D volumes, the shape variability may become simpler. But this is a serious and discouraging problem if the vessel boundaries

are segmented frame by frame. Things get worse if the B-scans are acquired with arbitrary orientation. However, this is not the case in clinical practice, where the B-scans are always approximately normal or parallel to the major axis of the artery. These orientations give the best picture of the vascular structure. In fact, these orientations are also convenient when acquiring sequences of frames with 3D freehand systems, to minimize the losses in the visibility of the boundaries between different tissues.

Speckle noise is inherent to ultrasound imaging and appears in the form of a granular texture of the echogenic regions. This texture appearance does not correspond to underlying tissue structure but the speckle intensity depends on the scanned tissue [16]. Therefore, it may be used to improve the segmentation. It is also frequently viewed as just noise to be reduced. The acquisition process of ultrasound images starts with a coherent summation of the echo signals produced by tissue scatterers. The density and spatial distribution of the scatterers depend on the scanned tissues and determine the statistical distribution of the speckle. Several statistical distributions (e.g., Rayleigh distribution [40, 41], Rice distribution [40, 42], K-distribution [43, 44], generalized K-distribution [44, 45] and homodyned K-distribution [44, 45]) have been proposed in literature to model the speckle noise under several scattering conditions. Most of these models are very complex to analyze and are applicable only to non-compressed signals. However, log-compressed ultrasound images are the most common in clinical practice, due to their reduced intensity dynamic range. Statistics of the log-compressed ultrasound signals have also been proposed [46, 47]. Extensive work has been published on speckle reduction (most of which use wavelets [48–50] and anisotropic diffusion [51–54]) and tissue characterization from speckle [15,42,43,55–61]. Speckle does not seem to bring much information to the segmentation of the carotid artery in B-mode images. Therefore, in this case, it is usually viewed as just noise.

Texture measures may give good discriminating features and have been used with success in the classification of several tissues in clinical ultrasound images, such as breast masses, liver tissues, kidney tissues and the prostate tissues [16]. There has also been some success in the classification of different kinds of carotid plaques using texture measures [62, 63]. But texture based segmentation is much more difficult and may not be possible for B-mode images of the carotid. The degree of discrimination in carotid plaques is very low and large regions of interest have to be considered in the extraction of their features. There is also strong evidence [64] that echogenic plaques and the tissues surrounding the artery have, in general, very

similar texture properties. On the other hand, hypoechogenic plaques can easily be misclassified as part of the lumen region. In fact, we may find some weak speckle noise inside the lumen that is stronger than the echo produced by hypoechogenic plaques. Our experiments with banks of Gabor filters [65, 66] confirmed the strong similarity between echogenic regions of interest.

The echo intensity gradient is the most frequent edge detector [67] in general image segmentation. But it was conceived for images affected by additive noise. Therefore, in spite of its popularity in ultrasound image segmentation, it is not well suited for ultrasound images, where the noise has a multiplicative nature. A better edge detector, known as the instantaneous coefficient of variation (ICOV) [51, 52], has been specifically conceived for these images. The echo intensity along with its gradient are the most frequently used features in the segmentation of B-mode images of the carotid.

3.1 Segmentation of the carotid in 2D B-mode images

In the particular case of the ultrasound diagnosis of atherosclerosis, IVUS seems to be the most frequent modality [16]. It is less aggressive than the X-ray angiography and gives better quality images than freehand B-mode systems. Nevertheless, it is still invasive, requiring the insertion of a catheter into the patient's artery, and it is unable to consider the vessel curvature and the orientation of the catheter [16, 18].

In spite of the attractive advantages of freehand B-mode imaging of the carotid, there isn't much literature on its automatic segmentation, probably due to the extreme difficulty in the automatic detection of the carotid boundaries in these images. In fact, although Noble's survey [16] is very recent and comprehensive, it dedicates only five lines to this particular problem.

In the first published attempts to detect the carotid boundaries in ultrasound images [3–5], a previous manual segmentation of the boundary was needed. The location of the boundary was then refined, according to the local value of a single image feature, like the echo intensity or the intensity gradient. These approaches suffered from two important weaknesses: first, the large manual intervention needed, which is time consuming and prone to subjective segmentation results; second, the utilization of a single image feature is usually not enough to correctly detect the carotid boundaries in B-mode images, characterized by strong speckle noise, echo

dropouts and large discontinuities in the boundaries.

More powerful approaches were proposed in [6, 7]. A common characteristic of these approaches is the minimization of a global cost function through dynamic programming (DP). The cost function may integrate multiple image features, like the echo intensity and its gradient, and a local geometric constraint to guide and smooth the estimated contour. Each feature or constraint is represented by a cost term and the relative importance of each term is determined by a weighting factor previously determined in a training stage. These models produce more robust segmentations with less human intervention, specially in the case of [6]. In a later study [68], the DP algorithm proposed in [6] also demonstrated better performance when compared with some alternative approaches, like the maximum gradient algorithm [5] and the matched filter algorithm [69].

More recently, an improvement of [6] was proposed in [8]. The main novelties are the embedding of the DP algorithm in a multiscale scheme, to get a first rough estimate of the carotid wall boundaries, and the incorporation of an external force as a new term in the cost function, which allows the human intervention over the selected best path, in case of incorrect detection. This model was tested against a large data set with promising results and has the advantage of being relatively fast. But it has several important drawbacks: its performance is significantly affected by the presence of plaque and other boundaries; frequently, human correction is also needed when the quality of the images is poorer; the determination of the optimal weight vector requires an exhaustive search in the weight space and a different vector has to be computed for each boundary; a retraining of the system may have to be done for images acquired with different ultrasonic equipment, although the authors reported consistent results, without retraining, for an image set taken with a different scanner; DP implementations are not suited for the incorporation of global smoothness constraints, which are more powerful than local ones, nor to deal with deep concavities or sharp saliences that may appear in the boundary of the plaque; finally, the DP algorithm is not directly applicable to closed contours, which is possibly the reason why the segmentation of transversal sections of the carotid was not referred.

Another family of algorithms [9–11] tried to apply parametric snakes [70] to the detection of the carotid boundaries. Active contours have been used with success in other fields of medical image segmentation. However, for several reasons, they do not seem to be the best choice for the segmentation of the carotid wall. First, they usually require a manual initialization of the snake in the close vicinity of the

carotid boundaries. This implies intensive human intervention and the algorithms appear more like methods for refinement of the boundary location and less like automatic segmentation algorithms. Second, the propagation force is frequently based on intensity gradients and, therefore, they tend to be very vulnerable to the attraction by false edges, located between the initialized snake and the boundary to be detected. Third, these snakes usually leak at wall gaps where there is no gradient or it is too weak.

In [9], the leaking problem was solved by discarding all images with big boundary gaps. They also excluded the images where the lumen boundary or the carotid wall boundary could not be defined visually. The snake has to be initialized manually and very close to the far end lumen boundary or the far end wall boundary, the only boundaries detected in this work. The intensity gradient was the only image feature considered in the energy of the snake. Some statistics computed for a large data base of longitudinal sections showed a smaller variability than manual tracings done by experts.

A more sophisticated external force was used in [10, 11], but also based on the intensity gradient, which means the snake is still sensitive to local noise and boundary gaps. Once again, the segmentation was done only for the far end boundaries of the carotid, in longitudinal sections. The user just has to specify the starting and the end points of the snake, significantly reducing the human intervention. A small rectangular region of interest is selected automatically, such that the former two points are included in this region. Then, for each vertical line inside this region, the first edge found in the downward direction is taken as a pixel of the lumen boundary. From this initial contour, the snake finds the final location of the lumen boundary. To detect the wall boundary, the snake is displaced downwards about 0.05 cm and a new search is done for the global minimum of the snake's energy. Some results were presented but the work lacks a validation with statistical meaning.

Quite different approaches were proposed in [71, 72]. In [71], the authors presented a new scheme for the segmentation of the carotid in B-mode images, based on the multi-resolution analysis and watershed techniques. In [72], the segmentation was based on a fuzzy region growing algorithm and thresholding. In both cases, only the lumen region was segmented and the results were illustrated with a single image. Both algorithms lack a quantitative validation in clinical images.

3.2 Segmentation of the carotid in 3D B-mode volumes

A few works have been published on 3D segmentation of the carotid boundaries from B-mode volumes. But this topic is still in its beginning and it is usually limited to the segmentation of the lumen region, leaving out the detection of the wall boundary.

Gill *et al.* [73] proposed a semi-automatic segmentation of the carotid lumen in 3D ultrasound images, using a dynamic balloon model, which is manually initialized inside the lumen region. The semi-automatic segmentation obtained for a 3D data set proved to be close to the fully manual segmentation.

Zahalka and Fenster [74] used a radial search scheme, relative to a seed manually placed inside the lumen, to get an initial estimate of the lumen boundary. Then, in a second step, a geometric deformable model (GDM) was applied to obtain a smoothed final contour. The algorithm was tested in two data sets with good results. However, the images of these data sets seem to have very low noise in the lumen region and do not have hypoechogenic plaques. It is not clear how these algorithms would behave on normal clinical images.

Baillard *et al.* [75] assumed a normal distribution for the intensity inside the lumen and a shifted Rayleigh distribution for the intensity in echogenic tissues. The lumen volume was then segmented with a Stochastic Expectation-Maximization (SEM) algorithm [76, 77], embedded in a 3D level set scheme. This is a simple representation of the tissues that does not account for speckle noise inside the lumen nor large boundary gaps caused by echo dropouts. Moreover, it cannot detect the wall boundaries and the superposition of the different probability density functions may give biased estimates of the decision level. The results were only illustrated by two examples and no quantitative measures were presented in this case.

In [78], the authors reconstructed the carotid wall and the lumen boundary surfaces from sequences of B-scans acquired with a 3D freehand system. But the B-scans are manually segmented.

A recent and interesting work can be found in [79,80], where the carotid surfaces were semi-automatically reconstructed from sequences of B-scans of the artery. Both the carotid wall and the lumen boundary were segmented, which is a step forward, when compared to the other referred automatic approaches. However, a gradient vector flow (GVF) snake [81] was used to detect the carotid boundaries. Therefore, as other snakes moved under gradient-based forces, the GVF snake may have to be initialized close to the boundary to be detected, when there are nearby edges

originated by noise or from other boundaries. On the other hand, these snakes tend to leak through boundary gaps, where there is no gradient or it is too weak. Finally, being a parametric snake, it may need additional processing when a topological change happens.

Chapter 4

SEGMENTATION OF THE CAROTID WALL IN B-MODE IMAGES

4.1 Introduction

Automatic segmentation of ultrasound medical images is extremely difficult, due to their complexity and poor quality. When compared to other applications of medical ultrasound imaging, the segmentation of the carotid artery in B-mode images presents additional difficulties, like the possible presence of plaque (disease tissue), which is often difficult to discriminate from other adjacent tissues. In other medical ultrasound applications, shape-based segmentation is often used with success to deal with gaps in the boundaries of the examined organ, caused by echo dropouts and shadows. However, the presence of plaque is an obstacle to the shape-based segmentation of the carotid. Another obstacle to this segmentation method is the impossibility to scan the whole organ, which means that different B-scans may correspond to different parts of the artery, with different anatomy. Even in the absence of plaque, the carotid wall is still very challenging to detect, since it frequently appears as a diffuse boundary between two echogenic tissues, with large discontinuities.

In spite of several attempts to automatically segment the carotid in B-mode images, this problem is still far from being well resolved. As a consequence, a manual segmentation of these images, performed by an experienced medical doctor, is the usual adopted procedure (see, for instance, [63, 78]), which is a tedious and time consuming task and tends to give subjective results.

The chapter starts with an overview of the method proposed for the automatic detection of the carotid wall in B-mode images, followed by several sections where the algorithm is described in detail, step by step. Finally, several results, computed from an image data base, and some concluding remarks are presented.

4.2 Overview of the approach

In face of the difficulties previously described for model-based detection of the carotid wall in ultrasound images, the ideal segmentation model should not be too flexible, in order to keep a strong robustness to noise and missing data, nor too rigid to correctly follow the desired boundary over its whole contour path. Moreover, it should avoid any gradient based motion, like in snake-based models. These requirements suggest looking for the best globally most significant smooth curve, according to some cost or gain function.

With these requirements in mind, we introduce a new segmentation algorithm for the detection of the CCA wall in ultrasound images, which looks for the best smooth curves in the image, according to a new gain function. Our algorithm is robust to speckle noise, irregular contrast due to echo dropouts and occlusions of the lumen caused by the plaque. Moreover, it also has the capability of adapting to flexible tubular shapes.

As in previous works on the segmentation of ultrasound images of the carotid [6, 8–11, 68], our algorithm was designed for sections of the CCA. But it can also be used in sections of the internal carotid artery (ICA) or the external carotid artery (ECA), as long as the image quality is not too poor. As we will show, our segmentation algorithm can be applied both to transversal and longitudinal sections.

The idea of looking for the most significant path is common to the dynamic programming algorithm proposed in [6], but our approach is quite different and presents several advantages. First, our model includes a global smoothness constraint which is not easily integrated in the dynamic programming approach. Second, the user does not have to specify a different region of interest (ROI) for each boundary. Third, our model does not need a previously determined reference path used as geometric constraint.

Next we give a global description of our algorithm, leaving most of the details for further discussion in subsequent sections.

It would be impractical to evaluate all possible paths. So, as an alternative to look for the best path, we use the very popular random sample consensus (RANSAC) algorithm [82], which works quite well in practice.

In longitudinal sections, the smooth curve model is a cubic spline with only a few control points, which has enough stiffness to stay robust to noise but is also flexible enough to correctly follow the carotid wall along its whole axis, even when it is severely bended. The locations of the spline control points are dynamically

chosen by the algorithm.

In transversal sections, an ellipse is used as the wall model since the wall contour in these sections has an elliptical shape.

The wall model consensus is measured by a new gain function that integrates the responses to the most discriminating characteristics of the carotid boundary: the proximity of the wall model to points of step edges; the proximity to valley edge points; the consistency between the orientation of the normal to the wall model and the orientation of the intensity gradient; and the distance to the detected lumen boundary.

Ideally, the distance to the lumen boundary should be represented by a signed distance function, here designated by SDL, with negative sign inside the lumen. It has been shown in [13] that thresholding algorithms may be used to segment the lumen in B-mode images of the carotid. Nevertheless, this usually produces more than one dark region, one of which is the lumen region. Moreover, in some B-mode images of the carotid there may be connections between the lumen region and other dark regions due to large gaps in the carotid wall. This makes it difficult to isolate the lumen region from the other dark regions and we end up with the signed distance to the boundaries of all dark regions. However, if we have an estimate of the lumen axis position, we may use it to select the surrounding region boundaries and significantly improve the estimate of the signed distance function.

The proposed algorithm requires a rough location of the lumen axis. This can easily be computed if we already have an approximate segmentation of the lumen. Unfortunately, this may not be possible due to the difficulties, discussed above, in isolating the lumen region. So, in transversal sections, the user has to choose one single point near the centroid of the lumen. In longitudinal sections, the user has to choose between 2 and 4 points roughly near the lumen medial axis, depending on the curvature of the carotid wall. If the carotid has low curvature along the medial axis, one point at each extremity will be enough. Nevertheless, this is faster and easier than selecting the whole ROI or initializing a snake close to the carotid boundary we want to detect.

We also introduce a new robust non-linear image filter, suited to ultrasound images, to compute an edge map with reduced noise and good localization of the edges. Our filter combines the properties of Tauber's anisotropic diffusion filter [53], which is well suited to ultrasound images in general, with a curvature dependent diffusion property that improves the preservation of objects with low curvature, like the carotid boundaries. The curvature dependence of the filter borrows concepts from

Total Variation theory [83, 84] and is incorporated through the Marquina-Osher's scheme for a mean curvature motion filter [85]. As in the Tauber's model, our filter also incorporates: an edge detector known as the instantaneous coefficient of variation (ICOV) [51, 52], more suited to the multiplicative nature of the speckle noise; the Tukey's function as the 'edge stopping' function, to improve the automatic stopping of the diffusion and produce sharper boundaries; and the median absolute deviation (MAD) as a base for the edge scale estimator.

Figure 4.1 shows a block diagram with the main steps of our algorithm, when applied to longitudinal sections. For transversal sections the procedure is very similar, except that instead of splines we have ellipses, instead of the lumen medial axis we have the lumen centroid and, finally, the dominant gradient direction block is not used. The input is an ultrasound image of the CCA, from which the lumen medial axis or the lumen centroid is obtained. The lumen medial axis is used to automatically select a ROI from the image and to improve the estimate of the signed distance to the lumen boundary. This signed distance computation also relies on a binary image computed from the ROI through a thresholding algorithm. The non-linear image filter is applied to the ROI to get a smooth image for which a gradient map and an edge map are computed. The spline model depends on the gradient orientation at the control points. So, the gradient map is substituted by the map of the local dominant gradient direction, with reduced error in the gradient orientation. The edge map is cleaned of all edges incompatible with the carotid walls and then used, in conjunction with the ROI and the dominant gradient map, to compute the valley edge map. Finally, the cleaned edge map, the valley edge map, the dominant gradient map and the signed distance to the lumen boundary are used as inputs to the gain function, during the RANSAC search. The outputs are the best splines found, above and bellow the lumen axis, according to the specified gain function.

The wall model can be further improved, in a subsequent step, through a function minimization in the vicinity of the solution found by the RANSAC search.

4.3 Lumen axis and ROI selection

The whole procedure starts with the user pointing out the approximate location of the lumen axis. This is done by clicking over the image with the mouse.

In transversal sections, only one click is necessary, near the centroid of the lumen. In longitudinal sections, the user has to enter at least one point at each extremity of the longitudinal axis. If the axis is significantly bended, then one or two additional

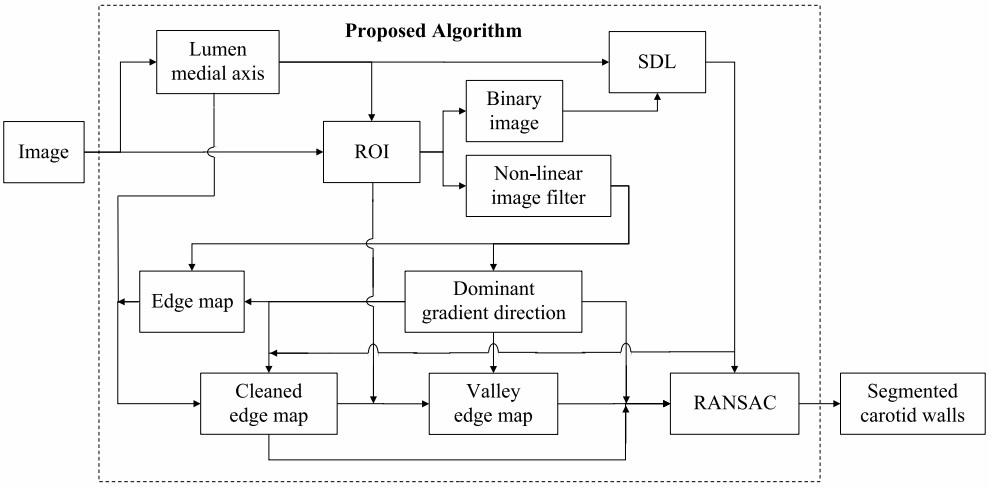

Fig. 4.1: Block diagram with the main steps of the proposed algorithm.

points should be entered along the lumen axis. This is the only human interaction needed. If the user enters more than one point, the algorithm assumes the image is a longitudinal section and completes the medial axis by cubic spline interpolation. Figure 4.2 illustrates the procedure for two sections of the CCA.

In the segmentation of 3D volumes, formed by sequences of B-scans, the user intervention is only required in the first frame. For the other frames, the estimation of the lumen axis location is done automatically, inferring this information from the segmentation of the previous frame.

Once the approximate location of the lumen axis is known, the ROI is selected, as shown in Fig. 4.2 (b) and Fig. 4.2 (d). Assuming the artery boundaries will not be at a distance, d, from the lumen axis, larger than a certain threshold, $d_{\max}$, the ROI may be chosen as the smallest rectangular box containing all image pixels within distance $d_{\max}$ to the lumen axis. This distance threshold can be estimated from the largest carotid found in an image data base. By limiting the image processing to this ROI, the computational effort is reduced.

4.4 Determination of the SDL

The signed distance to the lumen boundary is determined over the selected ROI box.

As will be demonstrated in chapter 5, the triangle thresholding algorithm [86] is a quick way to compute a good rough estimate of the lumen region. Therefore, it

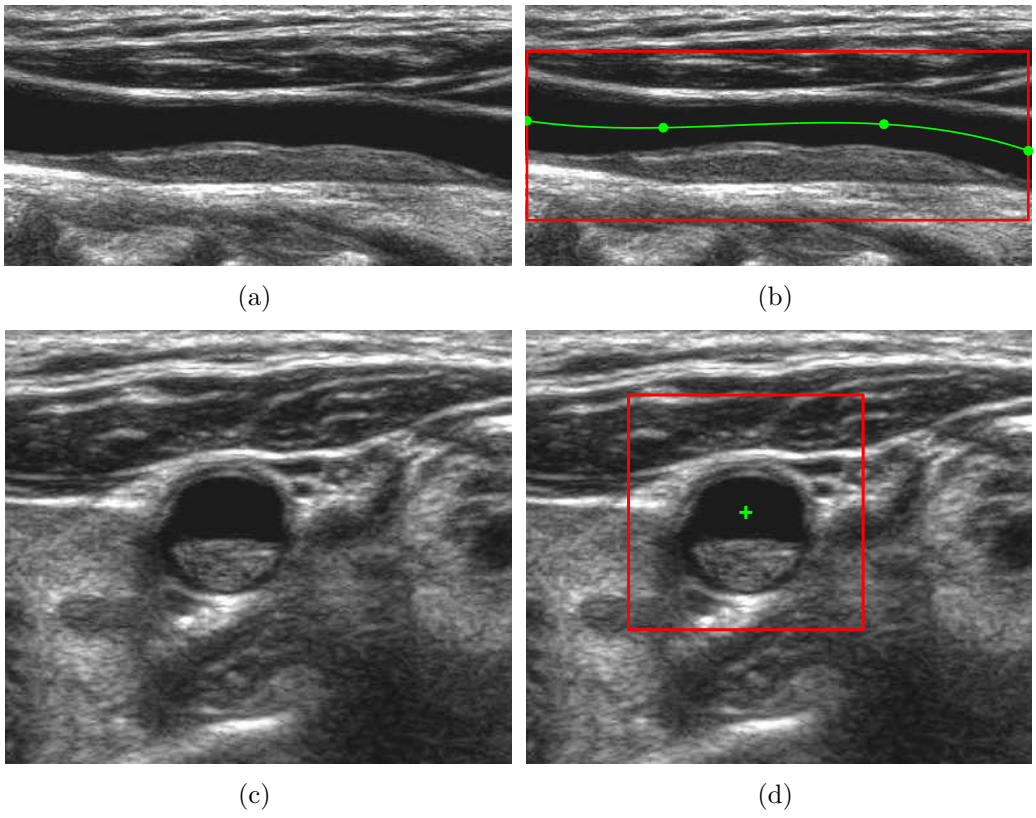

Fig. 4.2: Localization of the lumen axis by the user: a) A longitudinal section of the CCA; b) The ROI box (in red) for the longitudinal section, the interpolated lumen medial axis (green curve) and the four points entered by the user, represented as large green dots over the axis curve; c) A transversal section of the CCA; d) The ROI box (in red) for the transversal section and the single point entered by the user, represented a large green cross inside the lumen region.

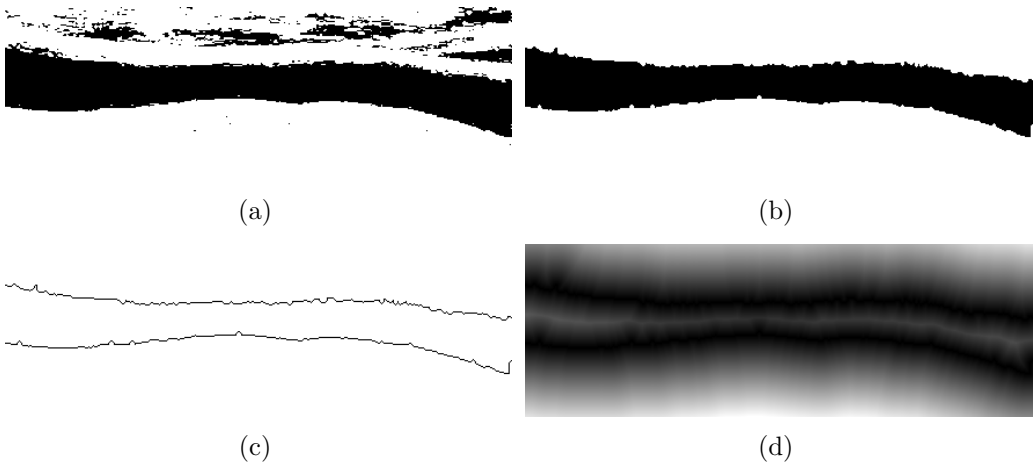

Fig. 4.3: Determination of the SDL in a longitudinal section: a) Binary image computed from the ROI box; b) Estimated lumen region; c) Boundary of the estimated lumen region; d) |SDL| represented as an intensity map.

is used to estimate an intensity threshold, with which a binary version of the ROI is computed. The binary images obtained for the ROI's of Fig. 4.2 (b) and (d) are shown in Fig. 4.3 (a) and Fig. 4.4 (a), respectively.

Using the lumen axis specified by the user as a reference, an estimate of the lumen region is computed as the set of black pixels in the binary image that can be reached from the lumen axis through a vertical line, in longitudinal sections, or a radial Bresenham line [87], in transversal sections. This procedure is illustrated in Fig. 4.3 (b) and Fig. 4.4 (b).

Figure. 4.3 (c) and Fig. 4.4 (c) show the boundary pixels of the estimated lumen region, determined as the set of pixels of the lumen region that have at least one 4-neighbor outside the lumen.

Finally, the Euclidean distance map to the lumen boundary is computed with the second algorithm described in [88], setting to negative the distances inside the lumen region. Figure 4.3 (d) and Fig. 4.4 (d) show the intensity maps of |SDL|, for the longitudinal section and the transversal section, respectively. Here, larger absolute distances were represented by brighter intensities.

4.5 Non-linear image filtering

To get the edge map from the ultrasound image, a smooth version of the original image is first computed, using low-pass filtering. Then, an edge detector is applied

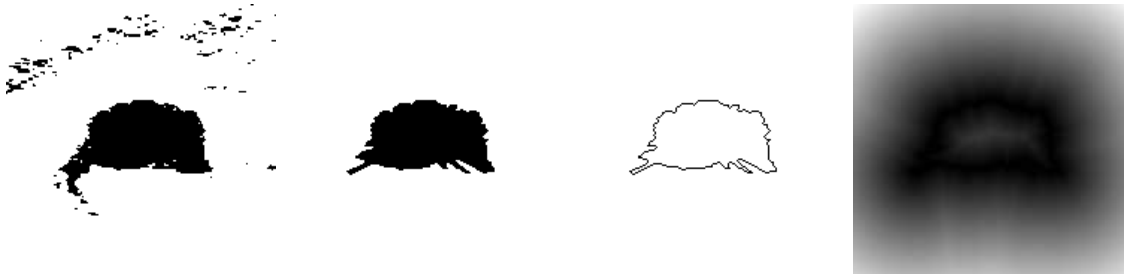

(a) (b) (c) (d)

Fig. 4.4: Determination of the SDL in a transversal section: a) Binary image computed from the ROI box; b) Estimated lumen region; c) Boundary of the estimated lumen region; d) |SDL| represented as an intensity map.

to this smoothed image to select the stronger edges.

A good smoothing filter should clean the noise while preserving the important boundaries as well as their location. Anisotropic diffusion and other non-linear filters are known as the best ones for this purpose. In these filters, some edge detector is included in a partial differential equation (PDE) model, encouraging smoothing in homogeneous regions while inhibiting the smoothing across the boundaries. The anisotropic diffusion model suggested by Perona and Malik [89] was probably the first one to be used in image processing, and it became very popular. Two other very successful non-linear filters are the total variation (TV) denoising [83, 84] and the related Marquina-Osher model [85]. All these filters were designed for additive noise, so their performance in ultrasound images is not so good due to the speckle noise, which has a multiplicative nature.

Yu and Acton [51, 52] introduced the ICOV edge detector and proved it is significantly better for speckled images than other classical edge detectors. The ICOV value at pixel (i, j) is given by:

$$\mathrm{ICOV}_{i,j} = \sqrt{\frac{|\frac{1}{2}\|\nabla I_{i,j}\|^2 - \frac{1}{16}(\nabla^2 I_{i,j})^2|}{(I_{i,j} + \frac{1}{4}\nabla^2 I_{i,j})^2}} \tag{4.1}$$

where $\|\nabla I_{i,j}\|^2 = 0.5[\|\nabla_- I_{i,j}\|^2 + \|\nabla_+ I_{i,j}\|^2]$, $\nabla_- I_{i,j} = (I_{i,j} - I_{i-1,j}, I_{i,j} - I_{i,j-1})$, $\nabla_+ I_{i,j} = (I_{i+1,j} - I_{i,j}, I_{i,j+1} - I_{i,j})$, $\nabla^2 I_{i,j} = I_{i+1,j} + I_{i-1,j} + I_{i,j+1} + I_{i,j-1} - 4I_{i,j}$, $\|(u, v)\| = \sqrt{u^2 + v^2}$ is the norm of a vector (u, v) and I represents the image intensity.

They also proposed an anisotropic diffusion model based on this detector, but it isn't very stable, as pointed out in [53].

To decide which edges are boundaries, we need an estimate of the image edge scale, σ_e. We expect that most of the image pixels belong to homogeneous regions, with low ICOV values. Boundaries will be outliers, with large ICOV values. As in [53,90], we appeal to tools of robust statistics to estimate σ_e, by computing a scale of the image ICOV based on its median absolute deviation (MAD). In particular, we use the measure proposed in [53], which is better formulated than in [90] and is given by

$$\begin{aligned} \sigma_e &= C \underset{\Omega}{\text{MAD}}(\text{ICOV}) + \underset{\Omega}{\text{med}}(\text{ICOV}) \\ &= C \underset{\Omega}{\text{med}} |\text{ICOV} - \underset{\Omega}{\text{med}}(\text{ICOV})| + \underset{\Omega}{\text{med}}(\text{ICOV}) \end{aligned} \tag{4.2}$$

where $\underset{\Omega}{\text{med}}(r)$ is the median of r over the image domain, Ω, and $C = 1.4826$ is a constant, derived from the fact that the MAD of a zero-mean normal distribution with unit variance is $1/1.4826$. The measure proposed in [90] is not correct because it uses just the first term of equation 4.2. Therefore, it measures the deviation of the data sample relative to its median, which cannot be directly compared with the data of the sample [53].

In [90], Black and his colleagues showed that the anisotropic diffusion is the gradient descent of an estimation problem with a particular robust error norm taken from the robust statistic field, which deals with problems where the data has large errors or outliers. They also showed that diffusion with Tukey's norm function produces sharper boundaries than the diffusion with the Lorentzian norm (corresponding to the Perona-Malik model [89]) and the L_1 norm (which is equivalent to the TV formulation of Rudin and Osher [83, 84]). Tauber [53] used these results to propose a new anisotropic diffusion model for ultrasound images:

$$\begin{cases} \frac{\partial I(x,y;t)}{\partial t} = \text{div}\left[c(x,y;t)\nabla I(x,y;t)\right] \\ I(x,y;0) = I_0(x,y) \\ \frac{\partial I(x,y;t)}{\partial \overrightarrow{n}} = 0 \qquad \forall_{(x,y)\in\partial\Omega} \end{cases} \tag{4.3}$$

where t is the time, div represents the divergence, ∇I is the intensity gradient, I_0 is the initial image, at time $t = 0$, $\partial\Omega$ is the image boundary, $\overrightarrow{n}$ is the outward normal at the image boundary and $c(x, y; t)$ is the diffusion coefficient, here computed as

the value of the Tukey's function for a pixel (x, y), at time t, and given by

$$c(x,y;t) = \begin{cases} \frac{1}{2}\left[1 - \left(\frac{\text{ICOV}(x,y;t)}{\sigma_s(t)}\right)^2\right]^2 & \text{ICOV} < \sigma_s \\ 0 & \text{ICOV} \geq \sigma_s \end{cases} \tag{4.4}$$

The model described by equation 4.3 uses the Tukey's error norm [90] as the 'edge stopping' function and the ICOV edge detector. One must set $\sigma_s = \sqrt{5}\sigma_e$ in order to obtain forward diffusion when ICOV $< \sigma_e$ and edge enhancement when ICOV $> \sigma_e$ [53, 90].

In ultrasound images, the Tauber's filter offers significant improvement, when compared to other models, in the detection of boundaries of objects. This is a direct consequence of using the ICOV edge detector, well adapted to multiplicative noise, and robust statistics to decide where the diffusion should take place and where it should be inhibited. Nevertheless, it has the inconvenience of destroying some important anatomical boundaries when they have low contrast at bright regions, where the ICOV is weak. An example of this problem can be seen in Fig. 4.5 (b), where the Tauber's model destroyed the weak valley edge pointed by the arrow inside the circle. To overcome this problem, we borrow concepts from the TV theory [83,84] and introduce the following model

$$\begin{cases} \frac{\partial I(x,y;t)}{\partial t} = c(x,y;t)\kappa(x,y;t)\|\nabla I(x,y;t)\| \\ I(x,y;0) = I_0(x,y) \\ \frac{\partial I(x,y;t)}{\partial \vec{n}} = 0 \qquad \forall_{(x,y)\in\partial\Omega} \end{cases} \tag{4.5}$$

where $c(x, y; t)$ is the Tukey's function given by equation 4.4 and $\kappa(x, y)$ is the mean curvature, updated at each time step and given by

$$\kappa(x,y) = \text{div}\left(\frac{\nabla I(x,y)}{\|\nabla I(x,y)\|}\right) \tag{4.6}$$

Equation 4.5 includes the curvature information and keeps the important properties of Tauber's filter. It can be seen as a curvature flow with the Tauber's tensor placed as a spatially varying parameter. As in the Tauber's model, the diffusion is inhibited or completely stopped at places where the ICOV is high. But it also inhibits diffusion where the curvature is small, as is usually expected for anatomical structures. On the other hand, the noise is strongly smoothed out because it usually has high curvature and low ICOV. As can be seen in Fig. 4.5 (c), our filter not only

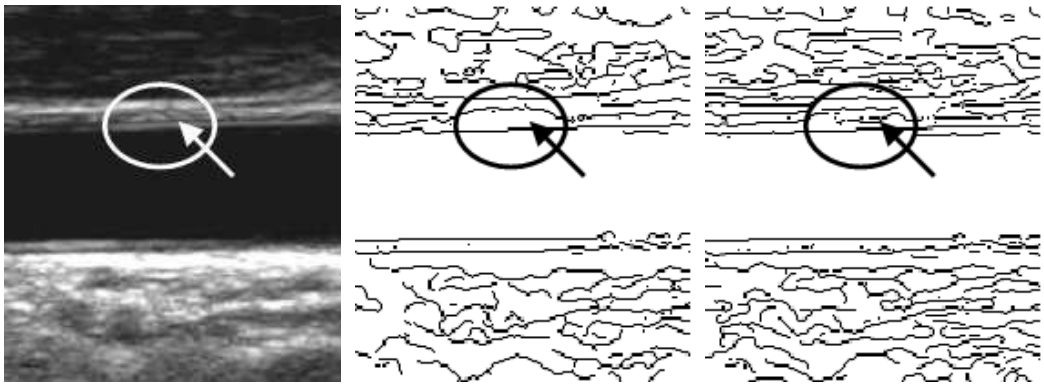

(a) (b) (c)

Fig. 4.5: Edge maps produced by non-linear image filtering: a) Part of a longitudinal section of a CCA, with a weak valley edge pointed by an arrow; b) The edge map produced by the Tauber's anisotropic filter shows a completely destroyed valley edge inside the marking circle and some degradation of its position outside the circle; c) The edge map produced by our filter shows a better preservation and localization of the weak valley edge.

produces well localized edges but it is also able to preserve important anatomical boundaries that are destroyed by the Tauber's filter.

We used a similar numerical scheme to the one found in [53] for the PDE in equation 4.3 and the numerical scheme proposed in [85] for equation 4.5.

4.6 Edge map

Once we have a smooth image, obtained with the proposed non-linear image filter, we need to select the stronger edges. We use the non-maxima suppression with hysteresis algorithm, a popular scheme introduced in [67] that works well. However, in our case, the gradient norm is replaced by the ICOV. In other words, instead of using $\|\nabla I\|(\cos(\theta), \sin(\theta))$, where θ is the gradient orientation, we use ICOV $(\cos(\theta), \sin(\theta))$, thus replacing the gradient norm by the ICOV for the edge strength, but keeping the gradient orientation information. In the non-maxima suppression, the edge map will be the set of pixels that are local maxima of the ICOV in the direction of the gradient and have ICOV value above a specified threshold, T_1. The hysteresis consists in keeping also weaker edges that are local maxima as long as they have an ICOV value above a second threshold, $T_2 < T_1$, and are connected to the stronger edges by some path of edge pixels. We use equation 4.2 to compute σ_e for the final smooth image and set $T_1 = \sigma_e$. A good range for the second threshold

is $T_1/3 < T_2 < T_1/2$ [67]. Therefore, we set $T_2 = 0.4T_1$. Finally, the edge map is processed by the morphological thinning algorithm introduced in [91], which is known to produce good results.

4.6.1 Dominant gradient direction

An additional step that became necessary at this stage, for the subsequent spline fitting in longitudinal sections of the carotid, was the reduction of the gradient orientation errors. This error reduction may be achieved through the computation of the local dominant gradient direction, at each image pixel. This step will not be necessary for transversal sections, but all other edge map operations, described in the next subsections, are common to both longitudinal and transversal sections of the carotid.

The dominant gradient direction is computed with an iterative procedure. Let $\nabla I^n_{i,j}$ be the intensity gradient for pixel (i, j), at iteration n, and ∇I^{n-1}_k the gradient for the k^{th} pixel in the 8-neighborhood of (i, j), at iteration $n-1$. We compute $\nabla I^n_{i,j}$ as the average of ∇I^{n-1}_k, for $k = 1, 2, ..., 9$:

$$\nabla I^n_{i,j} = \frac{1}{9} \sum_{k=1}^{9} \nabla I^{n-1}_k \tag{4.7}$$

To avoid the interference of close contours with very different orientation (e.g., as in valley shaped edges), gradients with opposite direction to the gradient of the central pixel should not be included in the gradient average. We consider that two vectors have opposite direction if their inner product is negative, which is equivalent to an angle larger than 90° between them. Let β_k be the angle between the gradient of the central pixel, (i, j), and the gradient of each of its 8 neighbors. Then, β_k should be less than 45° in order to guarantee a positive inner product for all pairs of gradients used in equation 4.7.

We expect that pixels in homogeneous regions will have no local dominant direction, unless they are close to a region boundary. This will also happen for some of the detected edge pixels, due to noise. Where there is no local dominant direction, its value may drift, from iteration to iteration, and may not stabilize. The changes of the gradient orientation at these pixels may be seen as outliers when compared to the rest of the population, for which the gradient change becomes smaller at each iteration. On the other hand, a small fraction of the edge pixels (whose detection depends on the gradient direction) will disappear and new ones will arise as the gra-

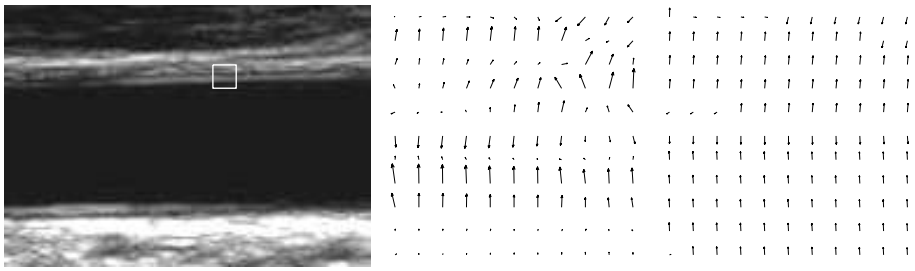

(a) (b) (c)

Fig. 4.6: Example of the gradient direction improvement introduced by the dominant direction computation: a) Part of a longitudinal section of a CCA with a selected sampling box; b) Sample of the gradient map before computation of the dominant direction; c) The same sample after computation of the dominant direction.

dient orientation changes. Since only a small fraction of the edge map will change (usually less than 5%), the initial edge map is a good estimate of the final edges and may be used as a representative sample of the edge population, with a few outliers included. Therefore, we use the edge pixels of the initial edge map as a reference to evaluate the stability of the gradient orientation.

In the evaluation of the stopping criterion, we want to include all inliers and discard the outliers, at least those for which the gradient orientation does not stabilize. Let α be the random variable representing the angle change in the gradient orientation between consecutive iterations, at each edge pixel of the initial edge map. We know, from robust statistics, that $\sigma_\alpha = C\text{MAD}(\alpha) + \text{med}(\alpha)$ gives us a good estimate of the threshold at which the outliers start to appear [53]. To get a robust estimate of the threshold, σ_α^*, above which we expect no inliers, we appeal to the Tukey's error norm, and set $\sigma_\alpha^* = \sqrt{5}\sigma_\alpha$ [90]. Iterations are stopped when the value of α is less than a small angle, ϵ, for all inliers. In other words, we stop the iterations when $\sigma_\alpha^* < \epsilon$. We set $\epsilon = 0.1°$, to guarantee a good stability to all inliers.

Figure 4.6 shows an example of the gradient map in a zoomed window, before and after the weighted average filtering.

4.6.2 Edge map cleaning

Since the computational effort of the RANSAC algorithm, described in section 4.7, is proportional to the number of edge points in the edge map, one should remove all edge pixels that are incompatible with the boundaries we are looking for.

We know that, in ultrasound images of the carotid, the tissues surrounding the

artery wall from the outside are brighter than the tissues inside the artery. Therefore, we should neglect all edges with gradient pointing to the interior of the artery. This can be easily done if we have a rough estimate of the lumen axis, computed automatically or specified by the user. Let $\gamma(i, j)$ be the angle, at a given pixel, (i, j), between the intensity gradient and the gradient of the distance map to the medial axis or the lumen centroid. If $\gamma_{\max}$ is the threshold above which the probability of finding an edge pixel of the carotid wall is virtually zero, then all edge pixels for which $\gamma(i, j) > \gamma_{\max}$ may be removed from the edge map.

All edge pixels in the image ROI, described in section 4.3, that have a distance to the lumen axis larger than a certain threshold, $d_{\max}$, are also removed from the edge map.

The ICOV edge detector tends to produce many false edges in dark regions when the image is very noisy, due to its higher sensitivity at lower intensities. We may clean many of these false edges using the signed distance map to the lumen boundary, SDL, described in section 4.4. All pixels with signed distance outside the range $\text{SDL}_{\min} < \text{SDL} < \text{SDL}_{\max}$ are removed. The determination of these two thresholds will be discussed in section 4.9.

Figure 4.7 shows an example of the edge map before and after the selection of the important edges using the above mentioned criteria.

In longitudinal sections, the cleaned edge map is divided into two independent edge maps, one with the edges above and the other with the edges below the medial axis, which are separately fed to the RANSAC algorithm. This partitioning is not done in transversal sections.

4.6.3 Valley edge map

One of the discriminating characteristics of the carotid boundary is its typical intensity profile in the shape of a valley, also called 'double line' pattern [20]. To use this information we compute the image valley edge map.

As illustrated in Fig. 4.8 (a), we start by searching, up to a certain distance, L, the first local intensity maximum in both directions along the line defined by each edge point, e, and the intensity gradient at that point, $\nabla I(e)$. The intensity profile of a valley edge has two intensity peaks, a and b, being one of these usually shorter than the other. Due to the strong noise in these images, some step edges may also have a double peak intensity profile, but their lower peak will be weak. Therefore, all profiles with only one peak or a weak lower peak should be classified

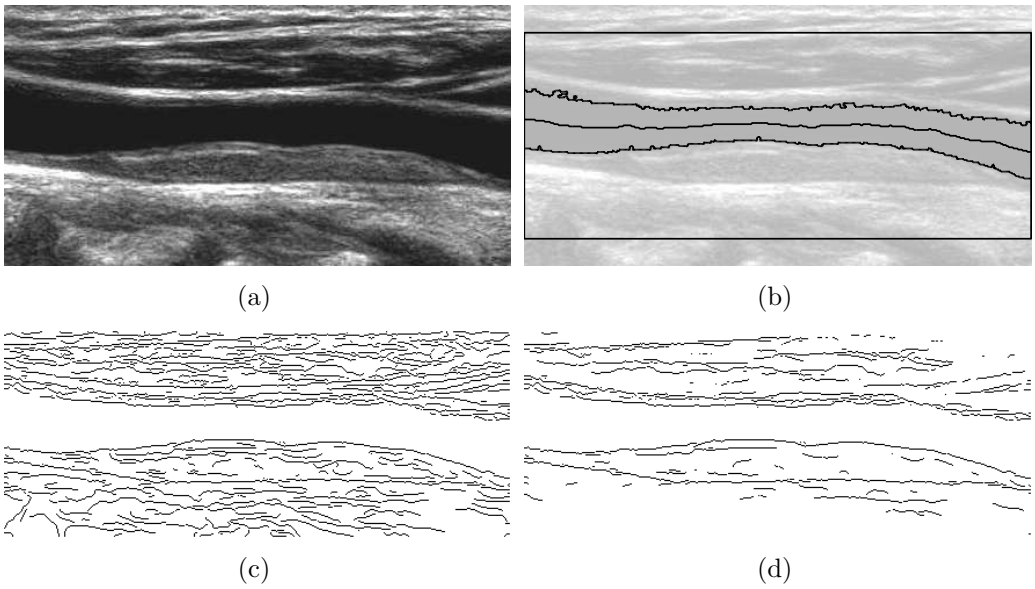

Fig. 4.7: Example of the edge map cleaning: a) Longitudinal B-scan of the CCA; b) Estimated medial axis, ROI box and lumen boundary superimposed on a faded version of image (a); c) Complete edge map of the ROI; d) Edge map of the ROI after cleaning.

as step edges. The other intensity profiles, with a strong lower peak, will be valley edges. To detect the strong lower peaks, we may use an approach similar to the edge detection scheme described for the edge map, at the beginning of this section. If we use hysteresis and if A is a random variable representing the amplitude of the lower peak, we may set the high threshold to $T_A = C\text{MAD}(A) + \text{med}(A)$ and the low threshold to $0.4T_A$. However, experimentation showed that using only the lower threshold is better because it captures more valley edges without a significant increase in noise. Therefore, in our algorithm, an edge pixel is classified as a valley edge if $A > 0.4T_A$. As an example, the valley edge map for the ROI of Fig. 4.7 is presented in Fig. 4.8 (b).

4.7 Random Sample Consensus (RANSAC)

Since the introduction of the RANSAC algorithm [82], a huge amount of work has been published concerning improvements to the algorithm or its use in different areas, including computer vision. A brief list of possible applications of the RANSAC algorithm may be found in [92]. We could not find any application to the segmentation of ultrasound images of the carotid.

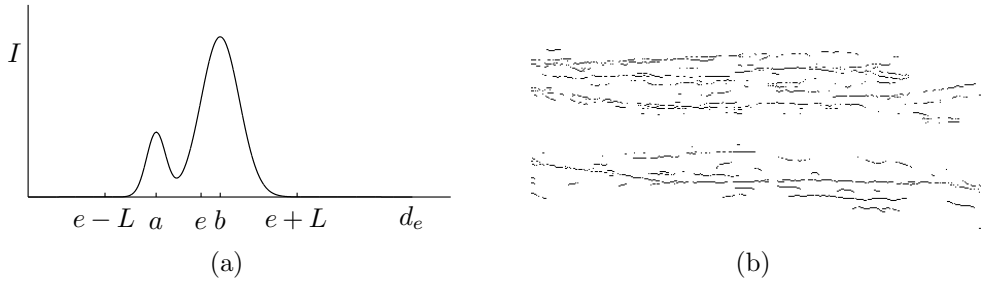

Fig. 4.8: Valley edges: a) Illustration of an intensity valley, where: I is the intensity, e is the location of the edge, d_e is the distance from the edge in the direction of its intensity gradient, $\nabla I(e)$, a is the location of the small peak, b is the location of the large peak, and L is the maximum distance of search; b) Valley edge map for the ROI of Fig. 4.7.

This algorithm deals with the problem of estimating the parameters of a model from a data set containing a large number of outliers. Its main attraction comes from the fact that it is simple and works well in practice. It works by repeatedly extracting from the set of data points a random sample, with the minimum size required to determine the model parameters. For example, if the model is a straight line, samples of two points will be drawn, while samples of 5 points are needed if the model is an ellipse. The consensus of the model, determined for the drawn sample, is evaluated for the rest of the population. The model with the best consensus is selected. The number of inliers, defined as the data points closer to the model than a certain threshold, is the most common criterion for the consensus evaluation. The process is terminated when there is a high confidence of having drawn at least one good sample.

One way of estimating the minimum number of samples necessary to get this confidence is to determine the number of samples that guarantees a low probability of obtaining only bad samples [93]. Another way is to add a few standard-deviations to the expected number of samples necessary to get a good sample [93]. We adopted this last formulation, which is expressed as:

$$\begin{aligned} k &> \mu + N\sigma \\ &> \omega^{-n} + N\frac{\sqrt{1-\omega^n}}{\omega^n} \\ &> \left(1 + N\sqrt{1-\omega^n}\right)/\omega^n \end{aligned} \tag{4.8}$$

where k is the number of drawn samples, μ is the expected number of draws re-

quired to get one good sample, σ is the corresponding standard-deviation, n is the size of the sample, ω is the probability of a good point and N is the number of standard-deviations added to the mean.

The idea behind this formulation comes from the fact that, if x is a random variable, with mean μ and standard-deviation σ, we have [93]

$$P(|x - \mu| \geq \epsilon) \leq \left(\frac{\sigma}{\epsilon}\right)^2 \tag{4.9}$$

where ϵ is a positive value. Making $\epsilon = N\sigma$, we get

$$P(|x - \mu| \geq N\sigma) \leq \frac{1}{N^2} \tag{4.10}$$

In theory, the addition of a few standard-deviations to the mean should be enough. However, in practice, the number of necessary draws is frequently higher, due to the errors affecting the inliers.

4.7.1 RANSAC-based carotid wall segmentation

We need an estimate of the proportion of inliers, ω, in the data set. The usual procedure is to classify as good samples those that lead to a model with a good data consensus and use the ratio between the number of good samples and the total number of drawn samples as an estimate of ω^n, the probability of a good sample. In our case, the value of the gain function described in subsection 4.7.4 proved to be, in practice, a more reliable estimate of ω. This is also more convenient because it doesn't need any extra computations.

Another important difference of our approach, compared to more conventional implementations of the RANSAC algorithm, is the fact that we take advantage from *a priori* knowledge concerning the spatial distribution of the inliers. In longitudinal sections of the CCA, the carotid boundaries can be represented as functions of the type $y = f(x)$. Therefore, samples of points with repeated abscissas, i.e., along the same vertical line, cannot be good samples and should not be considered. In the case of transversal sections of the CCA, the carotid wall contour has an ellipsoidal shape and samples of points along radial line segments centered at the contour centroid should be discarded. With this property in mind, instead of a set of n points, we draw a set of n abscissas, in longitudinal sections, or n orientations taking the centroid as the origin, in transversal sections. Throughout the text, both cases will be generally called samples of n line segments.

Usually, there are several edge points for each line segment (see Fig. 4.11). The samples of edge points are built from a set of n randomly chosen line segments. The k^{th} point of the sample is taken from the k^{th} line segment. Each sample of line segments will usually produce a large number of point samples, given by $\prod_{k=1}^{n} m_k$, where m_k is the number of edge points found in the k^{th} line segment.

Some of the line segments may not have a good point. The probability of finding a good point is

$$\omega_p = P(\text{'good line segment'})P(\text{'good point'/'good line segment'}) \tag{4.11}$$

After drawing a sample of n line segments, we could proceed and choose, randomly, one edge point from each drawn line segment, to get the final sample of n points, and set $\omega = \omega_p$ in equation 4.8. But it is more efficient to set $\omega = P(\text{'good line segment'})$ and to evaluate all combinations of n edge points for each sample of n line segments (see appendix B for a proof).

In our implementation, the minimum number of samples of line segments is estimated dynamically and the procedure is terminated when the number of drawn samples exceeds the estimated minimum.

4.7.2 Carotid wall model in longitudinal sections

The chosen model to look for in the image is the classical complete cubic spline, which proved to be able to adequately follow the CCA boundaries in longitudinal sections.

Determination of the spline parameters

Each spline has only 5 control points, corresponding to 4 cubic polynomials, which are enough to give the model some flexibility while keeping it robust to noise. This also means the RANSAC samples will have a size $n = 5$.

For each sample of 5 points, we have to compute the spline parameters. This implies solving a 5×5 system of linear equations, which can be done very efficiently with the Crout factorization algorithm for tridiagonal systems [94].

The spline determination relies on the intensity gradient orientation at the end points, requiring a good degree of confidence in the gradient orientation at each edge point. This confidence is achieved through the estimation of the local dominant direction of the gradient, as described in subsection 4.6.1. An alternative approach

would be to complete the spline at the expense of two extra points, avoiding the gradient information in the spline determination. In fact, we have tried this approach with success. However, this solution has the drawback of requiring larger samples and, subsequently, a significant increase in the computational effort of the RANSAC algorithm.

RANSAC sample

The samples of edge points are built from a set of 5 vertical line segments, defined by a set of 5 random abscissas. The segments go from the estimated medial axis of the lumen to a certain distance threshold, $d_{\max}$, above or bellow the axis, depending on the searched contour being located above or bellow the lumen, respectively.

Normal to the spline

The spline normal is easy to compute, once the spline parameters are determined. We build the function $F(x, y) = y - P_j(x)$ for the lower carotid boundary or $F(x, y) = P_j(x) - y$ for the upper boundary, where $P_j(x)$ is the polynomial defining the spline at x. Then, at point (x_0, y_0), the normal vector will be $(F_x(x_0, y_0), F_y(x_0, y_0))$ and the slope will be $-F_x(x_0, y_0)/F_y(x_0, y_0)$, where F_x and F_y are the partial derivatives of F. Obviously, a sample of points is immediately rejected if $F_y = 0$ for any of its points.

Digital spline

The spline points usually fall between pixel positions, therefore requiring an interpolation of the image information, which introduces some additional computations in the evaluation of the spline consensus. The digital spline is an integer-valued version where each real-valued spline point is represented by the closest pixel in a digital image. It is easily obtained by rounding the real-valued spline at each abscissa. The digital spline is used in the consensus evaluation because no interpolation is required and it is enough to find a good estimate of the best spline fit. As discussed in section 4.8, the best spline returned by the RANSAC algorithm can be refined afterwords, using the real-valued spline, interpolation and a minimization algorithm.

Bail-out tests

The spline consensus evaluation has a significant contribution to the total computational effort of the RANSAC algorithm. To alleviate this burden we use two

bail-out tests. The first one rejects any sample of n abscissas not well spread along the columns of the image, in order to guarantee a good support for the spline model. This restriction may be introduced in a very efficient way by excluding from the list of image columns the column corresponding to the last drawn abscissa and all its neighbor columns, up to a specified distance, Δ, before drawing another abscissa. To get a good distribution of the random values over the interval, $[a, b]$, of image columns, we set $\Delta = \frac{b-a}{2(n+1)}$, where n is the size of the sample. In longitudinal sections we have $\Delta = (m-1)/12$, where m is the number of columns in the image, since $n = 5$ (4 polynomials), $a = 1$ and $b = m$. The second bail-out test rejects any sample of n points if the angle, θ, between the gradient intensity and the spline normal is larger than a certain threshold, σ_θ, at any point of the sample. The value of σ_θ will be discussed in section 4.9. The spline consensus is computed only for samples that are not rejected by the bail-out tests.

4.7.3 Carotid wall model in transversal sections

Inspired by the wall model adopted in longitudinal sections, a periodic cubic spline was tried for transversal sections. In this case, the model is completely determined by the 2D coordinates of the sample of points drawn from the edge map. This means the gradient information is not needed to determine the spline parameters.

The periodic cubic spline was implemented as the curve $(x(t), y(t))$, parameterized by $0 \leq t \leq 2\pi$. For a sample of n points ordered by ascending value of t, an additional point, (x_{n+1}, y_{n+1}), is created such that $t_{n+1} = t_1 + 2\pi$, $x(t_{n+1}) = x(t_1)$ and $y(t_{n+1}) = y(t_1)$. The determination of each periodic cubic spline requires the resolution of two systems of $n+1$ linear equations, one for $x(t)$ and another for $y(t)$. The first system is completed with the conditions $x'(t_{n+1}) = x'(t_1)$ and $x''(t_{n+1}) = x''(t_1)$, where $x'(t)$ and $x''(t)$ represent the first and second order derivatives of x at t, respectively. Analogously, the second system of equations is completed with the restrictions $y'(t_{n+1}) = y'(t_1)$, and $y''(t_{n+1}) = y''(t_1)$. These systems are not tridiagonal, so they cannot be solved by the Crout factorization algorithm [94]. But they are almost tridiagonal and efficient numerical schemes based on the LU factorization [94] can still be used.

The complete spline tends to take the shortest smooth path between the n sample points. This path may turn away from the wall contour between the control points. Still, if n is large enough, this model produces good segmentations. Experimentation showed the algorithm usually gives bad results when $n < 5$. Some typical results

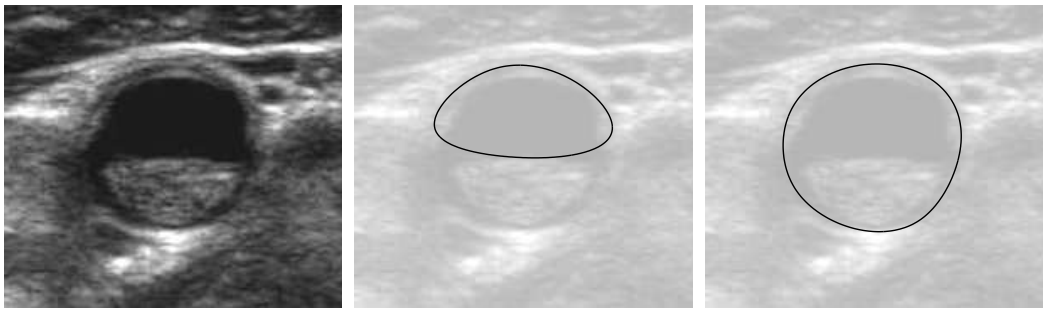

(a) (b) (c)

Fig. 4.9: Segmentation of a transversal section with a periodic 2D spline: a) Image to segment; b) Best cubic spline for $n = 4$; c) Best cubic spline for $n = 5$.

are presented in Fig. 4.9.

Unfortunately, for $n = 5$, it usually takes several minutes, in a modern computer, to finish each segmentation. Naturally, with a larger sample size things become much worse. This motivated us to look for an alternative model.

In transversal sections, the carotid wall contour has an approximate ellipsoidal shape. In fact, the ellipse model was used in manual segmentation in a recently published work [78]. The ellipse turned out to be a good model prior because it produces good enough results and it is several times faster than the periodic spline.

Determination of the ellipse parameters

As shown in Fig. 4.10, an ellipse is completely defined by five parameters: A, the length of its major semi-axis; B, the length of its minor semi-axis; x_c, the abscissa of its centroid; y_c, the ordinate of its centroid; and θ, the rotation angle.

The ellipse can also be represented implicitly as the zero level set of the function

$$F(x, y) = ax^2 + bxy + cy^2 + dx + ey + f \tag{4.12}$$

The equation $F(x, y) = 0$ is known as the general conic equation and we have an ellipse if $b^2 - 4ac < 0$ [95]. This implicit representation is more attractive in the computation of the ellipse parameters and the normals to the ellipse, which will be needed in the RANSAC search.

The conic parameters can be determined uniquely from five points in the plane, (x_i, y_i), $1 \leq i \leq 5$. If we divide equation $F(x, y) = 0$ by a, its first coefficient becomes unity and we get an equivalent equation with only five unknowns. Therefore, we

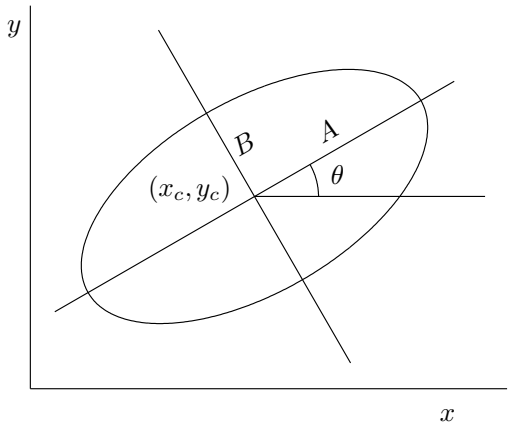

Fig. 4.10: Ellipse parameters.

may choose $a = 1$ and determine the other coefficients of $F(x, y)$ by solving the following system of five linear equations:

$$x_i y_i b + y_i^2 c + x_i d + y_i e + f = -x_i^2 \quad ; \quad 1 \leq i \leq 5 \tag{4.13}$$

RANSAC sample

Each RANSAC sample will have size $n = 5$, which is the number of points needed to determine the ellipse. For transversal contours, the samples of edge points are built from a set of 5 radial line segments, with random orientations, centered at the estimated lumen centroid and going up to a maximum distance $d_{\max}$, as illustrated in Fig. 4.11. First, 5 random orientations are chosen, one for each radial segment. Then, we look for edge points along each radial line segment, digitized with a Bresenham algorithm [87]. The k^{th} point of the sample is taken from the k^{th} radial segment.

Normal to the ellipse

The gradient of the conic function, $\nabla F(x, y) = (F_x(x, y), F_y(x, y))$, is normal to the ellipse. Moreover, it points outwards if $a = 1$ (see appendix A for a proof).

Digital ellipse

The ellipse may be computed as the set of points (x, y), parametrized by ϕ as

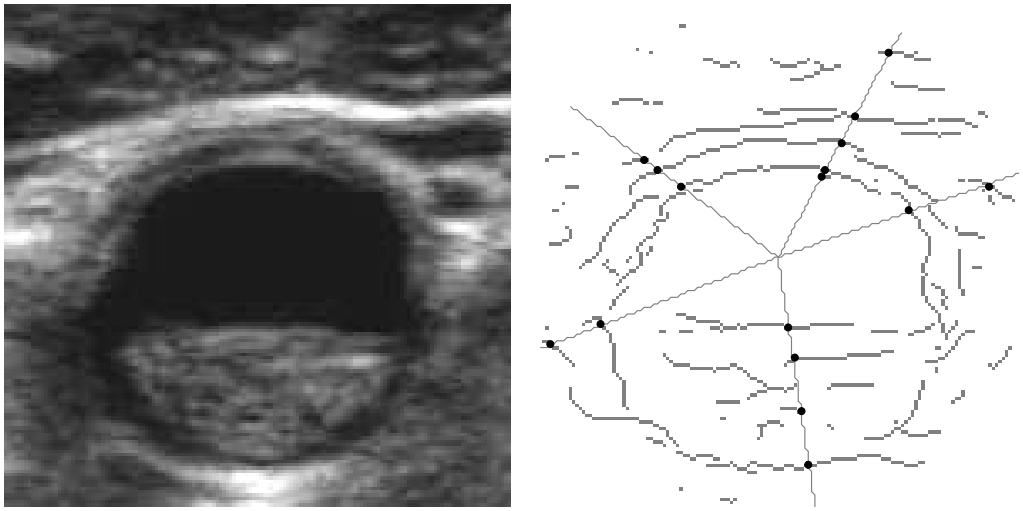

Fig. 4.11: Radial carotid lines: a) Image to be segmented; b) Edge map, radial lines and intersected edges points.

$$\begin{bmatrix} x \\ y \end{bmatrix} = R(\theta) \begin{bmatrix} Acos(\phi) \\ Bsin(\phi) \end{bmatrix} + \begin{bmatrix} x_c \\ y_c \end{bmatrix} \tag{4.14}$$

where $R(\theta)$ is a rotation matrix and $0 \leq \phi < 2\pi$. But this approach has three disadvantages. First, the 5 ellipse parameters in equation 4.14 need to be computed from the conic parameters obtained from the linear system 4.13. Second, one needs to compute two trigonometric functions and one geometric transformation for each ellipse point. Third, the ellipse points usually fall between pixel positions and the image information has to be interpolated.

The digital ellipse is enough to find a good estimate of the best ellipse fit and the computation complexity is much lower. The best ellipse returned by the RANSAC algorithm can be improved afterwords, as discussed in subsection 4.8.

One way to get the positions of the set of pixels of the digital ellipse is to adapt the midpoint algorithm [87] to the general conic equation and apply it over the entire elliptical path. But we propose the following algorithm, which looks simpler:

1. Choose one of the five pixels in the random sample as the first point, P_1, of the digital ellipse.

2. Look for the 8-neighbor of P_1 that is closer to the ellipse. This will be the second point, P_2, of the digital ellipse. A good estimate of the distance, d,

from an ellipse to a point, (x_0, y_0), is given by [95]

$$d(x_0, y_0) = \frac{F(x_0, y_0)}{\|\nabla F(x_0, y_0)\|} \tag{4.15}$$

A less reliable distance estimate is $d(x_0, y_0) = F(x_0, y_0)$ [95]. But this one is computationally lighter and is enough for our needs, since we only want to compare distances in the close vicinity of the zero level set of $F(x, y)$.

3. A new point, P_{i+1}, of the digital ellipse is searched only in five of the 8 neighbors of the last saved point, P_i, chosen as a function of the direction formed by the last pair of saved points, P_{i-1} and P_i. For instance, if P_{i-1} is the pixel to the west of P_i, then the candidates to P_{i+1} are the pixels to the north, northeast, east, southeast and south of P_i.

4. If the new point is different from the first, save it and go back to the previous step. Otherwise, don't save the new point and finish.

Bail-out tests

As in longitudinal sections, some bail-out tests were introduced in transversal sections, before the RANSAC consensus evaluation, to reduce the total computational effort of the RANSAC search.

Four bail-out tests were used here. The first one comes before the conic computation. It rejects any sample of 5 radial segments not well spread along the range $[0, 2\pi[$, in order to guarantee a good support for the ellipse model. To implement this restriction in an efficient way, the angle interval is previously divided into a list of 360 integers, α_k, from 0 to 359 degrees. The last drawn angle is excluded from the list as well as all the neighboring angles, up to a specified distance, Δ, before drawing another angle from the remaining list. By analogy to what was done in the longitudinal case, we set $\Delta = \frac{2\pi - 0}{2(n+1)} = \pi/6$, where $n = 5$ is the size of the sample for ellipses. After the fifth extraction, each of the 5 angle estimates, α_k, is relaxed from the integer restriction by a second random extraction in the interval $[\alpha_k - 1, \alpha_k + 1]$. This way, any real-valued angle can be generated. All random values are generated from a uniform distribution.

The remaining three bail-out tests are applied to the conic generated by each sample of 5 points. The conic is immediately rejected if any of the following conditions is true:

1. $b^2 - 4ac \geq 0$, which means the conic is not an ellipse.

2. The ellipse is too eccentric. The eccentricity of an ellipse (Fig. 4.10) is given by $\epsilon = \sqrt{1 - (B/A)^2}$, where $0 \leq \epsilon < 1$. It is minimum for a circle, where $A = B$ and $\epsilon = 0$, and increases with the length difference between the major (A) and minor (B) axis. The wall contours in transversal sections have very low eccentricity since the slices are approximately normal to the major axis of the artery. This knowledge is used to reject any generated ellipse with eccentricity above a certain threshold.

3. The angle, θ, between the gradient intensity and the outward normal to the ellipse is larger than a certain threshold, σ_θ, at any point of the sample.

The values of σ_θ and the eccentricity threshold will be discussed in section 4.9.

Some other differences from the spline model

The local dominant direction filter, used in longitudinal sections and described in subsection 4.6.1, has two drawbacks. First, it is an iterative process with a relatively slow speed of convergence, making it computationally heavy. Second, the larger weight of the gradients with stronger magnitude makes sense in noisy images and works fine in longitudinal sections, where the contours of interest have a roughly linear nature. But this property of the filter will introduce some undesirable bias in contours with strong non-linearity, like the wall contour in transversal sections. On the other hand, the determination of the ellipse parameters does not need the gradient information. Therefore, in transversal sections, the local dominant filter is not used. This means that some of the segmentation parameters will have different values for longitudinal and transversal sections. These parameters will be presented in section 4.9.

In transversal sections there is only one contour to look for. So, there is no need to split the edge map into parts. The whole cleaned edge map is fed to the RANSAC-based segmentation algorithm.

4.7.4 Gain function

To measure the consensus of the spline, in longitudinal sections, or the consensus of the ellipse, in transversal sections, we use a specially conceived gain function,

presented in equation 4.16, which integrates the response to several discriminating characteristics of the carotid boundaries. Next we will describe the selected characteristics and discuss their introduction in the gain function.

One good discriminating characteristic for carotid boundaries is the valley shaped edge property. In fact, it has already been explored in previous works on CCA segmentation [6, 68]. However, most of the times these valley edges are missing in large extensions of the CCA wall. Moreover, this type of edges can also be found in other anatomical structures surrounding the CCA and they are frequently surpassed in edge strength by other boundaries. This means that it is not a good idea to support our model entirely on this single property and that a direct edge strength evaluation may be deceiving. It seems a better idea to look for any type of edges, giving more emphasis to valley edges and edges closer to the detected lumen boundary. To reduce the influence of other anatomical boundaries in the image, a larger absolute value of the SDL (signed distance to the lumen boundary) should receive a stronger penalty. However, due to the eventual presence of plaque inside the carotid, this penalty should have a slower growth for positive distances (outside the lumen). There should also be a good orientation consistency between the normal to the carotid wall model and the intensity gradient. These observations led us to a gain function that integrates the responses to the following characteristics:

1. distance, *de*, of the carotid wall model (spline or ellipse) to edge points in general;

2. distance, *dve*, to valley type edge points;

3. angle, θ, between the orientation of the normal to the wall model and the intensity gradient;

4. signed distance, SDL, to the lumen boundary, with negative distances inside the lumen.

The way we integrate these characteristics into the gain function should reflect the probability of each wall model point to belong to the carotid boundary. Bearing in mind that the valley edge property is not always present, a wall model point, P_k, is a good candidate to the carotid boundary if it is close to a valley edge pixel *or* a step edge pixel, *and* it has an intensity gradient orientation similar to the orientation of the normal to the wall model *and* it falls inside the expected distance limits to the lumen boundaries. Moreover, the chance of each wall model point being

a good candidate should increase as each characteristic becomes stronger, reaching the maximum at the best fit. The best wall model should be the one with the highest global score for the sum of all its points.

Taking all this into consideration, we arrived at the following global gain function:

$$G = \frac{1}{2m} \sum_{k=1}^{m} \left[g_1(P_k) + g_2(P_k) \right] g_3(P_k) g_4(P_k) \tag{4.16}$$

where m is the number of P_k points of the digital model (spline or ellipse) and $g_j(P_k)$, $1 \leq j \leq 4$, is a fuzzy function representing the contribution of characteristic j at point P_k.

In equation 4.16, the first three fuzzy functions are $g_1(P_k) = f(de(P_k))$, $g_2(P_k) = f(dve(P_k))$ and $g_3(P_k) = f(\theta(P_k))$, where $f(z)$ is the Tukey's function, given in equation 4.17, with scale $\sigma = \sigma_d$ for characteristics de and dve and scale $\sigma = \sigma_\theta$ for characteristic θ.

$$f(z) = \begin{cases} \left[1 - \left(\frac{z}{\sigma} \right)^2 \right]^2 & z < \sigma \\ 0 & z \geq \sigma \end{cases} \tag{4.17}$$

The scale, σ, of each fuzzy function represents the threshold of the corresponding characteristic above which we no longer expect to find any pixel of the carotid boundary.

The fourth fuzzy function of equation 4.16 gives preference to curves that are closer to the lumen boundary, giving larger tolerance to distances outside the lumen. This is expressed as

$$g_4(P_k) = \begin{cases} f^-(-\mathrm{SDL}(P_k)) & \mathrm{SDL}(P_k) < 0 \\ f^+(\mathrm{SDL}(P_k)) & \mathrm{SDL}(P_k) \geq 0 \end{cases} \tag{4.18}$$

where $f^-(z)$ and $f^+(z)$ are given by equation 4.17, with scales $\sigma = \sigma^-$ and $\sigma = \sigma^+$, respectively.

The shapes of our fuzzy functions, plotted in Fig. 4.12, are inspired in the Tukey's function for several reasons: a) its success in the field of robust statistics concerning the treatment of random variables with unknown distribution and the presence of outliers [53]; b) the existence of a robust estimator, based on the MAD statistic, for the scale of the fuzzy function; c) its computational lightness.

This gain function has values in the range $[0, 1]$, where unity means a perfect fit.

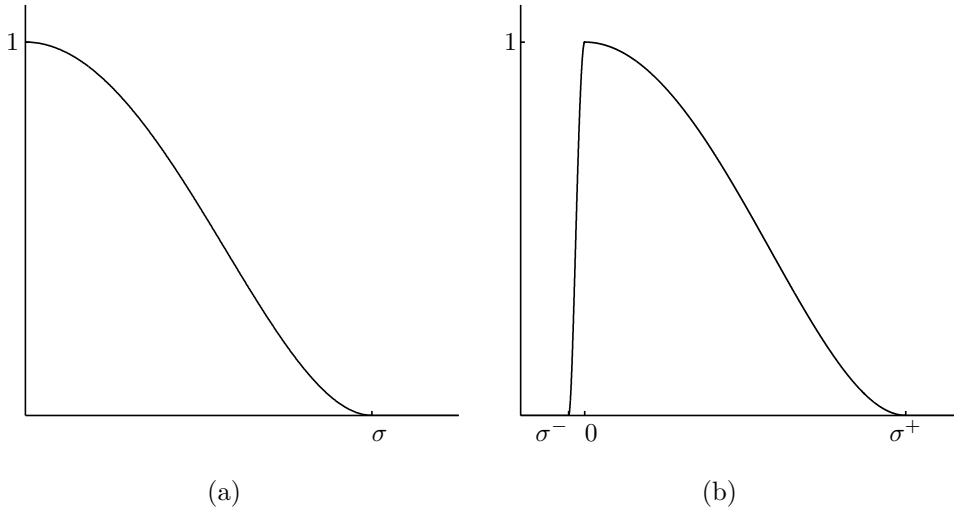

Fig. 4.12: Fuzzy functions used in the gain function: a) $f(z)$; b) $f^{-}(z)$ and $f^{+}(z)$.

Its score reflects, in a fuzzy way, the percentage of good points along the path of the wall model. Therefore, it is well suited to be used as an estimate of the probability, ω, of a good line segment, discussed in section 4.7. A good point is classified in a fuzzy way, which depends on several properties besides the distance to the model. This may seem a conservative estimate of ω, when compared to the usual approach discussed in section 4.7, but it leads to a more realistic estimate of ω, due to the large data errors usually present in these images. It also implies a more realistic estimate of the minimum number of samples to be drawn, given by equation 4.8.

4.8 Simplex search

The best splines and ellipses found by the RANSAC search can be further improved using the real-valued wall model, 2D interpolation and a function minimization with an algorithm like the Nelder-Mead simplex method [96].

The bilinear interpolation is simple and good enough for this purpose.

The points of the real-valued spline are easily obtained by computing the spline value at each image column.

The computation of the real-valued ellipse points is not so simple. We start by computing the first quadrant points of the ellipse at its standard position (without translation or rotation), choosing the independent variable according to the curve slope and incrementing this variable by unit steps. This is done using the following algorithm:

1. $(x_1, y_1) = (0, B)$
2. $i = 1$
3. while $B^2 x_i \leq A^2 y_i$ do
   (a) $i = i + 1$
   (b) $x_i = x_{i-1} + 1$
   (c) $y_i = B\sqrt{1 - (x_i/A)^2}$
4. $y_i = ceil(y_{i-1}) - 1$, where $ceil(z)$ is the smallest integer greater or equal to z.
5. $x_i = A\sqrt{1 - (y_i/B)^2}$
6. while $y_i > 0$ do
   (a) $i = i + 1$
   (b) $y_i = y_{i-1} - 1$
   (c) $x_i = A\sqrt{1 - (y_i/B)^2}$

The points of the other three quadrants are obtained by symmetry. Finally, the rotation and translation are applied to the whole set of ellipse points in the standard position. This procedure gives an approximately uniform spatial distribution of the ellipse points along the elliptical path, such that the distance between consecutive points is close to the distance between two adjacent image pixels.

The simplex algorithm finds a minimum of an unconstrained multivariable function. Therefore, the gain function of equation 4.16 is previously converted to a cost function, C, by changing its sign to negative. The cost function for the ellipse model becomes a function of 5 variables, given by $C = -G(A, B, x_c, y_c, \theta)$. The spline model is defined by the coordinates of the 5 control points so, its cost function depends on 10 variables and is given by $C = -G(x_1, y_1, x_2, y_2, x_3, y_3, x_4, y_4, x_5, y_5)$.

The model estimate returned by the RANSAC algorithm usually falls quite close to the global minimum of the cost function. Therefore, it is a good start for the simplex search, which will converge to a close local minimum, as exemplified in Fig. 4.13. In a modern computer, the Nelder-Mead simplex method [96] finds the local minimum in just a fraction of a second. Unfortunately, the surface of the cost function frequently has several close local minima near the global minimum. As a consequence, the simplex method may not converge to the global minimum, even if

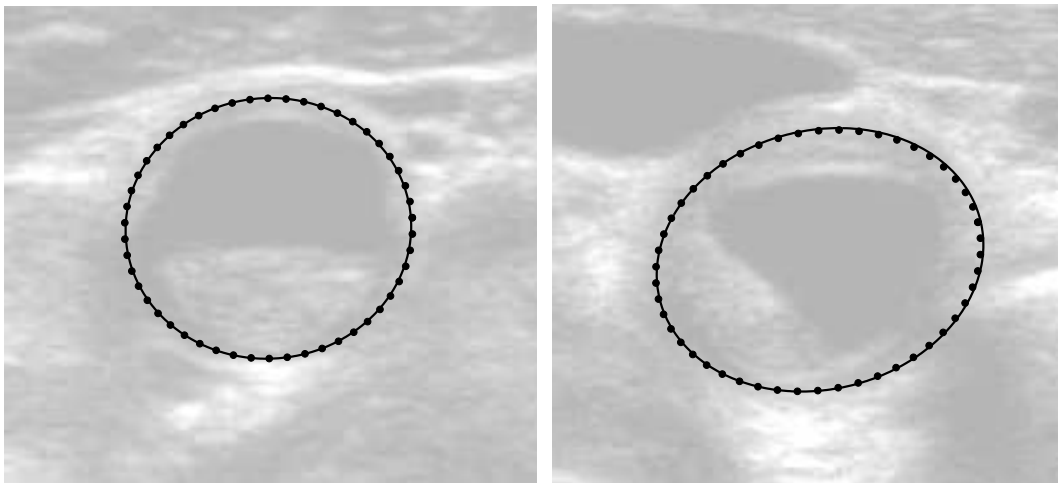

(a) (b)

Fig. 4.13: Simplex method applied to ellipses. The dots represent the best ellipse found by the RANSAC algorithm. The continuous line is the local maximum of the gain function found by the simplex method.

the search starts in its neighborhood. This means there is no guaranty the solution estimated by the RANSAC algorithm will lead the simplex method to the global minimum. On the other hand, the improvement introduced by the simplex search is usually so small that no significant loss will occur if we stick to the RANSAC solution.

4.9 Results

The non-linear image smoothing filter (see equation 4.5) was discretized with the numerical scheme proposed in [85] (see appendix D), where the grid size, h, was normalized to one. The time step was set to $\Delta t = 0.25$, which offers a good convergence speed without loosing numerical stability. The value of the edge scale, σ_e (see equation 4.2), as well as the slope of the corresponding curve, decrease monotonously with increasing iterations. The change in σ_e is proportional to the amount of smoothing generated by the last iteration. Therefore, iterations are stopped when the slope of the σ_e curve falls bellow the threshold 10^{-5}, after which the smoothing increases very slowly.

As stated in [52], the ICOV edge detector was conceived for decompressed B-mode images, which can be estimated by taking the exponential of the compressed B-mode image divided by 25. This decompressed image is used only for the

estimation of the ICOV.

We need a value for N, in equations 4.8 and 4.10, that gives us a high confidence of finding a good sample. In literature related to the RANSAC algorithm (e.g., [92,93]) it is common to find $1/N^2 \approx 0.05$, which gives $N \approx 4.5$. In our case, $N = 5$ is usually enough to capture at least one good sample.

There are several other parameters that have to be determined, in particular:

1. $d_{\max}$, the maximum distance to the lumen medial axis (section 4.3);
2. $\gamma_{\max}$, the maximum value allowed for the angle γ, defined in subsection 4.6.2;
3. $\mathrm{SDL}_{\min}$, the low threshold for SDL, the signed distance to the lumen boundary (subsection 4.6.2);
4. $\mathrm{SDL}_{\max}$, the high threshold for SDL (subsection 4.6.2);
5. L, the maximum distance from each edge pixel in the valley edge map computation (subsection 4.6.3);
6. σ_d;
7. σ_θ;
8. σ^-;
9. σ^+.

where the last four parameters are the scales used in each fuzzy function of the gain function (subsection 4.7.4).

To estimate values for each of the above parameters, we used a set of images manually segmented by a medical expert, for which the resolution was normalized to 0.09 mm, a common resolution used in clinical practice. With the help of the expert, a set of 67 B-mode images of the carotid was selected, from 30 different patients, of which 17 are transversal sections. An image was selected if the medical doctor was able to make at least a rough outline of the whole boundary, both for the carotid wall and the lumen boundary. This means the sample includes cases where the location of the carotid boundaries had to be partially inferred due to gaps along those boundaries. Given the poorer quality of transversal sections, the selection criterion was more difficult to satisfy in these sections than in longitudinal ones. This explains the reduced representation of transversal sections in the selected sample. In

fact, the quality of transversal sections is often too bad for clinical practice, leading to the preference for longitudinal sections by medical experts.

For each image of the sample, both the carotid wall contour and the lumen boundary contour were manually traced by the expert. The lumen medial axis, in longitudinal sections, and the lumen centroid, in transversal sections, are easily determined from the traced lumen boundaries. These manually traced contours were chosen as the ground truth and used to compute some useful statistics.

For our sample of images we found that $d < 70$ pixels, where d is the distance from a carotid wall point to the lumen medial axis. So, we set $d_{\max} = 90$ pixels, in order to keep some of the image data outside the carotid boundaries, which is important, for instance, in the edge map computation. This also gives us a good safety margin for new images.

The complete edge map of each of the manually segmented images was obtained as described in section 4.6. In longitudinal sections, the dominant gradient direction filter, presented in subsection 4.6.1, was also used for this purpose. This filter was not used in transversal sections, due to the reasons discussed in subsection 4.7.3. The value of γ was computed, in the neighborhood of the manually traced carotid boundaries, for the closest edge point along each image column. As expected, some values of γ are outliers, corresponding to noise edges or belonging to other contours that appear in the same neighborhood. Nevertheless, we found that in at least 99% of the cases, $\gamma < 30^\circ$ when the dominant gradient direction filter is used and $\gamma < 65^\circ$ otherwise. So, we set $\gamma_{\max} = 30^\circ$ in longitudinal sections and $\gamma_{\max} = 65^\circ$ in transversal sections.

Parameter $\mathrm{SDL}_{\min}$ represents the threshold of SDL below which we expect to find no edge pixel of the carotid wall. For all images of our sample it was observed that $\mathrm{SDL} > -6.4$. Therefore, we set $\mathrm{SDL}_{\min} = -7$ and $\sigma^- = -\mathrm{SDL}_{\min} = 7$. On the other hand, parameters $\mathrm{SDL}_{\max}$ and σ^+ represent the threshold of SDL above which we expect to find no edge pixel of the carotid wall. A natural value for this threshold is $d_{\max}$. So we set $\mathrm{SDL}_{\max} = \sigma^+ = d_{\max}$.

The width measurement of the valley edges in our sample of images showed that $L = 10$ is enough for valley edges belonging to the carotid wall.

To estimate the values of σ_d and σ_θ, we computed the values of de and θ, defined in subsection 4.7.4, for each point of the manually traced carotid walls in our set of images. Parameter θ was computed from the image gradient map, obtained with and without the local dominant gradient direction filter. Parameter de was computed from the cleaned edge map, described in subsection 4.6.2. Parameters

σ_d and σ_θ are scales of Tukey's functions. Therefore, they may be computed as $\sigma_d = \sqrt{5}\,[C\text{MAD}(de) + \text{med}(de)]$ and $\sigma_\theta = \sqrt{5}\,[C\text{MAD}(\theta) + \text{med}(\theta)]$, respectively. We found the value $\sigma_\theta \approx 11°$, when the dominant gradient filter is used, or $\sigma_\theta \approx 36°$, when this filter is not used. In both cases we found $\sigma_d \approx 4$ since this parameter is not significantly influenced by the gradient map.

Two parameters of the bail-out tests used in the RANSAC algorithm were also determined from the image data base, in particular:

1. The limit for the angle, θ, between the intensity gradient and the normal to the carotid wall model (spline or ellipse) at the sample points. Its value is given by the threshold σ_θ, also used in the gain function and already discussed above.

2. The maximum eccentricity, ϵ, allowed for an ellipse. We haven't found any case of a transversal section of the carotid with eccentricity above 0.7. So, an ellipse is immediately rejected if $\epsilon \geq 0.75$, a threshold that includes a comfortable safety margin. In other words, an ellipse is rejected if its minor axis is less than approximately 66% of the major axis.

Some examples of the carotid walls segmented by our model are presented in Fig. 4.14-4.16, including a case of successful segmentation in the presence of graphical markings placed by the medical doctor during the image acquisition. In the examples of Fig. 4.16, a comparison is made between the manual contours and the ones obtained with our algorithm.

The value of the gain function (equation 4.16) obtained for the lower spline in Fig. 4.14 (f) is an example of an underestimated probability of a good abscissa due to the influence of a thick carotid plaque. In this case, the plaque region pushes the lumen boundary away from the wall boundary, reducing the value of the SDL factor (fourth fuzzy function) in the gain function. A consequence of this underestimated probability is an increase in the number of samples analyzed by the RANSAC algorithm, which means an increase in the confidence of the fitted wall model, at the cost of some additional computational effort. The quality of the segmentation is not affected. In fact, the segmentation result in this example is quite good, illustrating the robustness of the algorithm to the presence of large plaques.

The gain function usually shows a weaker response in transversal sections because: a) in these sections the dominant gradient orientation filter is not used and, therefore, the intensity gradient has a larger variability; b) the ellipse model is not

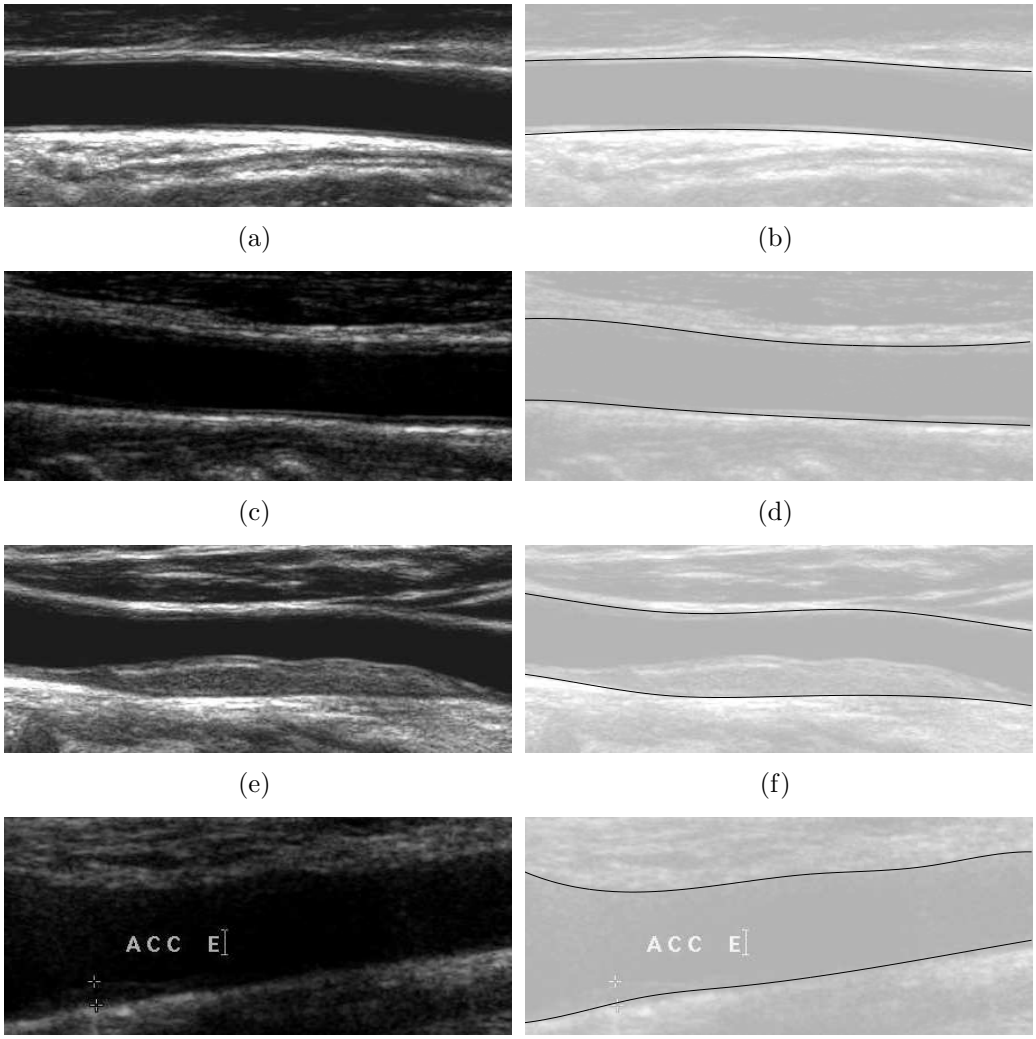

Fig. 4.14: Examples of segmented carotid walls in longitudinal B-scans of the CCA: a) Carotid with no plaque; b) Faded version of (a) and the best computed splines, in black, above and below the lumen, with gain function $G_a \approx 71.3\%$ and $G_b \approx 81.9\%$, respectively; c) Carotid with no plaque; d) Faded version of (c) and best splines, with $G_a \approx 57.2\%$ and $G_b \approx 68.9\%$; e) Carotid with extensive plaque; f) Faded version of (e) and best splines, with $G_a \approx 62.5\%$ and $G_b \approx 54.0\%$; g) Carotid with plaque and graphical markings placed during acquisition; h) Faded version of (g) and best splines, with $G_a \approx 45.7\%$ and $G_b \approx 50.3\%$.

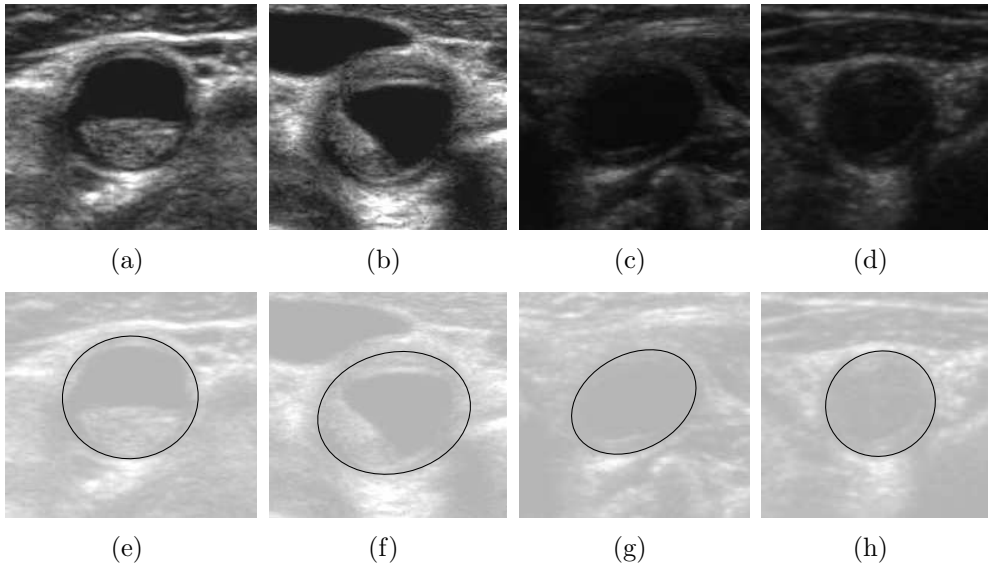

Fig. 4.15: Examples of segmented carotid walls in transversal B-scans of the CCA: a-d) Original images; e-h) Faded versions of the images and the best computed ellipses, with gain function values $G \approx 39.2\%$, $G \approx 33.3\%$, $G \approx 46.3\%$ and $G \approx 50.0\%$, respectivelly.

so flexible as the spline model and cannot capture any deviation of the wall contour from the elliptical shape.

Next we present some quantitative results for the carotid wall segmentation, computed for our set of images and using the manual segmentations as the ground truth.

A contour detection was considered successful if the maximum distance of the detected contour to the ground truth was smaller than 1 mm. This criterion was not fulfilled in 14.0% of the longitudinal contours and in 11.8% of the transversal contours. Since there are two independent wall contours to be detected in each longitudinal section and one wall contour in each transversal section, we can conclude that 15 out of 17 transversal contours and 86 out of 100 longitudinal contours were successfully detected. Failures in the segmentation of the carotid wall may occur if there are stronger and nearby boundaries with similar properties to the wall boundary, specially when the wall boundary is badly defined over a large fraction of its length. Some examples of failure are given in Fig. 4.17. The longitudinal examples and several other images in our sample include a large part of the internal carotid, which is a more complex region than the CCA and increases the detection difficulty. Nevertheless, we confirmed that our algorithm can correctly detect most

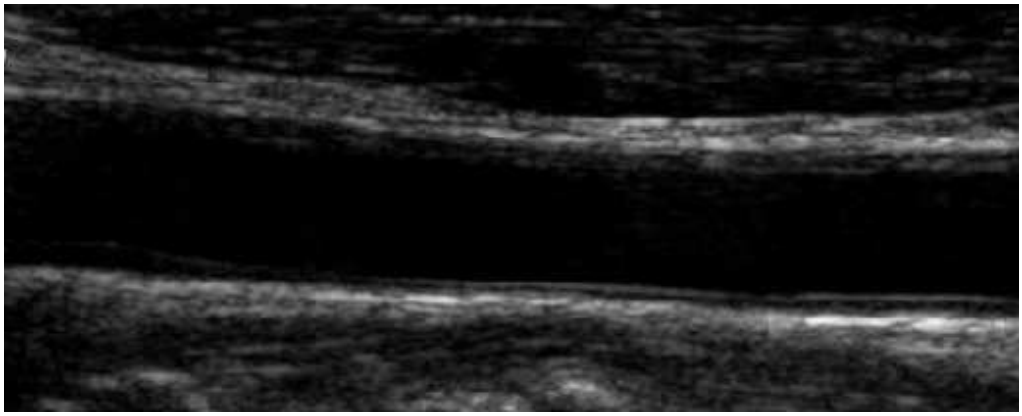

(a)

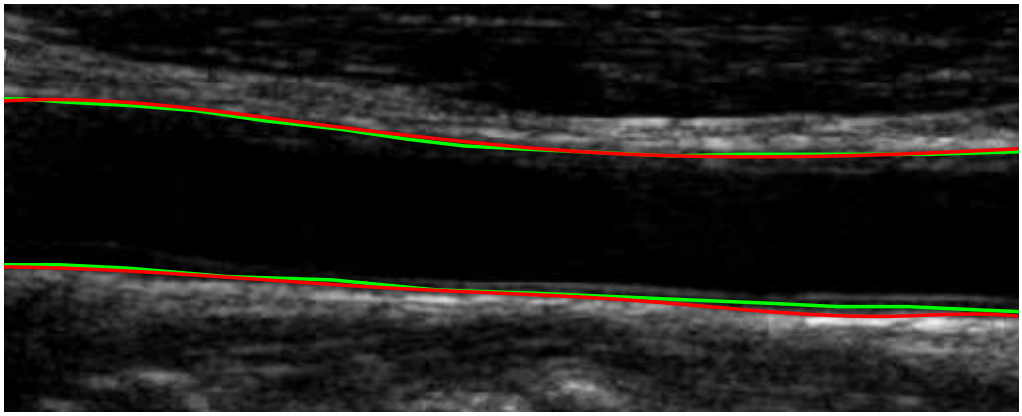

(b)

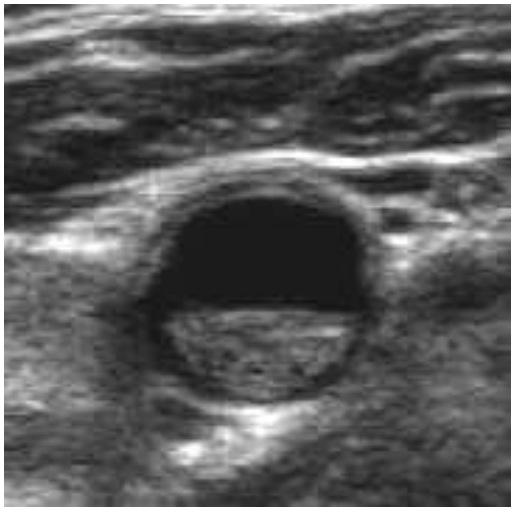

(c)

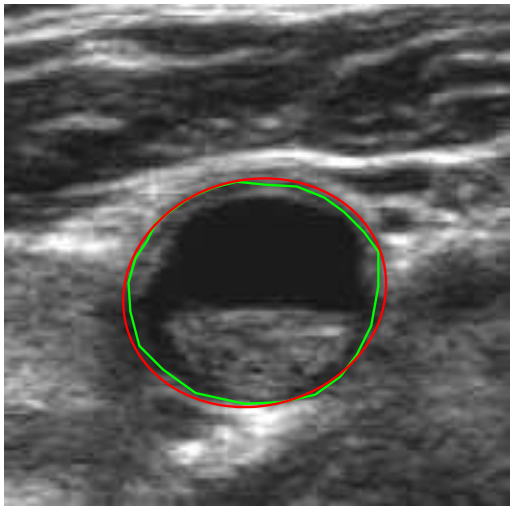

(d)

Fig. 4.16: Example of manual (green) and automatic (red) contours of the CCA walls: a) Longitudinal section; b) Contours for the longitudinal section; c) Transversal section; d) Contour for the transversal section.

of the wall boundaries. In appendices F and G, several other examples of successful and unsucessful segmentations are presented.

The following statistics were computed for the successful segmentations. Figure 4.18 (a) gives the boxes and whiskers for the maximum distance error, D_{err}, between the ground truth and the contour segmented automatically. This measure shows the maximum deviation from the ground truth. It is reliable in the present case, since the proposed segmentation model is robust to isolated outliers. In longitudinal sections, D_{err} is computed twice, one measure for the upper boundary and another for the lower one. In this case, the distance between the detected curve and the ground truth curve is simply the vertical distance between these two curves at each abscissa. In transversal sections, both the detected curve and the ground truth are densely sampled. Then, for each point of the detected curve, the distance to the ground truth is set as the smallest distance to the points of the ground truth.

Figure 4.18 (b) shows similar statistics for the relative area error, A_{err}, defined by the following expression

$$A_{\text{err}} = 1 - \frac{A \cap A_{\text{ref}}}{A \cup A_{\text{ref}}} \tag{4.19}$$

where A is the area inside the automatically segmented contour and A_{ref} is the area of reference (the ground truth). This measure was used as a complement of D_{err}, to evaluate the global quality of each segmentation. In longitudinal sections, A_{err} is computed only when both longitudinal contours were correctly detected, which happened in 37 of the 50 longitudinal images in the sample. As expected, the error is larger in transversal sections, where the wall boundaries are more likely to be missing in the image. This increases the uncertainty in the location of the real boundary, making it difficult to evaluate the real error. In general, a segmentation of a transversal section can be considered acceptable if the ellipse fits the visible contours reasonably well and gives an overall acceptable location of the boundary.

Although Matlab is not the best platform for efficiency, the CPU statistics presented in Fig. 4.19 give an idea of the relative computational weight of the main tasks in the wall segmentation. The simulations were done with a PC equipped with an Intel Core 2 Duo processor at 2.13 GHz and a 2GB RAM. The RANSAC algorithm usually takes longer to segment transversal sections. This should not come as a surprise, considering the lower quality of the wall boundaries and of the ellipse fitting, when compared to the boundaries in longitudinal sections and the spline fitting.

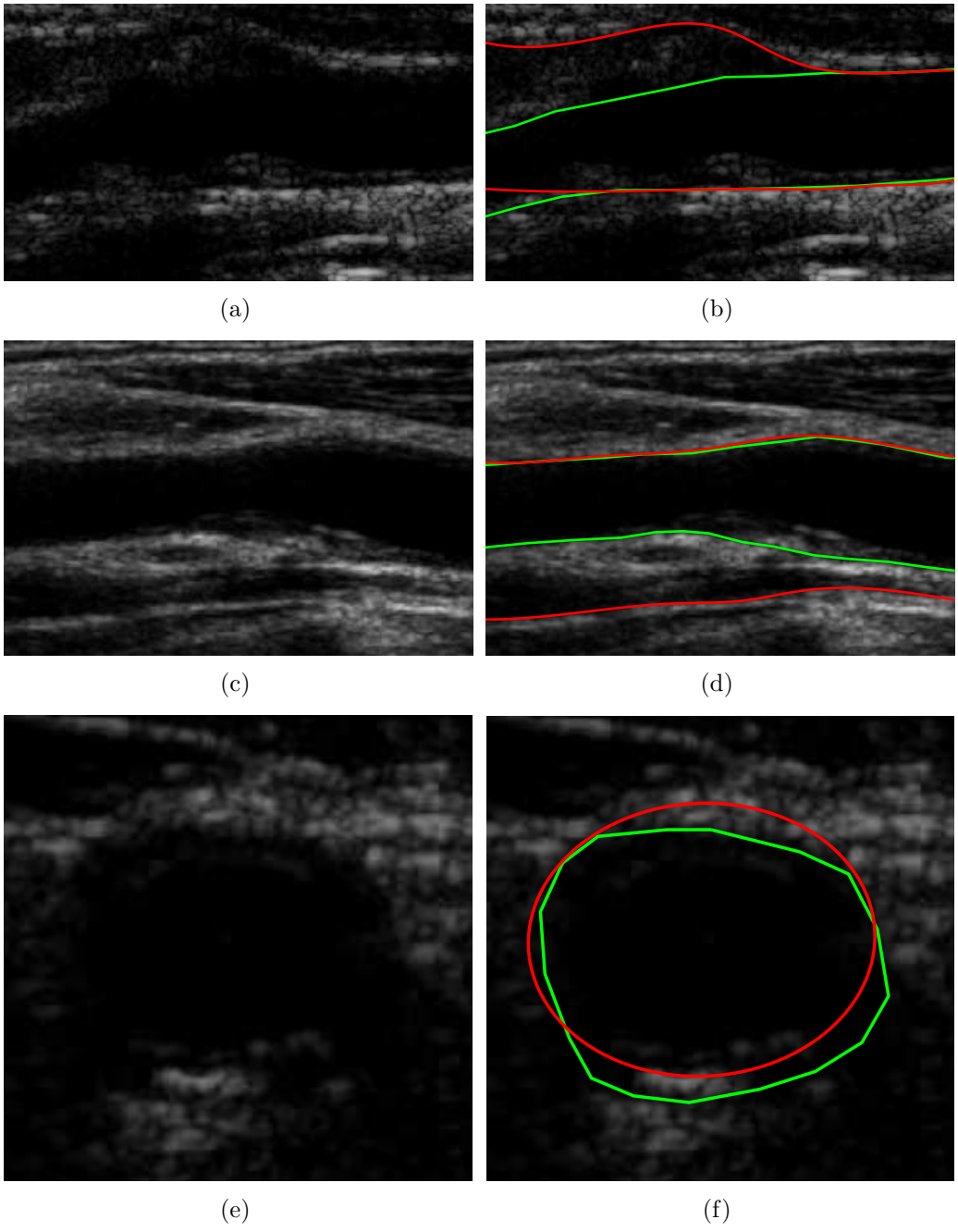

Fig. 4.17: Examples of failure in the segmentation of the carotid wall: a) Longitudinal section; b) Detected (red) and manually traced (green) wall contours for (a); c) Longitudinal section; d) Detected (red) and manually traced (green) wall contours for (c) e) Transversal section; f) Detected (red) and manually traced (green) wall contour for (e).

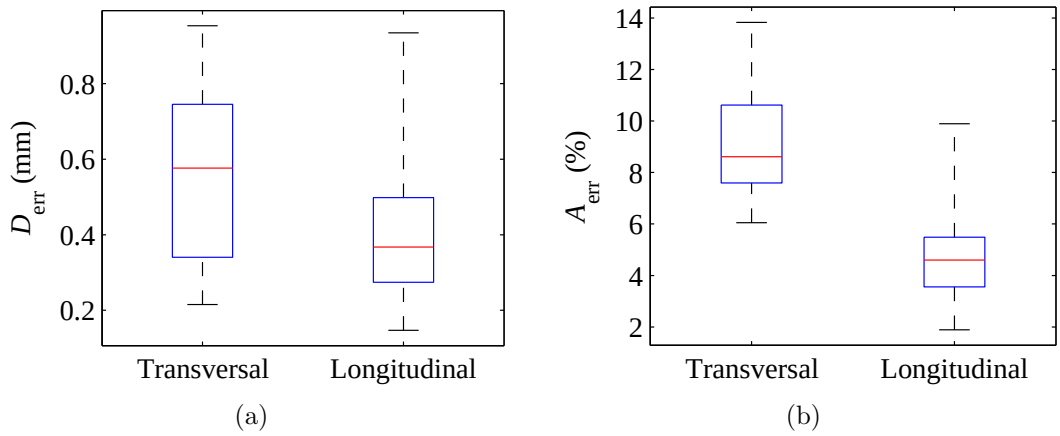

Fig. 4.18: Error statistics for the wall segmentation: a) D_{err} b) A_{err}.

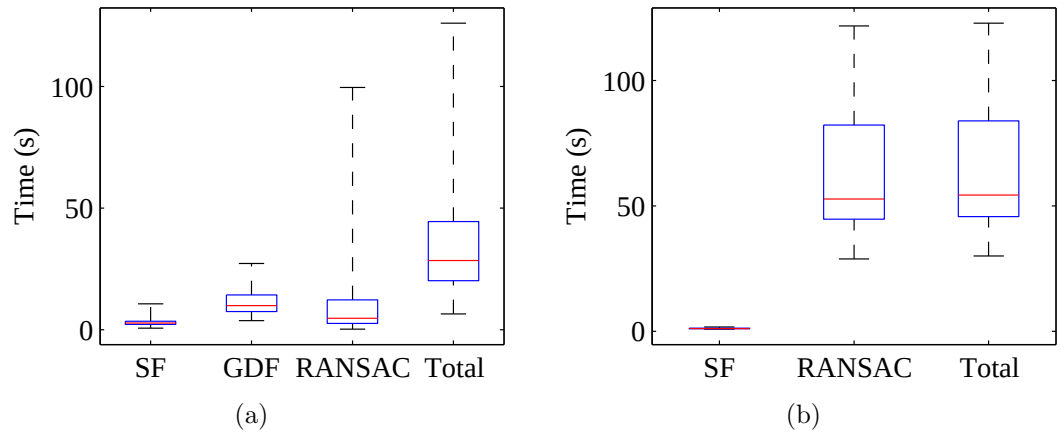

Fig. 4.19: CPU statistics for the wall segmentation for the non-linear image smoothing filter (SF), the dominant gradient direction filter (GDF), the RANSAC algorithm and the total time: a) Longitudinal sections; b) Transversal sections.

4.10 Concluding remarks

We have introduced a new algorithm for the segmentation of the carotid wall in both longitudinal and transversal B-mode sections of the CCA. This algorithm looks for the best smooth global path in the image, according to a newly proposed gain function, which integrates the response to several discriminating characteristics of the carotid wall in B-mode images. Our implementation of the RANSAC algorithm makes the search of the best path more efficient.

The complete cubic spline and the ellipse proved to be good geometric model priors for longitudinal and transversal sections, respectively. The 2D spline fitting seems to be a better geometric model than the ellipse for the wall boundary in transversal sections, but its computational complexity is too high.

Several presented examples and quantitative evaluations showed that our segmentation algorithm is robust to the highly degrading factors typical of these images, like the heavy noise, missing data and occlusions of the lumen region by plaque, producing good estimates of the wall boundaries, comparable to the contours manually traced by a specialist.

The results proved the high degree of discrimination of the selected characteristics for the wall boundary. But some additional information is needed to improve the robustness of the algorithm to other neighboring anatomical boundaries. This missing information is probably of contextual or anatomical nature.

Chapter 5

SEGMENTATION OF THE CAROTID LUMEN IN B-MODE IMAGES

5.1 Introduction

There are several properties of the B-mode images of the carotid that make the automatic detection of the lumen very difficult, in particular: a) gaps in the carotid boundaries due to echo dropouts are very common; b) there is usually a large echo and contrast variability over the image domain; c) the noise inside the lumen may be as strong as the echo produced by some parts of the tissues inside the carotid wall; d) some plaques are hypoechogenic, appearing as very dark regions, making its detection extremely difficult, even for a human observer.

Unfortunately, unlike the carotid wall, the lumen region cannot be represented by a geometric prior due to the possible presence of plaque. Therefore, the shape-based active contours are of no use here. We will keep to the simple active contour, without any shape restriction, which is still very powerful and useful in the lumen segmentation.

A new algorithm for an effective and automatic segmentation of the carotid lumen in B-mode images is proposed. It combines the speed of thresholding algorithms with the accuracy, flexibility and robustness of a successful geometric active contour model.

The chapter begins with a small overview of the proposed algorithm. Several thresholding algorithms are presented and tested in the segmentation of the lumen in B-mode images. Then, the proposed algorithm is described in detail. The chapter ends with a section of results, computed from an image data base, and a section of concluding remarks.

5.2 Overview of the approach

The proposed algorithm consists of three main steps. First, an estimate of the lumen boundary contour is computed with a dynamic programming algorithm. This estimated contour is usually a good approximation of the correct location of the lumen boundary and is very fast to compute. Nevertheless, it is often rugged and cannot capture all details of the lumen boundary when it has deep concavities or sharp saliences. Therefore, an additional processing is needed to improve these issues. This is done by a region-based geometric active contour.

The chosen active contour groups the image pixels according to their echo intensity. Therefore, it requires the knowledge of an intensity threshold at each pixel of the image. So, the estimation of this threshold is the second step of our algorithm. A single intensity threshold usually produces poor results when the illumination of an image is not constant. To cope with the intensity variability throughout the image domain, a smooth thresholding surface is computed. It is derived from the intensity values at the edge pixels that belong to the contour obtained with the dynamic programing algorithm.

Finally, a two-phase piecewise constant geometric active contour [97, 98] is initialized at the location estimated by the dynamic programming algorithm. Then, it evolves in the image plane according to the intensity topology and the thresholding surface. The active contour reduces the noise, produces smoother estimates of the lumen boundary and improves its position accuracy.

To avoid leakage through large gaps in the carotid boundary, the evolution of the active contour is restrained to the region inside the previously segmented wall contour.

5.3 Thresholding

Thresholding is one of the most popular segmentation approaches for images in which the objects of interest have different intensity from the background. It has the advantages of being very fast and frequently producing quite good segmentation results. Therefore, we thought it would be interesting to evaluate its performance in the segmentation of the carotid lumen in B-mode images.

The number of published thresholding algorithms is so large that it would be an enormous effort to evaluate them all. A very comprehensive and recent survey can be found in [99]. In this work, the authors used several figures of merit to evaluate

the performance of each thresholding algorithm and ranked them according to their overall average quality score. Two ranking tables were presented, one for document images and another for non-document images. We selected several algorithms between the best 10 in the rank presented for non-document images, in particular: Kittler's algorithm [100] (1^{st} in the rank); Kapur's algorithm [101] (2^{nd} in the rank); Sahoo's algorithm [102] (3^{rd} in the rank); Yen's algorithm [103] (4^{th} in the rank); Otsu's algorithm [104] (6^{th} in the rank); Yanowitz's algorithm [105] (8^{th} in the rank); Li's algorithm [106] (10^{th} in the rank).

Some of the listed algorithms were chosen not only for their good ranking position but also due to some particular properties that make them attractive for our application. The Otsu's algorithm was included for being a very popular model, usually used as a reference to compare other algorithms. Yanowitz's algorithm was the local thresholding algorithm with the highest score. In fact, it was the only one of its group to appear in the first 20 places. It was chosen because its local approach makes it more effective for images with poor and nonuniform illumination. Finally, Li's algorithm is known to produce better segmentations than most other single global thresholding algorithms, when some assumptions about the populations' distributions, size and variance are not valid [106].

To this list of selected thresholding algorithms, we added the triangle algorithm [86, 107], which is known to work well when the image histogram has a single large peak and a long tail, as is typical of B-mode images of the carotid. Two new algorithms were conceived and tested, in particular, the sequential and the local minimum cross entropy algorithms.

With the exception of the Otsu's algorithm, which is available in Matlab's image processing toolbox, all these thresholding algorithms were implemented in Matlab.

The rest of this section gives a brief description of each of the selected algorithms, as well as examples of their application to B-mode images of the carotid. At the end of the chapter, some statistics will be presented for their performance in these images.

Now we introduce some notation and important definitions. Let N be the number of image pixels, $G = \{0, 1, 2, \ldots, L-1\}$ the set of intensity levels in the gray scale image, $k \in G$ an intensity level, and $h(k)$ the image histogram. The probability, $p(k)$, of intensity k in the image, the total intensity mean, μ, and the total intensity variance, σ^2, are given by:

$$p(k) = \frac{h(k)}{N} \tag{5.1}$$

$$\mu = \sum_{k=0}^{L-1} kp(k) \tag{5.2}$$

$$\sigma^2 = \sum_{k=0}^{L-1} (k-\mu)^2 p(k) \tag{5.3}$$

Let T be the intensity threshold that segments the image into two classes, $C_1 = \{(x,y) : 0 \leq k \leq T\}$ and $C_2 = \{(x,y) : T < k < L\}$. A useful quantity is

$$\mu(T) = \sum_{k=0}^{T} kp(k) \tag{5.4}$$

Finally, the probability of class one, $P_1(T)$, the probability of class two, $P_2(T)$, the intensity mean of each class, $\mu_1(T)$ and $\mu_2(T)$, and their intensity variances, $\sigma_1^2(T)$ and $\sigma_2^2(T)$, are given by

$$P_1(T) = \sum_{k=0}^{T} p(k), \quad P_2(T) = \sum_{k=T+1}^{L-1} p(k) = 1 - P_1(T) \tag{5.5}$$

$$\mu_1(T) = \frac{\sum_{k=0}^{T} kp(k)}{P_1(T)}, \quad \mu_2(T) = \frac{\sum_{k=T+1}^{L-1} kp(k)}{P_2(T)} = \frac{\mu - \mu(T)}{1 - P_1(T)} \tag{5.6}$$

$$\sigma_1^2(T) = \frac{\sum_{k=0}^{T} [k-\mu_1(T)]^2 p(k)}{P_1(T)}, \quad \sigma_2^2(T) = \frac{\sum_{k=T+1}^{L-1} [k-\mu_2(T)]^2 p(k)}{P_2(T)} \tag{5.7}$$

5.3.1 Otsu's method

Otsu's algorithm [104] assumes a bimodal histogram and similar populations and variances for both classes. It looks for the intensity threshold, T, that maximizes the separability of the two classes, measured by one of the following equivalent criteria: $\lambda = \sigma_B^2/\sigma_W^2$ or $\eta = \sigma_B^2/\sigma^2$ or $\kappa = \sigma^2/\sigma_W^2$, where σ^2 is the total variance of the image, $\sigma_B^2 = P_1(T)P_2(T)\left[\mu_1(T) - \mu_2(T)\right]^2$ is the variance between classes and $\sigma_W^2 = P_1(T)\sigma_1^2(T) + P_2(T)\sigma_2^2(T)$ is the variance within classes. The optimum threshold, T_{opt}, can be computed in a very efficient way as

$$\begin{aligned} T_{\text{opt}} &= arg \max_{T \in G} \eta(T) \\ &= arg \max_{T \in G} \left\{ \frac{[\mu P_1(T) - \mu(T)]^2}{\sigma^2 P_1(T)[1 - P1(T)]} \right\} \end{aligned} \tag{5.8}$$

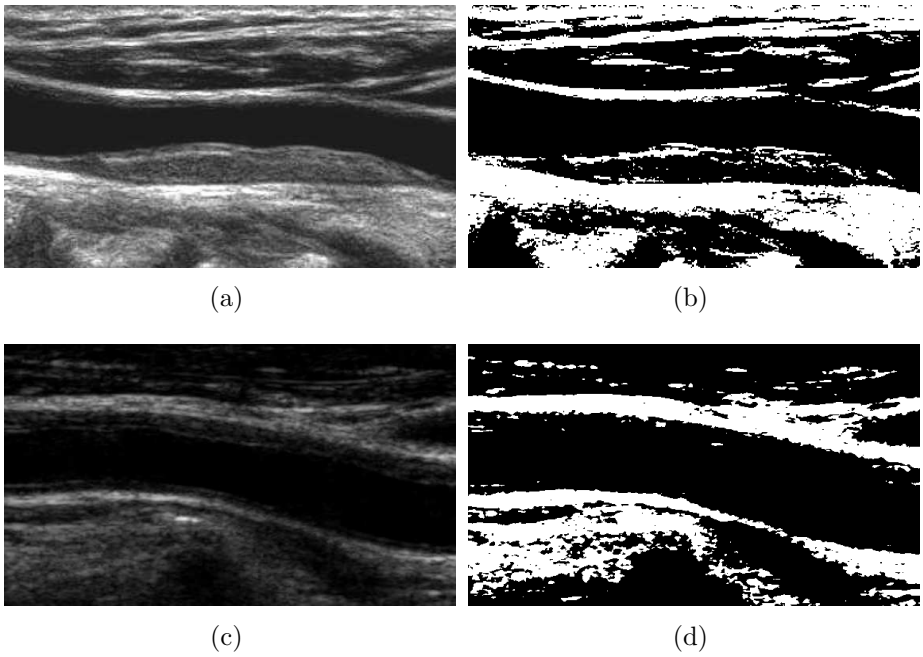

Fig. 5.1: Examples of Otsu's thresholding: a) B-mode image of the carotid with insignificant speckle noise in the lumen; b) Binary image produced by the Otsu's threshold for image (a); c) B-mode image of the carotid with some speckle noise in the lumen; b) Binary image produced by the Otsu's threshold for image (c)

Two segmentation examples are presented in Fig. 5.1, one for an image with some speckle noise inside the lumen and another for an image with insignificant speckle noise in the lumen.

5.3.2 Kittler's method

Kittler's algorithm [100] assumes the image histogram is a mixture of two Gaussian distributions, one for foreground pixels and the other for background pixels. It also assumes that the overlap between the two underlying distributions is small. This overlap tends to introduce a bias in the estimated threshold and, if it is too large, it may lead to a complete failure of the algorithm. The optimum threshold is the one that minimizes the total misclassification error and can be obtained as

$$T_{\text{opt}} = arg \min_{T \in G} \left\{ 1 + 2\left[P_1(T) ln\, \sigma_1(T) + P_2(T) ln\, \sigma_2(T)\right] - 2\left[P_1(T) ln\, P_1(T) + P_2(T) ln\, P_2(T)\right] \right\} \tag{5.9}$$

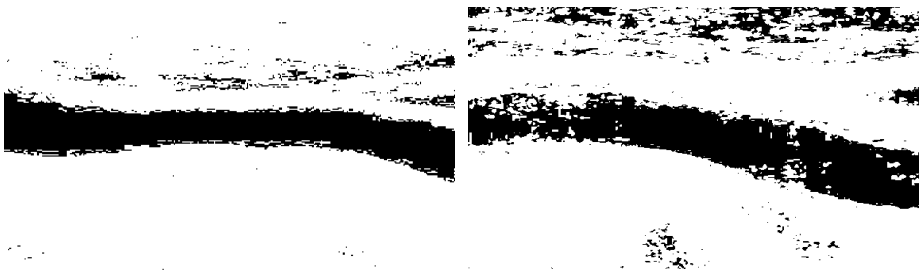

(a) (b)

Fig. 5.2: Binary images produced by the Kittler's algorithm: a) For the image in Fig. 5.1 (a); b) For the image in Fig. 5.1 (c).

or, in a simpler and equivalent way, as

$$T_{\text{opt}} = arg \min_{T \in G} \left\{ \begin{array}{l} P_1(T) ln\, \sigma_1(T) + P_2(T) ln\, \sigma_2(T) \\ - P_1(T) ln\, P_1(T) - P_2(T) ln\, P_2(T) \end{array} \right\} \tag{5.10}$$

Two segmentation examples are presented in Fig. 5.2.

5.3.3 Kapur's method

Kapur's algorithm [101] maximizes the information measure between classes C_1 and C_2, viewed as two different signal sources. It is also known as the maximum entropy sum method because the optimum threshold is the one that maximizes the sum of the Shanon entropies for the two classes. These class entropies are defined as

$$\begin{aligned} H_1(T) &= -\sum_{k=0}^{T} \frac{p(k)}{P_1(T)} ln\, \frac{p(k)}{P_1(T)} \\ H_2(T) &= -\sum_{k=T+1}^{L-1} \frac{p(k)}{P_2(T)} ln\, \frac{p(k)}{P_2(T)} \end{aligned} \tag{5.11}$$

and the optimum threshold is given by

$$\begin{aligned} T_{\text{opt}} &= arg \max_{T \in G} \{H_1(T) + H_2(T)\} \\ &= arg \max_{T \in G} \left\{ ln\, [P_1(T) P_2(T)] + \frac{H(T)}{P_1(T)} + \frac{H_T - H(T)}{P_2(T)} \right\} \end{aligned} \tag{5.12}$$

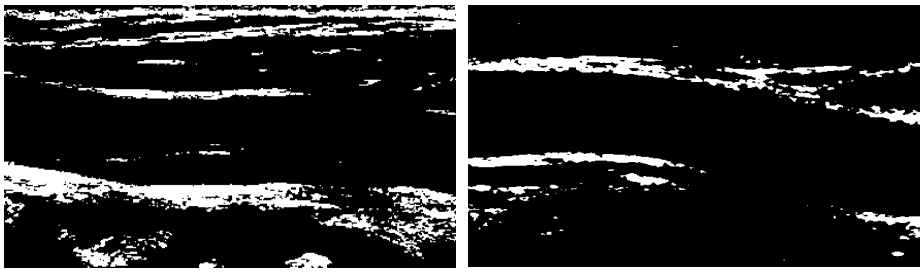

(a) (b)

Fig. 5.3: Binary images produced by the Kapur's algorithm: a) For the image in Fig. 5.1 (a); b) For the image in Fig. 5.1 (c).

where

$$H(T) = -\sum_{k=0}^{T} p(k) ln\, p(k) \tag{5.13}$$

and H_T is the entropy for the entire image, given by

$$H_T = -\sum_{k=0}^{L-1} p(k) ln\, p(k) \tag{5.14}$$

Two segmentation examples are presented in Fig. 5.3.

5.3.4 Sahoo's method

This method, introduced in [102], uses the Renyi's entropy, defined as

$$H_R^{\alpha} = \frac{1}{1-\alpha} ln \sum_{i=1}^{M} p_i^{\alpha} \tag{5.15}$$

where $\alpha\,(\neq 1)$ is a positive real number. This entropy is a one parameter generalization of the Shannon entropy, $H_S = -\sum_{i=1}^{M} p_i ln\, p_i$, since $\lim_{\alpha \to 1} H_R^{\alpha} = H_S$ [102]. The particular case of $\alpha = 1$ corresponds to the Kapur's algorithm. The optimum threshold is a weighted average of three different thresholds, each of which maximizes the sum of the Renyi's entropy of the two classes for a particular value of α. The first value of α is in $0 < \alpha < 1$, the second is $\alpha = 1$ and the third comes from

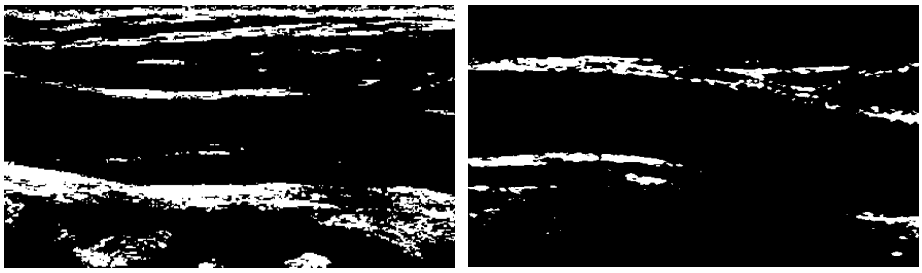

(a) (b)

Fig. 5.4: Binary images produced by the Sahoo's algorithm: a) For the image in Fig. 5.1 (a); b) For the image in Fig. 5.1 (c).

range $\alpha > 1$. The Renyi's entropies for classes C_1 and C_2 are defined as

$$\begin{aligned} H_1^\alpha(T) &= \frac{1}{1-\alpha} ln \sum_{k=0}^{T} \left(\frac{p(k)}{P_1(T)} \right)^\alpha \\ H_2^\alpha(T) &= \frac{1}{1-\alpha} ln \sum_{k=T+1}^{L-1} \left(\frac{p(k)}{P_2(T)} \right)^\alpha \end{aligned} \tag{5.16}$$

and the optimum threshold for a given value of parameter α is given by

$$T_{\text{opt}}(\alpha) = arg \max_{T \in G} \{H_1^\alpha(T) + H_2^\alpha(T)\} \tag{5.17}$$

Two segmentation examples are presented in Fig. 5.4, where the three thresholds used in the final average (with the weights proposed in [102]) were computed for $\alpha = 0.5$, $\alpha = 1$ and $\alpha = 2$.

5.3.5 Yen's method

Yen's method [103] maximizes the sum of the Renyi's entropies of the two classes, using equation 5.17 with $\alpha = 2$. Two segmentation examples are presented in Fig. 5.5.

5.3.6 Triangle method

As illustrated in Fig. 5.6, the triangle algorithm [86] starts by determining the line passing through points $(k_a, h(k_a))$ and $(k_b, h(k_b))$, the peak of the histogram and the end of the histogram tail, respectively. The distance, d, from this line to the

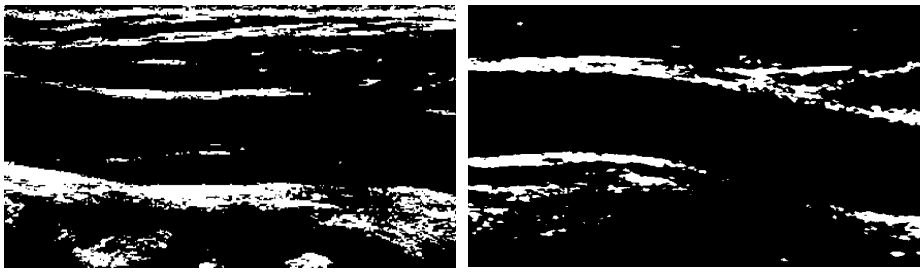

(a) (b)

Fig. 5.5: Binary images produced by the Yen's algorithm: a) For the image in Fig. 5.1 (a); b) For the image in Fig. 5.1 (c).

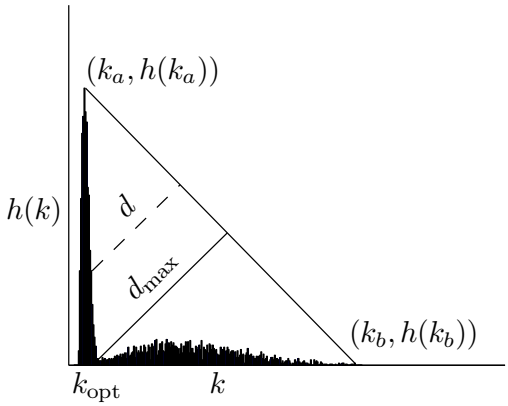

Fig. 5.6: The triangle algorithm selects the intensity threshold (k_{opt}) that maximizes the distance d.

histogram is computed for each intensity, between k_a and k_b. The optimum threshold is selected as the intensity that maximizes the value of d. Two segmentation examples are presented in Fig. 5.7.

5.3.7 Minimum cross entropy method

The minimum cross entropy (MCE) algorithm [106] minimizes the cross entropy between the gray scale image and its binary version obtained with a threshold, T. The cross entropy, also known as Kullback's distance, measures the information theoretic distance between two given distributions, $P = \{p_1, p_2, \ldots, p_M\}$ and $Q = \{q_1, q_2, \ldots, q_M\}$, and is expressed as

$$D(Q, P) = \sum_{i=1}^{M} q_i ln(\frac{q_i}{p_i}) \tag{5.18}$$

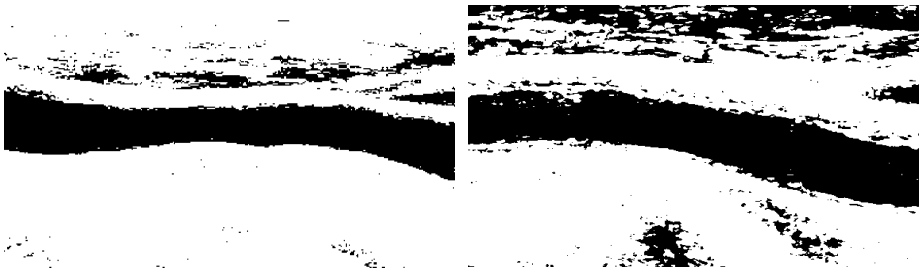

(a) (b)

Fig. 5.7: Binary images produced by the triangle algorithm: a) For the image in Fig. 5.1 (a); b) For the image in Fig. 5.1 (c).

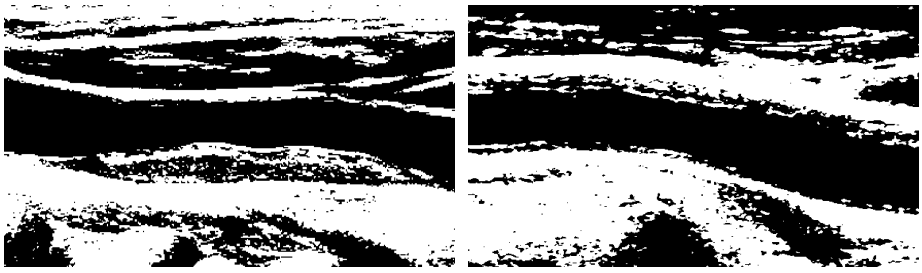

(a) (b)

Fig. 5.8: Binary images produced by the MCE algorithm: a) For the image in Fig. 5.1 (a); b) For the image in Fig. 5.1 (c).

This distance is minimized under the constraint that both the segmented and the binary image have identical intensity means in their foreground and background, which leads to the following equation

$$T_{\text{opt}} = arg \min_{T \in G} \left\{ \sum_{k=0}^{T} kh(k) ln \left(\frac{k}{\mu_1(T)} \right) + \sum_{k=T+1}^{L-1} kh(k) ln \left(\frac{k}{\mu_2(T)} \right) \right\} \qquad (5.19)$$

where we assume that $0\, ln(0) = 0$.

Two segmentation examples are presented in Fig. 5.8.

Unlike other algorithms that make assumptions about the distribution and variances of the two classes present in the image, the MCE criterion gives threshold estimates without the tendency of biasing when these assumptions are not true. This is probably the reason why it performs better, in our images, than most of the other tested thresholding algorithms (see the statistics in section 5.6). In the group of single global thresholding, the MCE algorithm was only surpassed by the triangle

algorithm. This is the reason behind its choice in two other thresholding algorithms proposed next, in particular, the sequential minimum cross entropy algorithm and the local minimum cross entropy algorithm.

5.3.8 Sequential minimum cross entropy method

Due to the echo variability in B-mode images, their segmentation may be viewed as a multiphase problem in which the lumen is a part of the darkest phase in the image. This assumption is made in [13] to present a new thresholding algorithm, called sequential minimum cross entropy (SMCE).

The idea behind the SMCE thresholding is to use the MCE algorithm iteratively. In the first iteration, the MCE algorithm is used to divide the original image into two regions. In the second iteration, the darkest region produced by the first iteration is further subdivided into another pair of regions, and so on, until a certain stopping criterion is satisfied. At the end of each iteration, only two regions of interest remain: the region with intensities below the last threshold and the region with all other intensities.

If the lumen has low noise, it appear as a very dark and homogeneous region, for which the intensity standard-deviation, σ, is quite small. This information can be used in a stopping criterion. Iterations come to an end when the value of σ, for the darkest region in the last iteration, drops bellow a certain threshold. Segmentation examples with this iterative algorithm, using $\sigma < 0.01$ as stopping criterion, are presented in Fig. 5.9. This works well if there is no significant noise inside the lumen. Otherwise, it will usually stop too late, as in the example presented in Fig. 5.9 (b), where some of the lumen noise is classified as other tissue. A possible solution would be to automatically adapt the σ threshold to each image, according to the level of noise expected in the lumen region. But no reliable criterion was found to do this.

5.3.9 Local minimum cross entropy method

An alternative to the SMCE algorithm is a local MCE (LMCE), which uses a single MCE threshold computed only for the region inside the carotid. The carotid boundary is included in the support region to make sure we always keep some other tissue besides the blood in the lumen. The local support of the thresholding gives a better estimate of the lumen region than most of the other tested thresholding algorithms. Figure 5.10 shows the binary images obtained with the LMCE algorithm for the gray

(a) (b)

Fig. 5.9: Binary images produced by the SMCE algorithm: a) For the image in Fig. 5.1 (a); b) For the image in Fig. 5.1 (c).

(a) (b)

Fig. 5.10: Binary images produced by the LMCE algorithm: a) For the image in Fig. 5.1 (a); b) For the image in Fig. 5.1 (c).

scale images presented in Fig. 5.1. One limitation of this approach is that it can only be applied after the segmentation of the carotid wall contours, since it needs this information to compute the boundaries of the support region.

5.3.10 Yanowitz's method

In spite of the apparent acceptable performance of some of the above methods (in particular, the triangle and the LMCE algorithm), all the considered single threshold methods give very poor results when the intensity variability becomes large. As can be seen in the example of Fig. 5.11, large extensions of the plaque region are misclassified as a part of the lumen, by both the triangle and the LMCE algorithms, due to the nonuniform and very weak echo produced by the plaque. On the other hand, some noise inside the lumen appears as white regions in the binary image. Obviously, this problem requires local thresholding.

The approach followed by Yanowitz and Bruckstein [105] is quite different from

(a) (b) (c)

Fig. 5.11: Thresholding an image with a dark plaque and nonuniform illumination: a) Ultrasound image with nonuniform illumination and a dark plaque; b) Segmentation obtained with the triangle thresholding algorithm; c) Segmentation obtained with the LMCE thresholding algorithm.

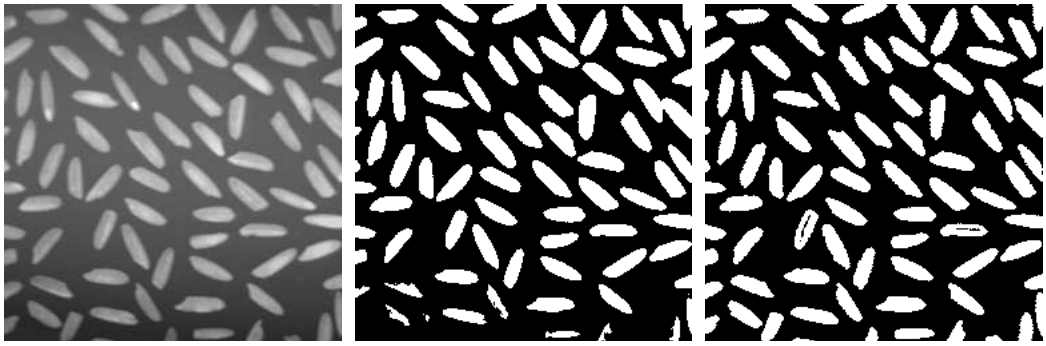

(a) (b) (c)

Fig. 5.12: Thresholding with nonuniform illumination: a) Image with nonuniform illumination; b) Segmentation obtained with the Otsu's thresholding algorithm; c) Segmentation obtained with the Yanowitz' thresholding algorithm.

the methods described so far. Instead of a single intensity threshold for the entire image, a local threshold is computed for each image pixel, in the form of a smooth thresholding surface. This is a generalization of the single global thresholding approach, which is equivalent to using a thresholding surface with a constant height. Local thresholding methods may produce better segmentations when the image presents nonuniform illumination. As an example, Fig. 5.12 shows an image with nonuniform illumination, as well as the binary image produced by the Otsu's algorithm, where we can see that the objects at the darker part of the image are not well detected. Figure 5.12 (c) shows the segmentation improvement introduced by Yanowitz' algorithm.

In [105], the thresholding surface is determined by interpolating the image intensities at edge pixels, where we expect to find intensity values that are good local

thresholds. The algorithm may be summarized in the following steps:

1. A low-pass filter is applied to the image to obtain a smoothed version, with reduced noise and moderate slopes at edges. This improves the estimates of the local thresholds.

2. An edge map is computed from the smoothed image as the local maxima of the gradient magnitude in the gradient direction, above a certain threshold.

3. The edge pixels found at the image boundaries are used to estimate, by linear interpolation, the intensity thresholds along the whole image border. This step is required for a good segmentation of objects that are cut by the image frame.

4. The intensities at the edge pixels and the intensity thresholds estimated at the image boundaries are interpolated over the rest of the image, by solving the Laplace's equation
$$\frac{\partial^2 u}{\partial x^2} + \frac{\partial^2 u}{\partial y^2} = 0 \tag{5.20}$$
for the thresholding surface, u.

5. The solution of this equation will be our smooth thresholding surface, which can then be used to segment the image.

6. If the thresholding surface intersects the image intensity surface inside the objects or the background, 'ghost' objects will appear in the binary image. These stains may be removed by a validation process, where white or black regions are eliminated if they have a weak edge support along their boundary.

The surfaces that satisfy equation 5.20 are known as potential surfaces and their smoothness comes from the fact that the divergence of their gradient vanishes everywhere [105].

Our implementation of this algorithm has some differences relative to the one proposed in [105], as discussed next.

We implemented two versions of the algorithm. The first one uses the Canny's edge detector [67], where a Gaussian filter is used to smooth the image and the gradient magnitude is used to measure the edge strength. This should be more appropriate for images with additive noise. The second version uses the non-linear smoothing filter proposed in section 4.5 and the ICOV-based edge detector described in section 4.6. This version is better suited for ultrasound images, where the noise

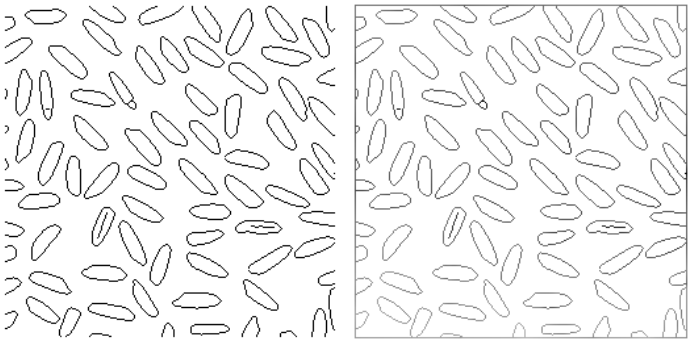

(a) (b)

Fig. 5.13: Interpolating data in Yanowitz' algorithm: a) Edge map for the image in Fig. 5.12 (a); b) Intensities at the interpolating pixels for the same image, where a higher image intensity is represented by a darker pixel.

has a multiplicative nature. Non-maxima suppression and hysteresis are used in both versions. In practice, the smoothed image (step 1) and the corresponding edge map (step 2) are previously computed, using independent functions that are also useful to other applications, and then passed to the next steps of the Yanowitz' algorithm.

The second difference is in the intensity (linear) interpolation along the image border. In [105], only the edge points detected at the image boundaries are used in this interpolation. To improve its reliability, we extended the search for edge points to the 8-neighborhood of image boundary pixels. In Fig. 5.13 we can see the edge map of the image in Fig. 5.12 and the intensities at all interpolating pixels, that is, the pixels at the detected edges and the images borders.

Another important difference is the resolution of the Laplace's equation. Its solution is computed in two steps. First, an approximate solution is obtained with a very fast algorithm that propagates the intensity values at the interpolating pixels to the rest of the image pixels. Second, the Laplace's equation is solved with the following numerical scheme

$$\begin{aligned} u_{i,j}^{n+1} &= 0.25\left(u_{i+1,j}^{n} + u_{i-1,j}^{n} + u_{i,j+1}^{n} + u_{i,j-1}^{n}\right) \\ u_{i,j}^{n+1} &= \lambda u_{i,j}^{n+1} + (1-\lambda)u_{i,j}^{n}, \quad n = 0, 1, 2, \ldots \end{aligned} \tag{5.21}$$

where $u_{i,j}^{n}$ is the value of the thresholding surface at pixel (i, j) and iteration n, $\lambda = 1.5$ and the initial solution, u^0, is the surface obtained in the first step.

The second equality of equation 5.21 introduces over-relaxation [94] to speed up

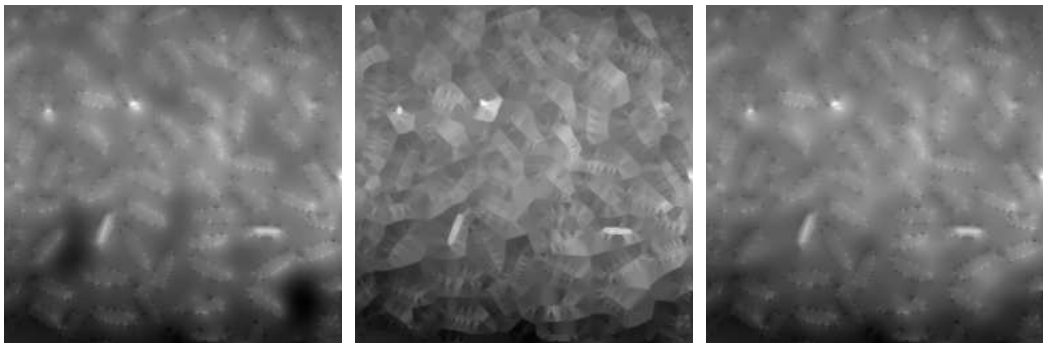

(a) (b) (c)

Fig. 5.14: Thresholding surfaces for the interpolating data in Fig. 5.13 (b), where the surface value at each pixel is represented by a gray scale level: a) Solution of the Laplace's equation if the initial values of the interpolated pixels are set to zero; b) Surface obtained by propagating the intensities at the interpolating pixels to the rest of the image; c) Solution of the Laplace's equation if the initial solution is the surface presented in (b).

the convergence. The iterations stop when the relative intensity difference between two consecutive iterations is less than 1% for all image pixels.

The intensity propagation step was implemented as described next. The Euclidean distance map to the interpolating pixels is computed with a very fast algorithm [88]. Then, the other pixels are ordered in a list by ascending value of the computed distance and processed in that order. At each pixel in the list, the intensity threshold is computed as a weighted average of the thresholds found for its 8-neighbors with smaller distance to the data points. The weights used in the average are inversely proportional to the distances of the central pixel to its 8-neighbors. As can be seen in Fig. 5.14 (b), this solution is not as smooth as desired, but its computation is extremely fast and will significantly reduce the total computational effort, when used to initialize the numerical scheme for the Laplace's equation. Moreover, initializing the interpolated pixels with zero will usually lead to solutions with deeper concavities, which are more likely to produce 'ghost' objects in the binary image obtained through thresholding. Figure 5.14 (a) and Fig. 5.14 (c) show the solutions obtained for the Laplace's equation when initializing the interpolated pixels with zeros and with the propagated intensities, respectively. The solution of Fig. 5.14 (a) has darker regions between the interpolating pixels, evidencing deeper concavities of the thresholding surface in those areas.

Finally, Fig. 5.15 presents two examples of the segmentation produced by this algorithm in B-mode images, without the validation step used to remove false objects.

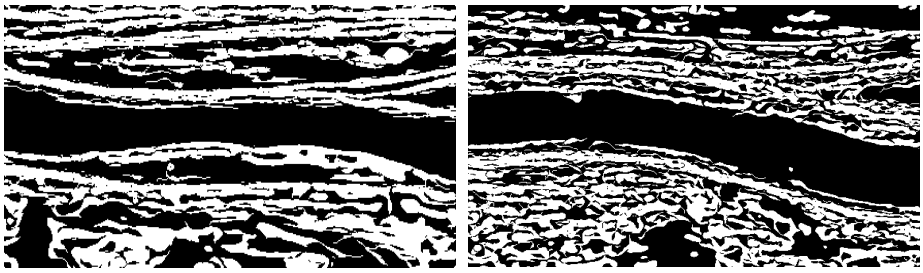

(a) (b)

Fig. 5.15: Binary images produced by the Yanowitz' algorithm: a) For the image in Fig. 5.1 (a); b) For the image in Fig. 5.1 (c).

As we can conclude from this example, the algorithm leaves numerous 'ghost' objects. Some of these stains are caused by staircase shaped intensity profiles, which may appear, for instance, when the plaque has an intensity mean above the one found for the lumen but bellow the intensity mean of the bright tissues surrounding the carotid. These false objects are difficult to eliminate because a large part of their boundaries corresponds to real object boundaries.

In some images, large areas of hypoechogenic plaques may not be distinguishable from the lumen, except for a thin and discontinuous line (see Fig. 5.11) along the boundary between the plaque and the lumen. In these cases, the Yanowitz' algorithm will not be able to detect the interior of the plaque region, leaving those areas as black holes. This limitation is common to the other thresholding algorithms previously discussed. The search for the most significant path is probably the best approach to deal with this type of problems.

5.4 Dynamic programming

Dynamic programming is a very efficient optimization method that can be used to search for the optimal path in an image, according to some cost function [6, 8]. It assumes the path we are looking for is a graph of the type $y = f(x)$, that can be represented as a polyline, $p = (p_1, p_2, \ldots, p_N)$, formed by a sequence of N points, as illustrated in Fig. 5.16.

Let's assume the desired path, in an image, begins at the first column and ends at the last column of a selected rectangular ROI. A scanning of this ROI is done from left to right, one column at a time. Each pixel is connected to one of its three left neighbors in the pixel matrix. The chosen neighbor is the one with the

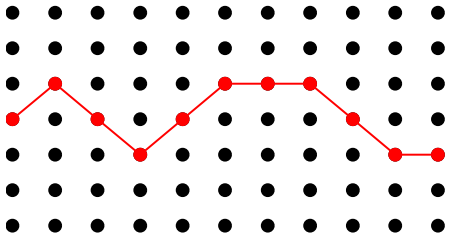

Fig. 5.16: A polyline, represented by the curve connecting the red points.

lowest accumulated value of the cost function, up to the previous column. After the connection is made, the accumulated value of the cost function at the current pixel is computed and stored. At the last column of the ROI, each pixel is the end point of a polyline. The other points of each polyline can be found by backtracking through the pointers to the best left neighbors, up to the first column of the matrix.

The optimal path is the one that minimizes the total cost function

$$C_t = \sum_{j=1}^{N} c(p_j) \tag{5.22}$$

where

$$c(p_j) = \sum_{k=1}^{m} w_k \psi_k(p_j) \tag{5.23}$$

is the local cost of the path at its point p_j, defined as a weighted sum of m local cost terms, $\psi_k(p_j)$, reflecting the influence of different image local features or geometrical properties. The weight factors, represented by w_k, determine the relative importance of each local cost term.

Representing by $C(p_n) = \sum_{j=1}^{n} c(p_j)$ the accumulated cost at point p_n, we can rewrite equation 5.22 in the following recursive form

$$\begin{cases} C(p_1) = c(p_1) \\ C(p_j) = C(p_{j-1}) + c(p_j), \quad j = 2, 3, \ldots, N \end{cases} \tag{5.24}$$

Therefore, at each pixel, $p_{i,j}$, the accumulated cost, $C(p_{i,j})$, and the pointer to the best left pixel can be stored in position (i, j) of two arrays with the same size of the ROI.

There are several image features that can be integrated into the cost function, depending on the application. In [6], a cost function was proposed to detect the

boundaries of the carotid in B-mode images. It consists of three terms, one related to an echo intensity feature, another related to an intensity gradient feature and, finally, a geometric constraint term. This model and its disadvantages were already discussed in section 3.1.

We introduce a new approach that gives satisfactory results and has the advantage of using the ICOV strength instead of the gradient magnitude.

The geometric term was implemented as a function of the length of the path, since this constraint is the most frequent in some very successful models for active contours [97, 98].

Although we could easily include, as well, an echo intensity term, we tried to avoid it to keep the model as simple as possible, with the advantage of requiring the estimation of less weights.

Our algorithm can be summarized in the following steps:

1. Compute the strong edge map, E_{strong}, as described in section 4.6, for the ROI selected during the segmentation of the carotid wall. Figure 5.17 shows an example of an image ROI for a longitudinal section and the corresponding strong edge map, where we can see that significant parts of the lumen boundary were not detected.

2. Using a similar procedure, compute the edge map with all edges, E_{all}, including the weak ones. An example is presented in Fig. 5.18 (a). This edge map is important because we have noticed that large parts of the lumen boundary may be far too weak to be captured in the strong edge map. In fact, some of the recovered lumen boundary edges are virtually imperceptible to a human observer.

3. Create a new edge map, E, containing only the edges of E_{all} that fall strictly inside the carotid wall. See Fig. 5.18 (b).

4. Clean all edges with incompatible gradient direction (Fig. 5.19). The lumen region is darker than the surrounding tissues. So, as in subsection 4.6.2, we should clean the edge maps from all edges with gradient pointing to the interior of the artery, i.e., with a large value of the angle γ. Since the lumen boundary can be much more irregular than the carotid wall, we are less demanding here, removing only the edges with $\gamma \geq 90^{\circ}$.

5. Normalize, over each vertical or radial line segment, the ICOV of the edges in E. Starting from the lumen axis, we walk along the line segment, searching

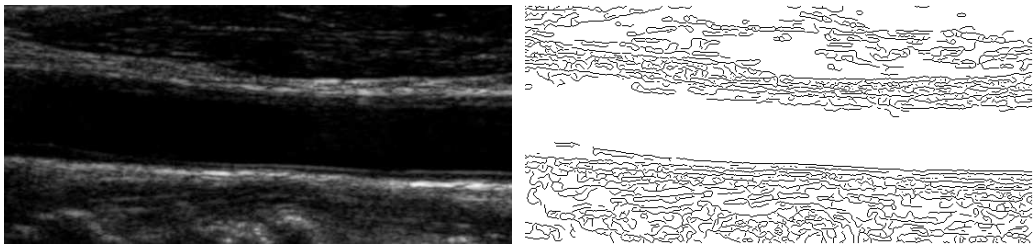

(a) (b)

Fig. 5.17: a) ROI from a B-mode image of a longitudinal section; b) Edge map, E_{strong}, containing only strong edges.

for edges in E. For each of the line segments, the ICOV of each edge is divided by the maximum value found for the edges in that segment. This procedure gives a chance to the usually weaker lumen boundary edges to compete with the wall edges. Otherwise, the polyline will usually be attracted toward the wall, where the ICOV is much stronger.

6. Add to edge map E the strong edges that are visible from the lumen axis (Fig. 5.20), normalizing their ICOV to one. These edges are the first ones found in the cleaned strong edge map, starting at the lumen axis and walking in the radial direction. This step is required because, when the intima-media region (the one that separates the lumen from the carotid wall) is not visible, the carotid wall is the best estimate of the lumen boundary.

7. Using dynamic programming, look for the path in E that minimizes the following cost function

$$C_t = \psi_1(p_1) + \sum_{j=2}^{N} [\psi_1(p_j) + \lambda \psi_2(p_{j-1}, p_j)] \tag{5.25}$$

where: $\psi_1(p_j) = 1 - \text{ICOV}^*$, if p_j is an edge pixel of E, and $\psi_1(p_j) = 1$, otherwise, where ICOV^* represents the normalized ICOV as described in the previous steps; $\psi_2(p_{j-1}, p_j) = 1/\sqrt{2}$, if p_{j-1} and p_j belong to the same line in matrix E, and $\psi_2(p_{j-1}, p_j) = 1$, otherwise; λ is the weight of the geometric term.

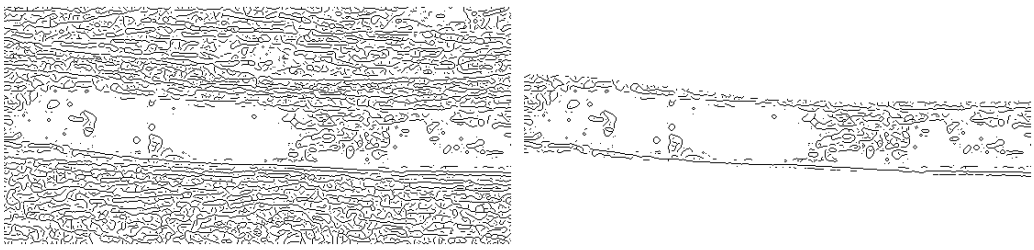

(a) (b)

Fig. 5.18: a) Complete edge map, E_{all}, containing all edges (strong and weak) found in the image presented in Fig. 5.17; b) Edge map, E, with the edges in E_{all} that fall strictly inside the carotid wall.

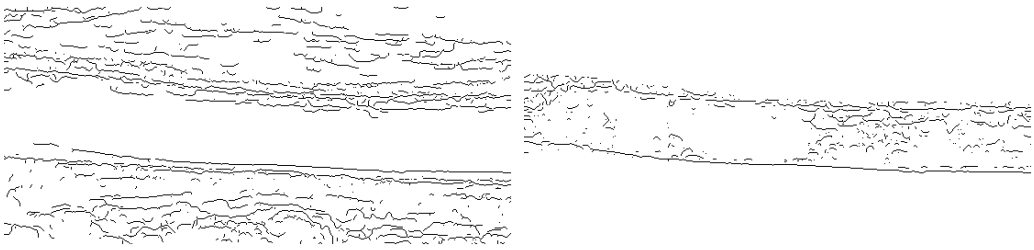

(a) (b)

Fig. 5.19: Edge maps after cleaning the edges with incompatible gradient direction: a) Cleaned version of the strong edge map, E_{strong}, presented in Fig. 5.17; b) Cleaned version of the edge map, E, presented in Fig. 5.18.

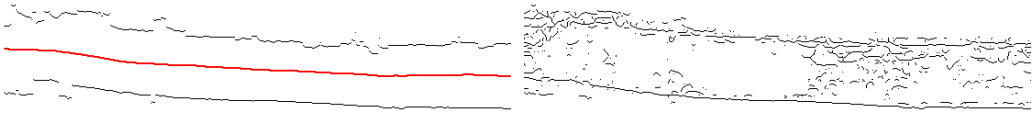

(a) (b)

Fig. 5.20: a) Edges of E_{strong} that are visible from the lumen axis (curve in red) specified by the user; b) Final version of edge map, E, after adding to it the edges presented in (a).

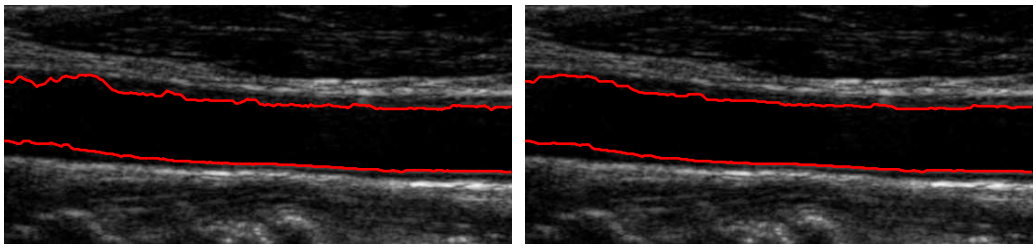

(a) (b)

Fig. 5.21: Lumen boundaries for the image in Fig. 5.17, segmented with dynamic programming: a) Without any geometric constraint ($\lambda = 0$); b) With a geometric constraint ($\lambda = 5$).

5.4.1 Dynamic programming for longitudinal sections

If the image corresponds to a longitudinal section of the carotid, we expect to find two contours, one above and the other below the lumen medial axis. Both contours start at the first column and finish at the last column of the edge map E. Therefore, the dynamic programming algorithm can be applied directly to E. However, the search must be done separately above and bellow the lumen medial axis. Figure 5.21 shows the lumen boundaries detected by our dynamic programming algorithm for the image presented in Fig. 5.17. The example shows the results obtained with ($\lambda = 5$) and without ($\lambda = 0$) a geometric constraint, to illustrate the smoothing introduced by the geometric term. Similar results for the image of Fig. 5.11 are presented in Fig. 5.22, to demonstrate the significant improvement relative to the segmentation with thresholding algorithms, for hypoechogenic plaques.

5.4.2 Dynamic programming for transversal sections

In a transversal section, we have a single closed contour. To be able to apply the described dynamic programming algorithm to this case, we select the smallest circular region, centered at the lumen centroid specified by the user (see section 4.3), that contains all the edges found in E. Then, we convert this ROI to polar coordinates, (r, θ), to obtain a rectangular grid with size $M \times N$. We set $M = ceil(R)$ and $N = ceil(2\pi R)$, where R is the largest distance from an edge to the centroid and $ceil(z)$ is the smallest integer above a real value z. The angle $\theta \in [0, 2\pi]$ is divided into $N - 1$ intervals of equal amplitude, such that the first and last columns of this polar matrix correspond to $\theta = 0$ and $\theta = 2\pi$, respectively. The lines of this matrix correspond to consecutive integer values of the radius, r, between 1 and M.

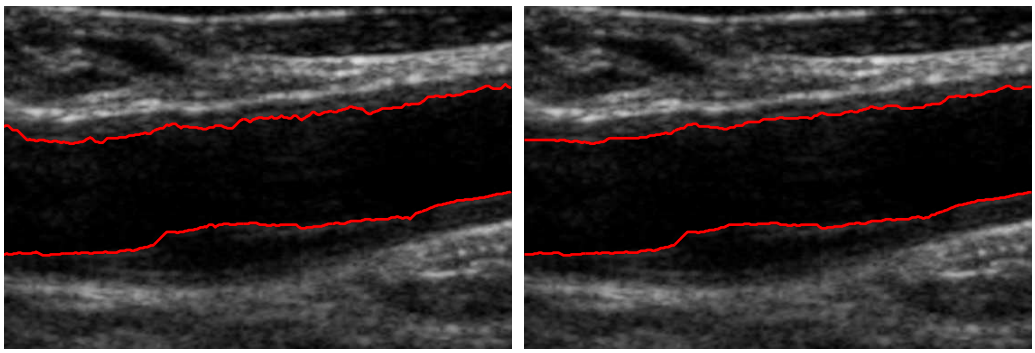

(a) (b)

Fig. 5.22: Lumen boundaries for the image in Fig. 5.11, segmented with dynamic programming: a) Without any geometric constraint ($\lambda = 0$); b) With a geometric constraint ($\lambda = 5$).

The polar version of E and of the ICOV map are computed using inverse mapping, from the polar system, (r, θ), to the cartesian system, (x, y), and selecting the highest value of the pixels surrounding the point (x, y).

When the best path is determined in the polar system, it is converted to the cartesian system through direct mapping. Each polar pixel is mapped to a single cartesian point, (x, y). Then, we choose the neighboring cartesian pixel with the highest ICOV. An alternative would be to round the coordinates of the cartesian points, but the final curve would not be so smooth and its location would be less accurate. Unlike inverse mapping, direct mapping may leave out some pixels of the cartesian curve. However, inverse mapping would produce thicker lines, reducing the accuracy of the boundary location. Besides, the gaps left by the direct mapping are quite small and do not hinder the determination of the cartesian curve.

The dynamic programming algorithm frequently produces open contours, whenever the end points of the best polyline are located at different lines (radius) of the polar matrix. To make sure the path is closed, we introduced the following additional processing. Let i_1^{opt} and i_N^{opt} be the lines of the first and last polar pixels of the optimum polyline, computed with the dynamic programming algorithm. We repeat the backtracking of the best path, but this time starting at line i_1^{opt} of the last column. The new path will quickly converge to the initial best path, resulting in a closed curve that contains most of the points of the initial polyline. Figure 5.23 gives an example of the computed best path for a transversal section, with and without the extra processing used to close the curve.

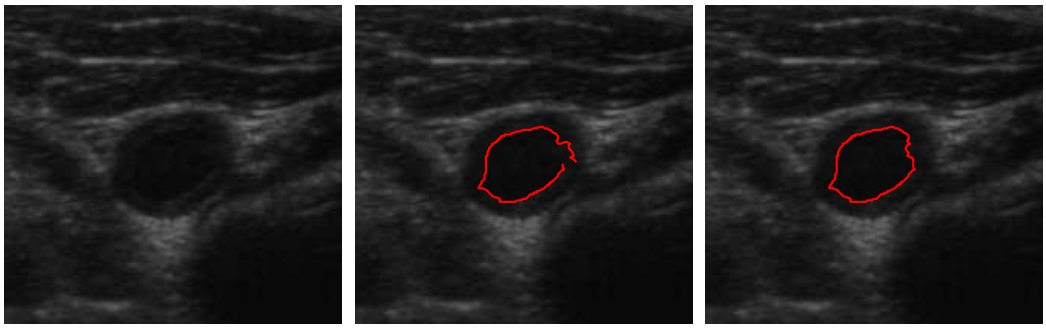

(a) (b) (c)

Fig. 5.23: Detection of the lumen boundary in a transversal section, with dynamic programming and $\lambda = 0$: a) B-mode image of a transversal section; b) Contour obtained by applying the dynamic programming algorithm to the polar grid; c) Contour given by the proposed additional processing, to close the curve.

5.4.3 Weight of the geometric term in the cost function

The geometric constraint may help to avoid deviations from the lumen contour when it is too weak and degraded, as in the example of Fig. 5.24. But this improvement usually requires a very large weight of the geometric term, to overcome the stronger ICOV of the alternative path. The lumen contour must have low curvature at those degraded sections, otherwise, using a strong geometric constraint will introduce more damage than improvement. A strong geometric weight and a lumen boundary with high curvature do not mix well, often resulting in some undesired bypasses through tissue or lumen regions, even when the edge strength is high at the bypassed sections of the boundary. Two examples of this problem are presented in Fig. 5.25. Unfortunately, lumen boundaries frequently contain segments with large curvature, due to plaque formation. In face of this dilemma, we thought it would be more acceptable not to detect some very degraded lumen boundary edges than to sacrifice well defined parts of the boundary that have large curvature. Therefore, we chose to drop the geometric constraint, by setting $\lambda = 0$ in the cost function. The roughness of the detected contour can easily be eliminated though a posterior smoothing, with an algorithm better suited for this purpose.

The segmentations produced for the image in Fig. 5.25 (d) illustrate quite well another limitation of the algorithm. It cannot correctly detect deep concavities nor sharp saliences, specially when they are oriented to the left or to the right, as in the left part of the upper boundary. This limitation is intrinsic to the dynamic programming approach, where the path does not invert the direction of its course during its

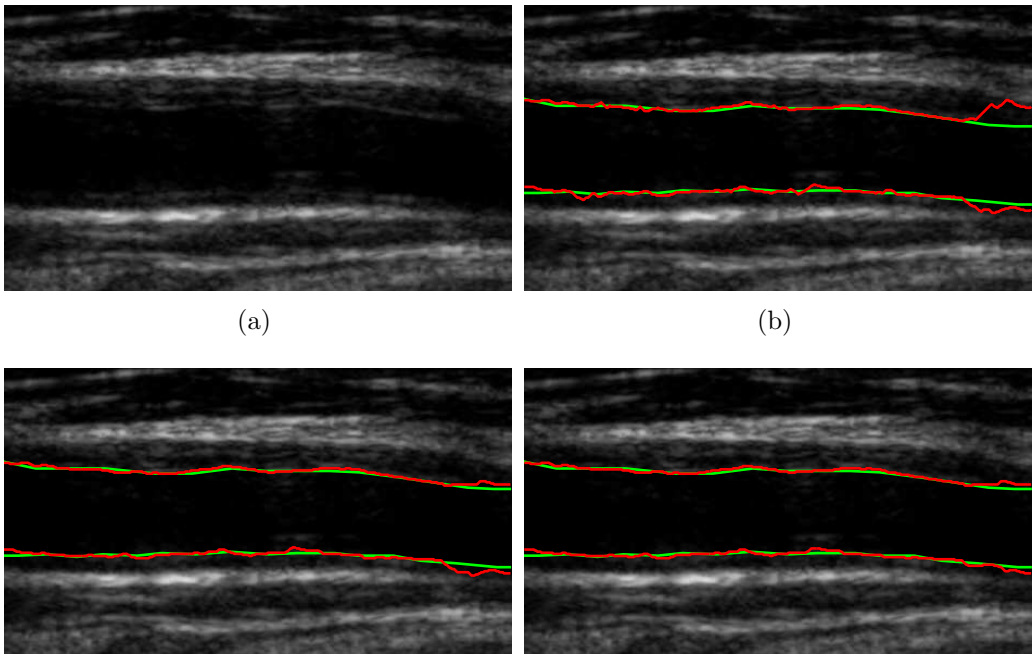

Fig. 5.24: Improved detection due to the geometric term: a) B-mode image of a longitudinal section; b) Detected lumen boundaries (red) with $\lambda = 0$ and the ground truth (green); c) Detected lumen boundaries (red) with $\lambda = 4$ and the ground truth (green); d) Detected lumen boundaries (red) with $\lambda = 5$ and the ground truth (green).

construction. Nevertheless, it is possible to significantly reduce this error through a region-based active contour, which is also used to produce smoother curves. The proposed solution is discussed next.

5.5 Smoothing the detected lumen boundaries

The output of the dynamic programming algorithm presented above is frequently not smooth enough. One simple and very fast solution to this problem is to fit, to the pixels of each computed polyline, a weighted cubic smoothing spline [108], with weights proportional to the value of the ICOV at each pixel. This should be enough if the polyline, produced by the dynamic programming algorithm, closely approximates the lumen boundary at its full length. Otherwise, a region-based active contour is preferable, since it has the power not only to smooth the polyline but also to significantly improve its location. This approach requires a much heavier computational effort than the weighted cubic spline, but it is quite effective for

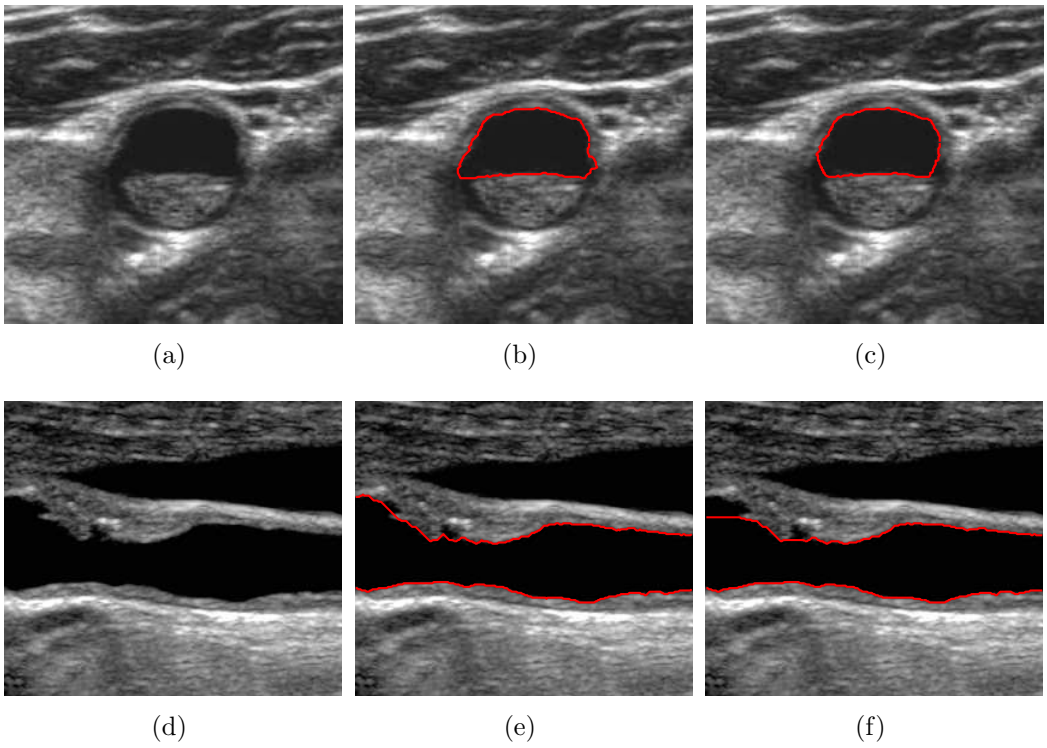

Fig. 5.25: Bypass through the lumen region due to the geometric term: a) B-mode image of a transversal section; b) Detected lumen boundary for image (a), with $\lambda = 0$; c) Detected lumen boundary for image (a), with $\lambda = 5$; d) B-mode image of a longitudinal section; e) Detected lumen boundaries for image (d), with $\lambda = 0$; f) Detected lumen boundaries for image (d), with $\lambda = 2$.

the treatment of large segmentation errors, like those described at the end of the previous section. The Chan-Vese two-phase piecewise constant segmentation model, recently introduced in [97, 98], was the chosen region-based active contour, for its potential, flexibility and accuracy.

5.5.1 The Chan-Vese active contour

The Chan-Vese active contours [97, 98] are geometric snakes in the sense that they are represented implicitly as the zero level set of a 3D surface [22, 23].

Geometric snakes offer several advantages over parametric snakes [70], some of which are: i) the natural treatment of topological changes in the propagating fronts, when they merge together or they pinch apart; ii) the straightforward generalization from two spatial dimensions to three or more spatial dimensions; iii) the existence of very efficient implementations, like the narrow band method [22] or the fast marching method [22].

Most active contours evolve under propagation forces based on gradients. These gradient-based active contours usually fail when dealing with images with high levels of noise or occlusions. If the noise is strong, it may cause the stopping of the contour at false edges and the final contour will be very dependent on its initial position. If there are gaps in the boundaries of the object to be segmented, the contour will not stop at these points.

In [97], the proposed active contour is a region-based model that does not depend on gradients, which makes it very robust to the initial position of the active contour and small gaps in the object boundary. Moreover, it is very accurate, it has the ability to automatically detect interior contours and it is embedded in a level set framework [22, 23].

This active contour belongs to a family of level set formulations of the well-known image segmentation variational model of Mumford and Shah [109], whose functional is

$$\begin{aligned} F(u,C) =& \mu \cdot \text{Length}(C) + \lambda \int_{\Omega} \left[u_0(x,y) - u(x,y)\right]^2 dxdy \\ &+ \int_{\Omega \setminus C} |\nabla u(x,y)|^2 dxdy \end{aligned} \tag{5.26}$$

where μ and λ are positive parameters and u is a smooth approximation of a given image $u_0 : \Omega \rightarrow \mathbb{R}$, with sharp boundaries at C.

In the particular case of a two-phase piecewise constant image, the gradient of

u is zero inside each region and the Mumford-Shah model simplifies to

$$\begin{aligned} F(c_1, c_2, C) =& \mu \cdot \text{Length}(C) + \lambda_1 \int_{inside(C)} [u_0(x,y) - c_1]^2 \, dxdy \\ &+ \lambda_2 \int_{outside(C)} [u_0(x,y) - c_2]^2 \, dxdy \end{aligned} \tag{5.27}$$

where c_1 and c_2 are, respectively, the averages of u_0 inside and outside the region boundaries represented by C, and λ_1 and λ_2 are positive parameters.

In [97], the following level set formulation was introduced for equation 5.27

$$\begin{aligned} F(c_1, c_2, \phi) =& \mu \int_\Omega \delta_\epsilon(\phi(x,y)) |\nabla \phi(x,y)| \\ &+ \lambda_1 \int_\Omega [u_0(x,y) - c_1]^2 \, H_\epsilon(\phi(x,y)) dxdy \\ &+ \lambda_2 \int_\Omega [u_0(x,y) - c_2]^2 \, [1 - H_\epsilon(\phi(x,y))] \, dxdy \end{aligned} \tag{5.28}$$

where: $\phi : \Omega \to \mathbb{R}$ is a Lipschitz continuous function with its zero level set representing the active contour that separates the image regions defined by $\{(x,y) \in \Omega : \phi(x,y) > 0\}$ and $\{(x,y) \in \Omega : \phi(x,y) < 0\}$; H_ϵ and $\delta_\epsilon = H_\epsilon'$ are regularized versions of the Heaviside function H and the Delta function δ, respectively, such that

$$H_\epsilon(z) = \frac{1}{2} \left[1 + \frac{2}{\pi} \arctan\left(\frac{z}{\epsilon}\right) \right] \tag{5.29}$$

Keeping c_1 and c_2 fixed, the minimization of $F(c_1, c_2, \phi)$ with respect to ϕ leads to the following Euler-Lagrange equation [97]

$$\frac{\partial \phi}{\partial t} = \delta_\epsilon(\phi) \left[\mu \text{div}\left(\frac{\nabla \phi}{|\nabla \phi|} \right) - \lambda_1 (u_0 - c_1)^2 + \lambda_2 (u_0 - c_2)^2 \right] \tag{5.30}$$

$$c_1(\phi) = \frac{\int_\Omega u_0(x,y) H_\epsilon(\phi(t,x,y)) dxdy}{\int_\Omega H_\epsilon(\phi(t,x,y)) dxdy} \tag{5.31}$$

$$c_2(\phi) = \frac{\int_\Omega u_0(x,y)(1 - H_\epsilon(\phi(t,x,y))) dxdy}{\int_\Omega (1 - H_\epsilon(\phi(t,x,y))) dxdy} \tag{5.32}$$

Chan and Vese also extended the level set formulation to more general versions of equation 5.27, like the multiphase piecewise constant model and the piecewise smooth model [98].

We have implemented and tested several of these models, including the piecewise

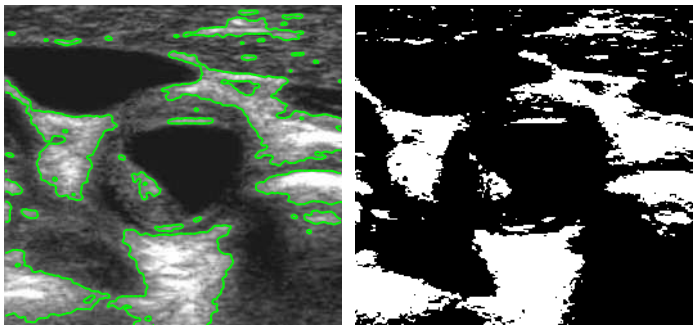

(a) (b)

Fig. 5.26: Segmentation of a B-mode image of the carotid: a) With the Chan-Vese model; b) With the Otsu's thresholding algorithm.

smooth one, which seemed the best theoretical model for the segmentation of images with non-uniform illumination. Unfortunately, with the exception of the two-phase piecewise constant model, all the others suffer from two very annoying problems: i) the extremely large computational complexity; ii) the tendency to stop at local minima that are far away from the global minimum. These problems are more accentuated in the piecewise smooth model and we found it to be of little use in practice.

On the other hand, the two-phase piecewise constant model turned out to be very effective and accurate. The major difficulty in its application to B-mode images of the carotid is their nonuniform echo intensity. In the following section we introduce a modified version of this active contour model that is better suited to deal with this problem.

5.5.2 Hybrid Chan-Vese active contour

In the original Chan-Vese model, the values of c_1 and c_2 are estimated, in each iteration, by minimizing the mean square distance between the gray-scale image to segment and the binary image produced by the segmentation, which is equivalent to the criterion used in the Otsu's thresholding algorithm [106]. The equivalence between the two criteria is evident in the example presented in Fig. 5.26. Therefore, c_1 and c_2 can be viewed as functions of an intensity threshold that is updated as the active contour evolves in space.

We propose a hybrid approach for the segmentation of images with nonuniform illumination. Here, the intensity threshold estimate of the Chan-Vese model is

replaced by a thresholding surface, keeping the rest of its attractive properties. Basically, the proposed hybrid algorithm consists of two image processing stages, in the following order:

1. An optimal smooth thresholding surface, $T_{\text{opt}}(x, y)$, is computed from the intensities found at the edges along the boundaries produced by the dynamic programming algorithm. This is done only once, before the initialization of the active contour, and using the algorithm described in subsection 5.3.10.

2. The image is then processed by a modified version of the Chan-Vese two-phase piecewise constant active contour, for which the constants c_1 and c_2 are determined as functions of $T_{\text{opt}}(x, y)$, such that the intensity threshold is preserved at each pixel.

In the hybrid model, we set $c_1(x, y) = 2T_{\text{opt}}(x, y)$ and $c_2(x, y) = 0$, to keep the intensity threshold as the mean of c_1 and c_2. The active contour is not used to estimate the intensity threshold. It just uses its elastic properties and the intensity topology of the image to clean the noise, smooth contours, improve their position accuracy and close small carotid wall gaps.

Next, we discuss some important details related to the implementation of our hybrid model.

An attractive property of the hybrid model is its faster convergence, compared to the original active contour model.

The implicit function, ϕ, in equation 5.30, is initialized as a signed distance function for which the zero level sets are the curves produced by the dynamic programming algorithm. Since these curves are already very close to the real lumen boundaries, a large number of iterations is saved.

To further reduce the computational effort, the processing is limited to the smallest rectangular box containing the wall contour. An extra pair of lines is added to the top and bottom of this box and an extra pair of columns is added to its sides, in order to keep the wall contour away from the boundaries of the box. This will insure the active contour will stay a closed curve, which might not happen if the lumen region touched the boundaries of the box.

The Chan-Vese model spontaneously detects the interior of objects in an image. While this is a blessing in most cases, it should be avoided in our case. Otherwise, we may end up with more than the two regions we want, i.e., the lumen and the rest of the image. This property disappears if ϕ becomes unable to generate new

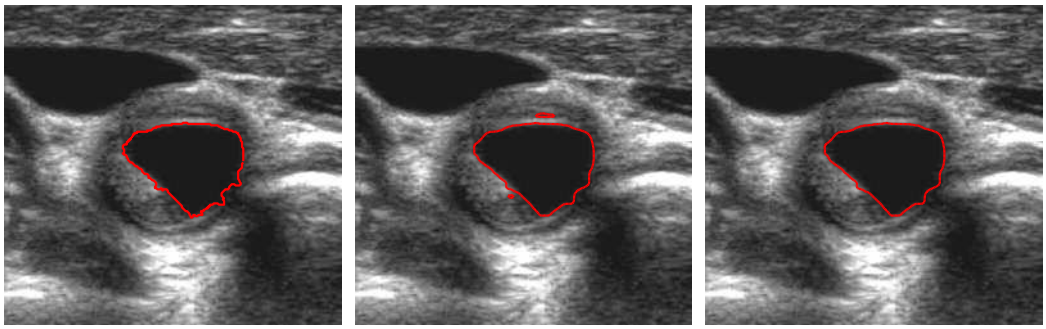

(a) (b) (c)

Fig. 5.27: Inhibiting the detection of new holes in the hybrid Chan-Vese model: a) Initial active contour; b) Segmentation result without inhibiting the detection of new holes inside the carotid; c) Segmentation result inhibiting the detection of new holes.

isolated zero level sets. A fast and simple way to achieve this goal is to inhibit a sign change in ϕ at any pixel for which there is no 8-neighbor with the same new sign. In other words, ϕ is allowed to change sign only at pixels in the vicinity of the active contour. An example of the effect introduced by this restriction is presented in Fig. 5.27.

Since, at this time, we already know the location of the carotid wall, we restrain the evolution of the active contour to the region delimited by the wall, inhibiting any contour leakage at wall sections with weak echo or no echo at all. This restriction is implemented by setting the intensities of the pixels outside the carotid to the highest value of the image gray scale. Figure 5.28 shows an example of a contour leakage through the carotid wall, which is stopped by the described restraint.

The active contour may also leak through the lumen boundary produced by the dynamic programming algorithm, at places where boundary edges are missing. We may reduce this risk by computing the thresholding surface under the restriction of it dropping to zero at some reasonable distance, d, from the carotid. This gives lower thresholds outside the detected lumen boundary, reducing the influence of large values of the ICOV. Other possibilities are: i) to apply a smoothing filter to the intensity profile along the boundary produced by the dynamic programming algorithm; ii) to propagate to non-edge pixels of the contour the smallest intensity at the closest edges pixels of the contour. In practice, the first solution seems to give the best results. We usually set $d = 3\sigma_d$ (the definition and estimation of σ_d can be found in subsection 4.7.4 and section 4.9, respectively), to keep some safety margin from the carotid wall. An example of the contour leakage through the lumen

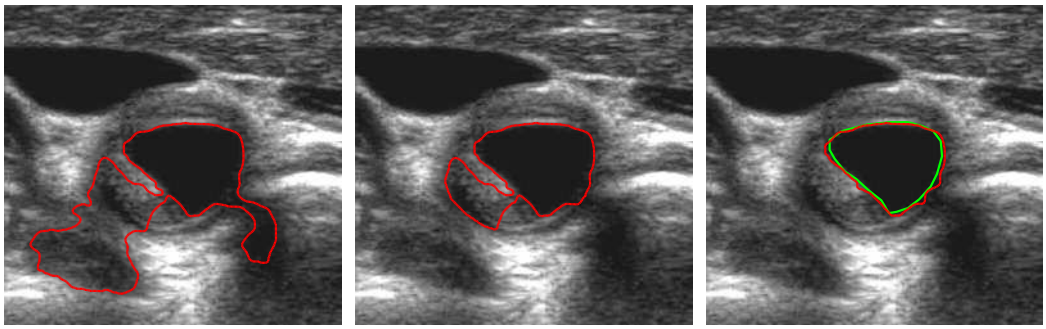

(a) (b) (c)

Fig. 5.28: Leakage of the active contour in the hybrid Chan-Vese model: a) Segmentation with leakage through the carotid wall and through the lumen boundary, processing the whole image; b) Segmentation restrained to the region inside the carotid wall; c) Ground truth (green) and the automatic segmentation (red) when we also force the thresholding surface to zero at a distance $d = 3\sigma_d$ from the carotid.

boundary is presented in Fig. 5.28, where we can also see the improvement obtained with the proposed additional processing. For comparison, the ground truth was included in the last image. Figure 5.29 shows the thresholding surfaces with and without the additional restriction.

Two other examples of the final contour obtained with the hybrid algorithm are presented in Fig. 5.30. The second example shows the significant improvement in the location of the lumen boundary near plaque concavities that could no be detected by the dynamic programming algorithm (see also Fig. 5.25). In both cases, the ground truth is also displayed.

5.6 Results

There are several parameters to be defined in the Chan-Vese two-phase piecewise constant active contour. With the exception of parameter μ, which determines the elastic strength of the contour, all the others were set as suggested in [97, 98]. Therefore, we set: $\lambda_1 = \lambda_2 = 1$, to give equal importance to both phases in the image; $\Delta x = \Delta y = 1$, where $(\Delta x, \Delta y)$ represents the image grid size; the regularizing parameter of the Heaviside and delta functions as $\epsilon = \Delta x$; and the time step as $\Delta t = 0.1\Delta x$.

The semi-implicit numerical scheme proposed in [97, 98] (see appendix E) was used for equation 5.30. This numerical scheme was iterated until the maximum

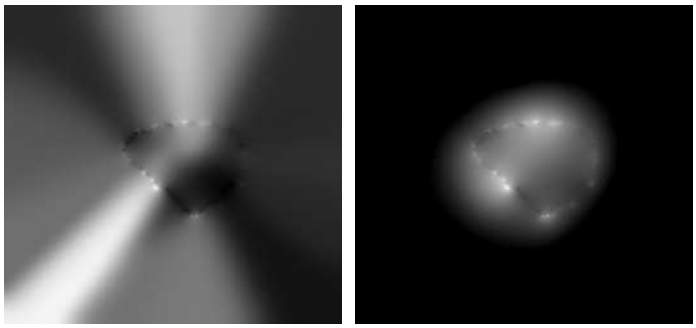

(a) (b)

Fig. 5.29: Thresholding surfaces for the hybrid Chan-Vese model: a) Surface used in the segmentation presented in Fig. 5.28 (a) and Fig. 5.28 (b); b) Surface used in the segmentation presented in Fig. 5.28 (c).

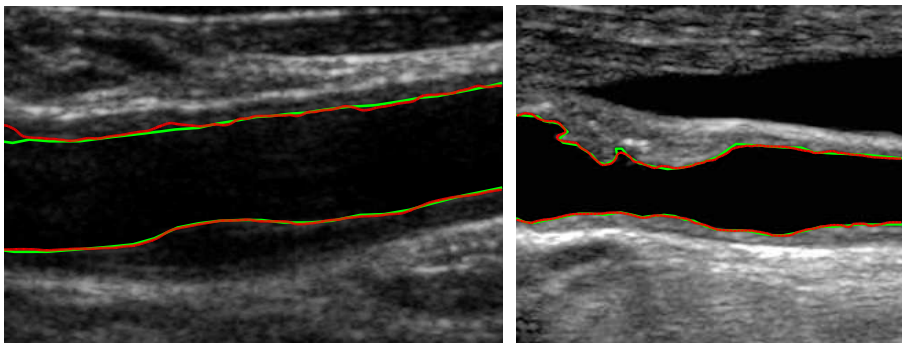

(a) (b)

Fig. 5.30: Ground truth (green) and the lumen boundaries obtained with the hybrid Chan-Vese model (red): a) From the contours displayed in Fig. 5.22 (a); b) From the contours displayed in Fig. 5.25 (e).

distance covered by the active contour became less than $0.01\Delta x$, between two consecutive iterations. In other words, iterations were terminated when the active contour virtually stopped.

Parameter μ can also be seen as a scale parameter, in the sense that the size of the smallest objects detected by the active contour is proportional to the value of μ. So, we defined this parameter as a function of the scale of the segmented lumen, measured by the length, L, of the lumen boundary produced by the dynamic programming algorithm. In longitudinal sections, L is the perimeter of the region delimited by the two estimated contours (one above and the other bellow the medial axis), to better capture the scale of the lumen region. The scale parameter was set as $\mu = \rho L \times 255^2$, where $\rho = 10^{-4}$ was empirically determined as a good compromise between a satisfactory level of smoothing and the fidelity to the data. The factor 255^2, also used in [97, 98], is necessary to keep unity consistence in the level set equation, since the image intensities are represented in the range $\{0, \ldots, 255\}$.

Besides the results presented in Fig. 5.28 (c) and Fig. 5.30, several other examples of successful and unsuccessful segmentations of the carotid lumen are presented in appendices H and I. Next we present several statistics of the segmentation results, computed for our set of images and using the manual segmentations as the ground truth.

Figure 5.31 gives the boxes and whiskers for the maximum distance error, D_{err}, and the relative area error, A_{err}, defined in section 4.9. These statistics were computed for the subset of images for which the wall was successfully segmented. As expected, the errors in the detection of the lumen boundaries are often larger than in the wall detection, due to the typical hypoechogenicity of the plaque. Of course, larger plaques will give larger errors, in case of failure. In many cases, the whole plaque or a significant part of it is only detectable with complementary information, like power-Doppler imaging. The medical specialist seems to add some mental model to the data in the image that allows him to infer the approximate location of the lumen boundary from very poor and discontinued lumen boundaries.

The CPU statistics for the lumen segmentation are presented in Fig. 5.32.

Finally, Fig. 5.33 shows the lumen area error statistics for the segmentation results obtained with thresholding. The maximum distance error was not computed in this case because the detection of a single noisy pixel inside the lumen would distort the results.

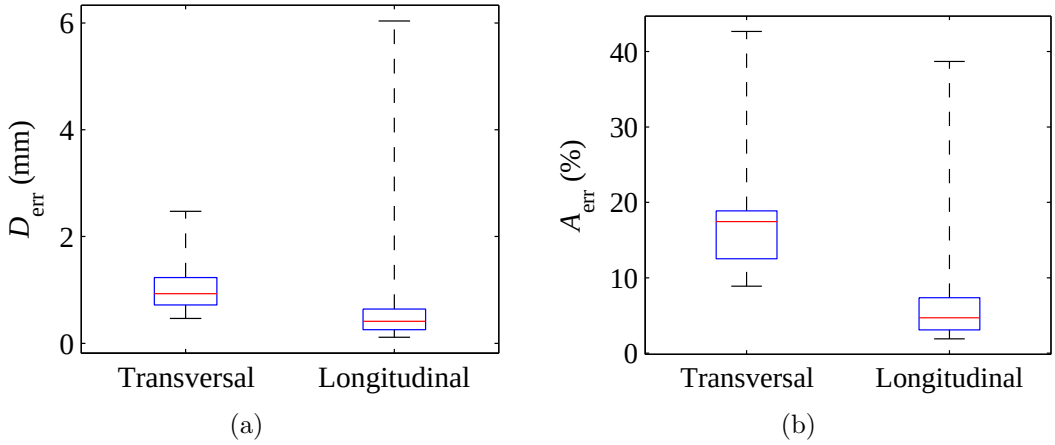

Fig. 5.31: Error statistics for the lumen segmentation: a) D_{err} b) A_{err}.

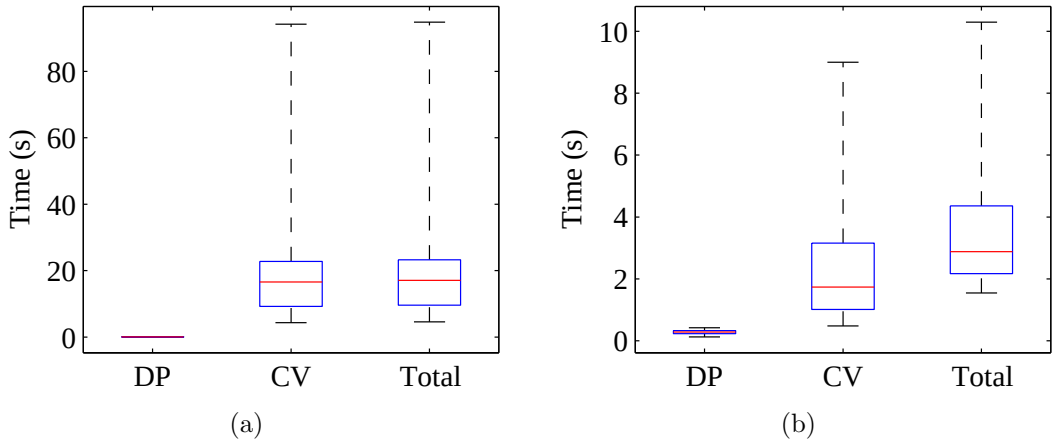

Fig. 5.32: CPU statistics for the dynamic programming (DP), the hybrid Chan-Vese active contour (CV) and the total time spent in the lumen segmentation: a) Longitudinal sections; b) Transversal sections.

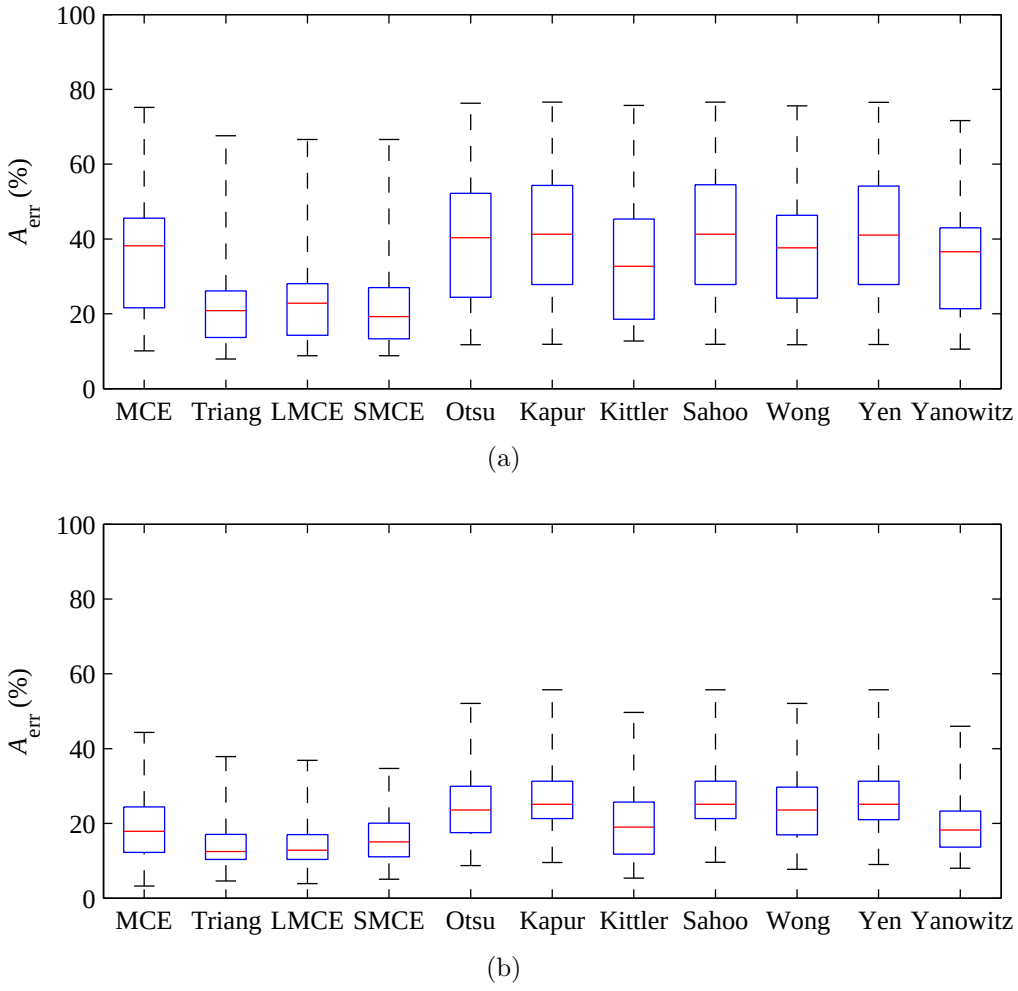

Fig. 5.33: Lumen area error statistics for thresholding segmentation: a) Transversal sections; b) Longitudinal sections.

5.7 Concluding remarks

In thresholding segmentation, the triangle algorithm presented the best results. This is the reason why we used it in chapter 4, to compute a quick rough estimate of the lumen region. The LMCE algorithm was the second best thresholding algorithm. Its results are very close to the triangle algorithm but it has the disadvantage of requiring the knowledge of the wall location. As expected, the results get worse in transversal sections, where the quality of the tissue boundaries is poorer. Unfortunately, even the triangle algorithm failed to give reliable enough segmentations when there is hypoechogenic plaque, significant noise inside the lumen or large echo dropouts over the carotid region.

The proposed dynamic programming algorithm improved the lumen segmentation, but still presents significant errors when the echo along the boundary is too low to produce any reasonable contour. The major drawback of this approach seems to be the impossibility to capture deep concavities and sharp saliences, specially when they are oriented in a direction similar to the direction of the boundary. Another problem is the difficulty in integrating global constraints, like we did for the detection of the carotid wall, which could help improving the poor response at very degraded parts of the lumen boundary. Of course, if there is no signal at all, there isn't much we can do about it, considering it is not possible to use a shape prior. Although the integration of a geometric term is attractive, the results show that penalizing the length of the boundary may cause undesirable bypasses through the interior of tissue regions. Penalizing the variation of the distance to the carotid wall does not seem to work well either, since one can find plaques where this distance varies a lot along the lumen surface. This motivated us to drop the geometric term and do the smoothing in an independent step.

The combination of a smooth thresholding surface and the proposed modified version of the Chan-Vese active contour proved to work well, both in the smoothing and in the reduction of the errors in the location of the boundaries estimated by the dynamic programming algorithm. The main disadvantages of this approach are the computational effort and the risk of leakage of the active contour. If there are no significant errors in the output of the dynamic programming algorithm, a simple smoothing, with a weighted smoothing spline, should be enough, with the advantage of being extremely fast to compute.

In spite of the good results for most of the images, the detection of the lumen boundaries often fails in images with very poor quality, which are common in clinical

practice. More studies should be pursued in order to reduce the gap between the error rates in manual and automatic segmentations.

Chapter 6

RECONSTRUCTION OF THE CAROTID 3D SURFACE

6.1 Introduction

Performing the segmentation of the carotid boundaries in 2D B-mode sections is convenient because they are more familiar to medical doctors, facilitating the validation of the results and eventual corrections.

On the other hand, a 3D surface reconstruction of these boundaries has the advantage of allowing other perspectives, through re-slicing of the data, that may help to produce a better diagnosis.

One may take the best of both approaches by reconstructing the surfaces of the carotid wall and of the lumen boundary directly from the segmented contours of a sequence of B-scans of the artery. This procedure has several advantages relative to alternatives based on data interpolation into voxels, as pointed out in chapter 2. The validity of this approach was confirmed by a recent work [78], in which an ellipse was used as a geometric model of the wall contour in each 2D transversal section of the carotid. However, the authors of this work did all the segmentations by hand. Some other relevant differences between their work and ours are: a) the approach used to smooth the medial axis and the wall surface of the carotid; b) the treatment of the lumen boundary after the wall smoothing; c) the algorithm used to obtain new slices normal to the main axis.

The chapter starts with a brief overview of the approach, followed by several sections which present and discuss, in detail, the algorithm proposed for the automatic reconstruction of the 3D carotid surfaces, from a sequence of parallel transversal slices of the CCA. The following sections introduce new algorithms for surface reslicing in arbitrary directions and normal to the medial axis of the artery. Then, some results and 3D measures of the carotid are presented. The chapter ends with

a section of concluding remarks.

6.2 Overview of the approach

Both the carotid wall surface and the lumen boundary surface are reconstructed.

The proposed algorithm starts by segmenting the carotid wall and the lumen boundary contours in each B-mode image of the 3D volume, using the segmentation algorithms proposed in chapters 4 and 5.

The segmented contours are resampled and the resulting set of points is used to obtain a first estimate of the 3D surfaces, after matching the sampled points between different frames.

Due to location errors of the volume slices, the obtained surfaces are rugged and need to be smoothed, which is done with smoothing splines. First, a strong smoothing is applied to the 3D curve that links the centroids of the carotid wall contours. This step serves to align the segmented carotid wall contours and introduces a significant improvement in the smoothness of the carotid wall surface, but is not enough to produce the desired level of smoothness. Therefore, this surface is subjected to a weaker additional smoothing. The displacements of the carotid wall points, caused by the axis smoothing and wall surface smoothing, are transmitted, through interpolation, to the points of the lumen surface. Finally, the lumen surface also receives some very weak smoothing, which further improves the quality of the surface without loosing a strong fidelity to the lumen data.

A fast and simple algorithm is introduced to reslice the reconstructed surfaces in new positions and orientations. The problem of slicing a 3D surface consists in determining the sliced 3D contour, defined as the intersection between an arbitrary slicing plane and the surface to be sliced. Using a rigid geometric transformation of the surface to be sliced, the problem can be viewed as the determination of the zero level set of a 3D surface. This level set is a 2D contour, corresponding to the projection of the sliced 3D contour in the slicing plane. The 3D contour can be obtained from the determined level set, by inverting the geometric transformation applied to the surface. But the level set may be enough for some applications, like the computation of cross sectional areas.

The problem of reslicing in the direction normal to the medial axis of the carotid wall is also addressed. In the proposed algorithm, the slice that passes through a given 3D point and is normal to the medial axis is determined as the slice containing that point and that minimizes the area inside the wall contour in the slice.

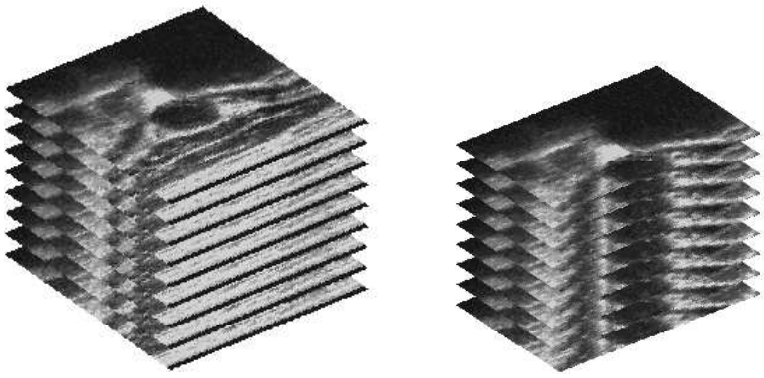

(a) (b)

Fig. 6.1: A 3D volume acquired with a 3D freehand system: a) Sequence of B-mode images; b) A cut of the 3D volume.

6.3 The freehand 3D volume

The processed data consists of a sequence of parallel transversal slices, obtained with a 3D freehand system and illustrated by the example in Fig. 6.1. This is the usual form of the data for this kind of applications.

Longitudinal sections could also be included and used to improve the alignment of the transversal sections. In fact, the integration of the longitudinal information may be the best way to reduce the alignment errors between the segmented contours of different transversal sections, specially for the lumen surface, where a strong smoothing is out of the question.

In a more general approach, we could consider the acquisition of 2D slices with arbitrary orientation. This approach introduces some undesired issues. First, the ultrasound probe needs a 3D location tracker to estimate and save the 3D position and orientation data of each image. The idea of connecting extra hardware to the ultrasound machine is not very attractive since it disturbs the routine of the examination and causes extra difficulties to the medical doctor. Some probes come with a built in 3D tracker and, with a proper ultrasound machine, can be used to acquire 3D volumes. But the acquired data is protected by the manufacturer and it is not available to export from the machine. Second, it is known that the quality of the ultrasound image is related to the angle of incidence of the ultrasound beam at the organ boundaries. A small angle will generally produce poorly defined boundaries, which would compromise the image segmentation results. In a modality like ultrasound imaging, where the image quality is so low, this detail is very important.

That is why specialists prefer to acquire slices normal to the longitudinal axis of the artery.

Besides the set of 2D images, another important complementary information for the surface reconstruction is the voxel size, $(\Delta x, \Delta y, \Delta z)$, which is frequently saved in a separate text file.

Since our segmentation algorithm was conceived for the CCA, only this part of the scanned artery was considered for 3D reconstruction.

6.4 Segmentation of the 3D volume

The segmentation of the volume is done sequentially, one 2D B-mode image at a time, using the segmentation algorithms described in chapters 4 and 5.

The carotid boundaries segmented in each transversal section image are used to initialize the segmentation of the next image in the sequence.

The segmentation algorithm starts by asking the user to click at a point near the centroid of the lumen in the first frame of the 3D volume. This first estimate is replaced, after the image segmentation, by the centroid of the detected lumen boundary contour. The final estimate of the lumen centroid in each image is used as the first estimate of the lumen centroid in the next frame of the volume sequence.

The RANSAC search during the segmentation of the wall, for all frames except the first, is limited to a narrow band around the ellipse found for the previous frame. In the first frame, a ROI around the lumen centroid is selected and segmented, as described in chapter 4. This will considerably reduce the processing time. Figure 6.2 shows the segmented carotid wall contours for each frame of a 3D volume.

The segmented lumen boundary contour in each frame is saved in a file as a chain of 2D coordinates, (x, y), before proceeding to the segmentation of the next frame in the volume. The (x, y) coordinates are relative to the associated frame. The parameters of the best ellipse fitted to the carotid wall are also saved, in another file. These files may be used, afterwords, to compute the 3D surfaces of the carotid boundaries. This clear separation between the segmentation and the surface reconstruction is not only convenient but also desirable. In fact, the results of the automatic segmentation may be used for other purposes, like the visualization and eventual correction of the segmented boundaries. The surface rendering, based on the set of previously segmented contours, is very fast, taking no more than one or two seconds, making it adequate for real-time user interaction. The same cannot be stated about the segmentation step, which is a heavy task, requiring at least three

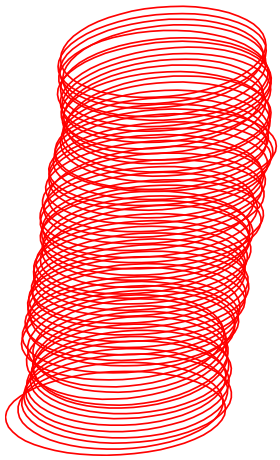

Fig. 6.2: Segmented carotid wall contours of a 3D volume.

or four minutes to complete.

6.5 Rendering of the 3D surfaces

A 3D surface can be rendered using Matlab, with the function $mesh(X, Y, Z)$. The parameters X, Y and Z are m-by-n matrices, where m is the number of frames and $n-1$ is the number of points per frame. The x, y and z coordinates of the j^{th} point of the i^{th} frame are saved in $X(i,j)$, $Y(i,j)$ and $Z(i,j)$, respectively. To obtain a cylindrical surface, the curves described by each line of X, Y and Z must be closed, which means the first and the n^{th} columns of these matrices must be equal. In other words, a closed curve is represented by a polygon with $N = n - 1$ vertices.

The number of points per frame must be equal. Therefore, the segmented contours in each B-scan must be re-sampled to obtain a constant number of points. Fortunately, not all the points of the segmented contours are necessary to obtain a good representation of the desired boundary surface. Usually, a sample of $N = 50$ points, equally spaced along the contour, is quite enough in practice.

The order sequence of the elements in matrices X, Y and Z determines the connections between the corresponding 3D points. Each patch in the mesh is defined by 4 vertices, with coordinates $(X(i,j), Y(i,j), Z(i,j))$, $(X(i+1,j), Y(i+1,j), Z(i+1,j))$, $(X(i,j+1), Y(i,j+1), Z(i,j+1))$ and $(X(i+1,j+1), Y(i+1,j+1), Z(i+1,j+1))$, such that $1 \leq i \leq m-1$ and $1 \leq j \leq n-1$.

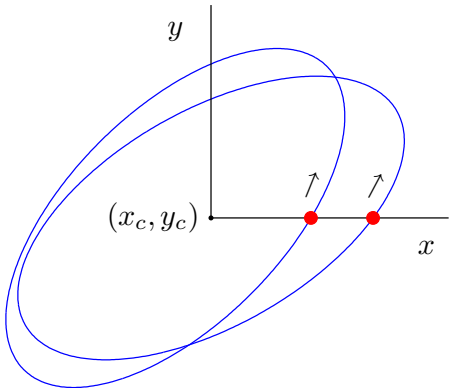

Fig. 6.3: Matching points between ellipses: each ellipse is run in the counter-clockwise direction and its starting position (red dot) is the positive intersection with the x axis, after translating the ellipse to the origin.

6.6 Matching points between consecutive curves

The sample of contour points in each frame must be well matched with the samples of the adjacent frames, otherwise, the surface mesh will not be correctly built. In the case of ellipses, the contour is represented by a set of 6 parameters. With this information, it is easy to start the sampling at the same angle and choose the same direction to walk along the ellipse. We chose to always start at the positive intersection of the ellipse with the x axis, after translating it to the origin, and walk in the counter-clockwise direction (or the clockwise direction, if the y axis is pointing down). This is illustrated in Fig. 6.3.

At the output of the segmentation stage, each lumen boundary contour is described by a sequence of points that are usually not well matched with the points of the curves in adjacent frames. As shown in Fig. 6.4 (a), in some cases, these curves may not even run in the same direction. To get a good matching between the curve points of consecutive frames, the points in each frame may have to be shifted backwards or forwards, along the corresponding line in matrices X, Y and Z. Moreover, a curve also has to be flipped over if it does not run in the same direction as the curve in the previous frame. Let $\delta = 1$ represent a flipping of the curve, $\delta = 0$ represent no flipping, $k \in \{0, 1, ..., N-1\}$ the size of the shifting and $i \in \{2, 3, ..., m\}$ the i^{th} curve to match. Then, the optimum values of δ and k for the i^{th} curve are computed as

$$(\delta_i^{\text{opt}}, k_i^{\text{opt}}) = arg \min_{\delta,k} d(i, \delta, k) \tag{6.1}$$

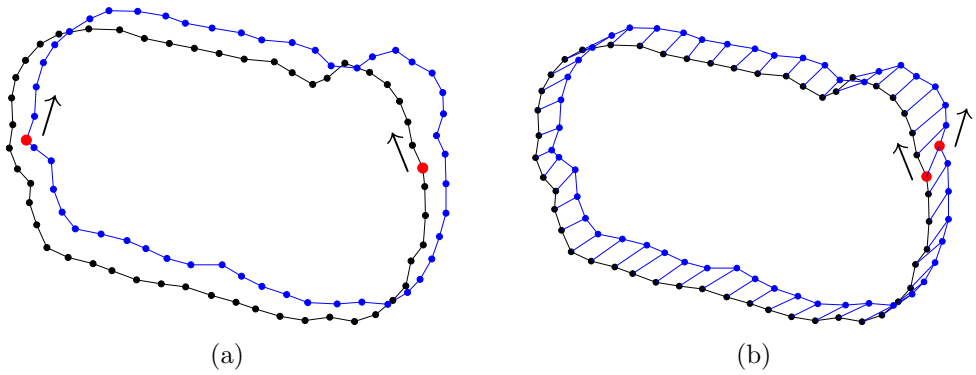

(a) (b)

Fig. 6.4: Matching points between contours of the lumen boundary: a) Sampled points in two consecutive frames, with starting positions and running directions indicated by the red dots and the arrows, respectively; b) Matching after the optimal shifting and flipping.

with

$$d(i,0,k) = \sum_{j=1}^{N} \|p_{i-1,j} - p_{i,((j-1+k) \bmod N)+1}\| \tag{6.2}$$

$$d(i,1,k) = \sum_{j=1}^{N} \|p_{i-1,j} - p_{i,((N-j+k) \bmod N)+1}\| \tag{6.3}$$

where N is the number of curve points per frame and $p_{i,j}$ is the 3D position of the j^{th} point of the i^{th} curve.

Figure 6.4 (b) shows the curves of Fig. 6.4 (a), after matching their points according to the above criterion.

6.7 Alignment of the segmented carotid wall contours

When the image acquisition is made with a freehand 3D system, it is very difficult to avoid some alignment errors between different frames of the 3D volume. Therefore, the resulting surfaces will be far from smooth, as can be seen in Fig. 6.5 (a), for the case of the carotid wall surface.

A good way of reducing this alignment error, as suggested in [78], is to fit a weighted cubic smoothing spline [108], $f(s)$, to the centroids of the segmented wall

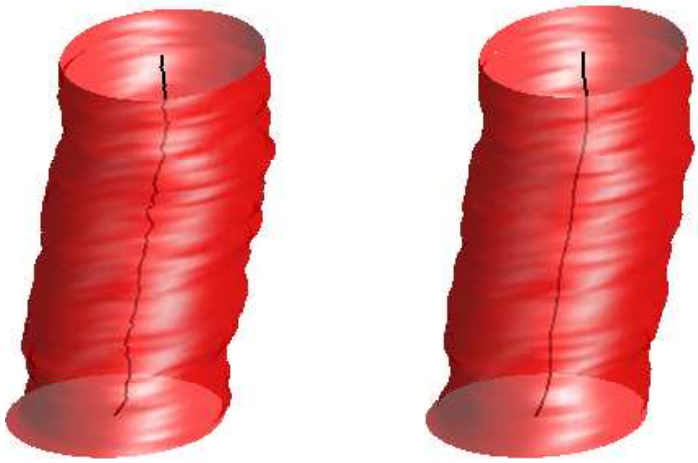

(a) (b)

Fig. 6.5: Wall surface alignment: a) Wall surface obtained directly from the matched segmented 3D contours, without any alignment processing; b) Wall surface after alignment with our algorithm.

contours, by minimizing the following expression

$$p \sum_i w_i \left(v_i - f(s_i)\right)^2 + (1-p) \int_0^L f''(s)^2 ds \tag{6.4}$$

where: p is a real-valued smoothing parameter in the range $0 \leq p \leq 1$; w_i is the weight of the i^{th} centroid; v_i represents the x, y or z component of the position vector of the i^{th} centroid; s_i is the value of the arc-length parameter, $s \in [0, L]$, at the i^{th} centroid; and $f''(s)$ is the second derivative of f with respect to s. The value of p determines the balance between the smoothness of f and the fidelity to the data. For $p = 0$, f is the least-squares straight line fit to the data. At the other extreme, $p = 1$, f is the natural cubic spline interpolant.

The fitting can be made robust to outliers by using different weights for the centroids. In [78], the weights were computed with a 'leave-one-out' scheme. Each weight is computed as $w_i = d_i^{-3}$, where d_i is the Euclidean distance between the i^{th} centroid and the smooth spline obtained from all the other centroids, with uniform weighting. When the weights for all the centroids are known, a final smooth spline is computed using all the centroids and their estimated weights. This method has two problems. First, it is computationally heavy, since the number of centroids is usually large. Second, the distance function for each weight is chosen empirically.

We use a more natural and faster method to determine the weighted smooth cubic spline. In fact, it usually takes only a fraction of a second, in Matlab. We take advantage of the tools of robust statistics described in chapter 4, in particular the CMAD estimator and the Tukey's function, presented in equations 4.2 and 4.4, respectively. The estimation of the weighted smooth cubic spline, $v = f(s)$, for each coordinate, x, y and z, is summarized in the following steps:

1. Using equal weights and all the centroids, determine a smooth cubic spline, $f(s)$.

2. Compute the spline residuals, $r_i = v_i - f(s_i)$.

3. Estimate the CMAD of the residuals. Since the median of the spline residuals is zero, the expression simplifies to $C\text{MAD}(r) = C\text{med}|r|$.

4. Set the weight at each centroid as $w_i = g(r_i; \sigma)$, where $g(ri; \sigma)$ is the Tukey's function for a residual r_i, with scale given by $\sigma = \sqrt{5}C\text{MAD}(r)$.

5. Using the new weights and all the centroids, determine a new smooth cubic spline $f^*(s)$.

6. Compute the new spline residuals, $r_i^* = v_i - f^*(s_i)$.

7. If, for any centroid, $|\frac{r_i^* - r_i}{r_i^*}| > \epsilon$, where ϵ is a small positive threshold ($\epsilon = 1\%$ is quite enough), then make $r_i = r_i^*$ and $f = f^*$ and go back to step 3. Otherwise, take the new spline as the weighted cubic spline estimate for the given data.

The smoothing parameter is set as

$$p = \frac{1}{1 + \frac{h^3}{0.6}} \tag{6.5}$$

where h is the average spacing of the data sites, since this value of p is known to give satisfactory smoothing[1]. Figure 6.5 (b) shows an example of the alignment improvement achieved by our algorithm.

6.8 Smoothing of the carotid wall surface

From Fig. 6.5 (b), it is evident that, in spite of the significant reduction of the surface irregularities, in general, the alignment of the centroids is not enough to produce

[1] http://www.mathworks.com/access/helpdesk_r13/help/toolbox/splines/csaps.html

the desired smooth carotid wall surface. In fact, this problem is difficult to eliminate completely, without risking over-smoothing the data, in volumes acquired with freehand systems. But the results may be further improved by a small additional smoothing of the wall surface itself.

In [78], the smoothing of the carotid wall surface is done by fitting longitudinally oriented smooth splines to matched points from adjacent cross-sectional carotid contours. This has the disadvantage of smoothing only in the longitudinal direction. Moreover, if the carotid bifurcation is also considered, an extra and specific treatment is required for some of the points above the bifurcation.

It makes more sense to look for the smooth surface that best approximates the complete set of 3D points. This way, the smoothing at each surface point takes into consideration all the information from the point neighborhood, and not only the information from the longitudinal direction. The general problem is quite complex, involving both interpolation and approximation of sparse non-uniformly spaced 3D data, and it may be solved with powerful but heavy tools, like the radial basis function (RBF) interpolation [110]. But, in our case, we only consider the common carotid artery, that has a simple cylindrical shape. Therefore, the surface smoothing can be achieved with a generalization of equation 6.4. This solution is very fast and produces very good results. It is used to compute a bi-variate tensor-product smoothing spline for the matched and aligned (X, Y, Z) data of the carotid wall, with uniform weighting.

The surface is represented as a parametric vector valued function, $F(s,u) = (X(s,u), Y(s,u), Z(s,u))$, where s parameterizes the curve of the medial axis (that passes through each centroid) and u parameterizes the curve in each frame, which, ideally, should be perpendicular to the medial axis. Both parameters are normalized to the range $[0, 1]$.

Two smoothing parameters, p_s and p_u, have to be specified, one for each surface parameter. Both of them fall in the range $[0, 1]$ and both are computed as in equation 6.5, by replacing h with the average spacing of the data sites in s and u, respectively.

Along the u direction, the surface is closed and can be seen as a periodic function of u. $F(s,u)$ is computed over one period in the s direction and over three periods in the u direction. Then, the middle period of the resulting smooth surface is selected. This procedure reduces to virtually zero the discontinuities at the junction of the tube along the direction of u. Figure 6.6 shows the surface presented in Fig. 6.5 (b) after the additional smoothing produced by the algorithm just described.

Fig. 6.6: Carotid wall surface presented in Fig. 6.5 (b) after an additional smoothing of the surface itself.

6.9 Readjustment of the lumen position

Unlike the carotid wall surface, the lumen surface may present some irregularities that are not caused by errors introduced by the freehand image acquisition system. The plaque deposits may be responsible for some of these irregularities. Therefore, a direct smoothing of the lumen surface is a risky step because one could be wiping off important data and invalidating the diagnosis. But, the deformation of the carotid wall, due to the smoothing of its surface and of the medial axis, must be transmitted to the points of the lumen surface.

Since, at each frame, all the lumen points fall inside the region enclosed by the carotid wall contour, the induced deformation of the lumen surface can be estimated through interpolation. One may use 2D interpolation, in each frame, to estimate each component of the 3D dislocation vector at each point of the lumen contour in that frame.

To compute the interpolation, it is more convenient to view the 3D points of the carotid boundaries as 2D points in the plane of the frame to which they belong. From this perspective, the 3D dislocation vector, $\overrightarrow{r}_j$, for the j^{th} curve point of a frame is associated to a unique 2D point, $P_j = (x_j, y_j)$, in that plane.

The interpolation problem for each frame can be posed as the computation of an interpolation surface from a set of interpolating data located at points in the plane. Three interpolating surfaces have to be computed in each frame, one for each of the

x, y and z components of the dislocation vectors.

The interpolation surface could be computed as a potential surface, as described in subsection 5.3.10. But, in the present case, the points of the carotid wall and lumen contours rarely coincide with image pixels. Therefore, the wall points have to be approximated by the closest pixel, before computing the interpolation surface. This introduces errors in the data, which are proportional to the size of the grid step. Moreover, the dislocations at the lumen points have to be interpolated from the values of the interpolation surface at the surrounding pixels. These problems motivated the search for other solutions that are better tailored for the problem in question. Two possible alternatives are the weighted average and the thin-plate interpolation surfaces, which are discussed next.

6.9.1 Weighted average interpolation surface

An interpolation surface can be obtained as a weighted average of the interpolating data. The value of the interpolation surface, f, at an interpolated point (x_k, y_k), is given by

$$f(x_k, y_k) = \frac{\sum_j w_{k,j} v(x_j, y_j)}{\sum_j w_{k,j}} \tag{6.6}$$

where $v(x_j, y_j)$ represents the interpolating data at the site $P_j = (x_j, y_j)$ and $w_{k,j}$ is the weight of the j^{th} interpolating point when the data is interpolated at $P_k = (x_k, y_k)$. Each weight is computed as $w_{k,j} = 1/\Phi(d_{k,j})$, where $\Phi(d_{k,j})$ is a monotonically increasing function of the distance, $d_{k,j}$, between points P_k and P_j, and $\Phi(0) = 0$.

This method is very simple and fast, since the data at the set of interpolated points can be estimated without actually having to build an interpolation surface. However, this approach has two important drawbacks: first, the choice of Φ is arbitrary; second, the produced surface may not be very smooth, specially around the interpolating points, as can be seen in the example of Fig. 6.7.

6.9.2 Thin-plate interpolation surface

A thin-plate smoothing spline[2] can be used to build smooth interpolation surfaces from data located at a set of sites in the plane. The thin-plate smoothing spline, f,

[2] http://www.mathworks.com/access/helpdesk_r13/help/toolbox/splines/tpaps.html

Fig. 6.7: Weighted average interpolation surface, with $\Phi(d) = d^2$, for the set of interpolating points represented by the black dots.

is the unique minimizer of the weighted sum

$$\begin{aligned} & p \sum_j \left[v(x_j, y_j) - f(x_j, y_j) \right]^2 + \\ & (1-p) \int_{\mathbb{R}^2} \left[f_{xx}^2(x,y) + 2 f_{xy}^2(x,y) + f_{yy}^2(x,y) \right] dxdy \end{aligned} \tag{6.7}$$

where: p is a real-valued smoothing parameter in the range $0 \leq p \leq 1$; $v(x_j, y_j)$ represents the x, y or z component of the dislocation vector, $\overrightarrow{r}_j$, at the j^{th} interpolating point, with coordinates (x_j, y_j); f_{xx}, f_{xy} and f_{yy} are the second order derivatives of f with respect to x and y. The value of p determines the balance between the error of f, measured by the summation term, and the roughness measure given by the integrand term. When $p = 0$, f is the least-squares approximation to the data by a linear polynomial. When $p = 1$, f is the thin-plate spline interpolant to the data.

One may set $p = 1$ in the above equation and use it to estimate a very good smooth interpolation surface, as the one presented in Fig. 6.8. The main disadvantage of this method is that its computation time grows very fast with the number of data points, since it involves the solution of a full linear system with as many unknowns as there are data points. We found it to be a good solution as long as we do not use much more than 50 points to represent the wall contours in each frame. Otherwise, perhaps it is better to use potential surfaces with a small grid step.

Figure 6.9 shows the curves of the segmented carotid boundaries, in a frame of a 3D volume, before and after the deformation caused by the smoothing operations. As can be seen in this example, the smoothing operations may introduce an error in the plaque area, which is corrected quite well by the interpolation step.

Fig. 6.8: Thin-plate interpolation surface, for the set of interpolating points represented by the black dots.

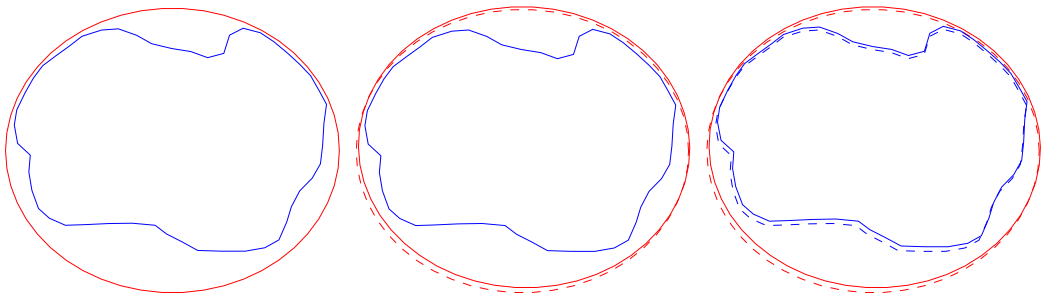

Fig. 6.9: Carotid wall (red) and lumen (blue) contours in a frame of a 3D volume: a) Before any smoothing; b) After smoothing the medial axis and the wall surface (the dashed curve is the original version); c) After interpolating the dislocation of the lumen surface (the dashed curves are the original versions).

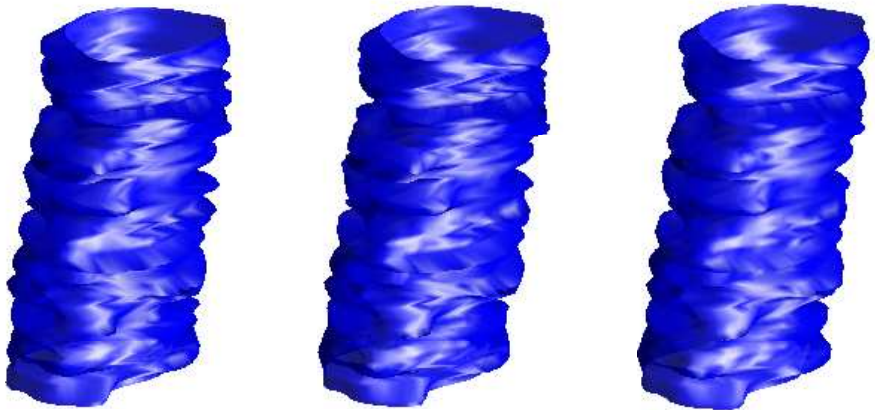

(a) (b) (c)

Fig. 6.10: Example of a lumen surface: a) Obtained directly from the segmented lumen contours; b) After interpolating the deformation of the wall surface; c) After a light smoothing of the interpolated lumen surface.

In Fig. 6.10, one can see the lumen surfaces obtained from a 3D volume, before and after the interpolation of the deformation induced by the smoothing of the medial axis and the wall surface. Interpolating the deformation of the wall surface does not necessarily produce a smoother lumen surface. In fact, as illustrated in the example of Fig. 6.11, some sharp edges may even become sharper, resulting in a more irregular surface at those regions.

The presence of plaque may introduce some irregularity in the lumen surface. But most of the irregularities observed in the reconstructed lumen surface are caused by location errors in the segmented lumen contours. The magnitude of these errors tends to be larger when the plaque is hypoechogenic and large extensions of its boundaries are missing. Although it is tempting to introduce additional smoothing to the lumen surface, there is the risk of wiping off important details of the plaque. This risk will be small if the level of smoothing is low. Figure 6.10 (c) shows the result of applying, to the interpolated lumen surface, a smoothing similar to the one used for the wall surface, but with a stronger fidelity to the data. Here, to make sure the smoothed surface closely follows the data, the smoothing parameters are computed as $p_s = 1/(1 + h_s^3/60)$ and $p_u = 1/(1 + h_u^3/60)$, where h_s and h_u are the average spacings of the lumen data sites in the direction of parameters s and u, respectively[3].

[3] http://www.mathworks.com/access/helpdesk_r13/help/toolbox/splines/csaps.html

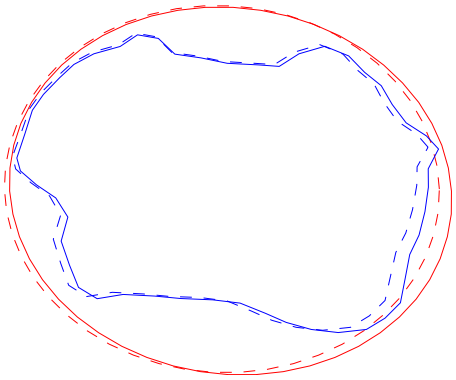

Fig. 6.11: Interpolated lumen contour with sharp edges.

6.10 Surface slices

An important issue for the analysis of 3D volumes is the computation of arbitrary slices. Most software in this field come with functions that compute slices of data volumes in uniform grids. But, in our case, we need the intersection contour between a specified slicing plane and a 3D surface. One could conceive and implement a specific algorithm for this purpose. This is, perhaps, the ideal solution. A more practical alternative is to take advantage of a general use algorithm that computes level sets of a 3D surface. The idea is to apply a rigid geometric transformation to the surface we want to slice, such that the slicing plane becomes coincident with the x-y plane, and then compute the zero level set of the transformed surface. To represent this level set in the original reference frame, the inverse geometric transformation is applied. Although this is an indirect method, it is fast, relatively simple to implement and works well in practice.

A slicing plane is completely defined by one of its points, $P_0 = (x_0, y_0, z_0)$, and a vector, $\overrightarrow{n} = (a, b, c)$, that is normal to the plane. Analogously, the x-y plane can be defined by the point at the origin, $(0, 0, 0)$, and a vector normal to that plane, like the vector $\overrightarrow{v} = (0, 0, 1)$. The equation of the plane normal to vector $\overrightarrow{n}$ and passing through point P_0 is

$$\overrightarrow{n} \cdot (P - P_0) = 0 \tag{6.8}$$

where $P = (x, y, z)$ and the dot represents the inner product. From here, it is simple to find the general equation of this plane, given by

$$ax + by + cz + d = 0 \tag{6.9}$$

with $d = -(ax_0 + by_0 + cz_0)$.

Any point, $P = (x, y, z)$, of the slicing plane can be mapped into the x-y plane through the following rigid body geometric transformation

$$P' = R(\overrightarrow{u}, \theta)(P - T) \tag{6.10}$$

where $P' = (x', y', z')$ is a point in the x-y plane, $R(\overrightarrow{u}, \theta)$ is a 3D rotation matrix and T is a translation vector. The direction about which to rotate is indicated by vector $\overrightarrow{u}$ and θ is the angle of rotation.

Since the inverse of a rotation matrix is its transpose, the mapping from the x-y plane back to the slicing plane can be computed as

$$P = R^T(\overrightarrow{u}, \theta)P' + T \tag{6.11}$$

where R^T is the transpose of R.

The translation, T, of the slicing plane, relative to the x-y-z reference frame, may be defined as the position vector of the intersection between the slicing plane and the normal line passing through the origin. This definition leads to the following equation for T (see appendix C)

$$T = -\frac{d}{\|\overrightarrow{n}\|^2}\overrightarrow{n} \tag{6.12}$$

The rotation angle, θ, of the slicing plane is such that

$$\cos(\theta) = \frac{\overrightarrow{n} \cdot \overrightarrow{v}}{\|\overrightarrow{n}\|\|\overrightarrow{v}\|} \tag{6.13}$$

which gives

$$\theta = \arccos\left(\frac{c}{\|\overrightarrow{n}\|}\right) \tag{6.14}$$

In three dimensions, a rotation can be defined by a single angle of rotation, θ, and the direction of the rotation axis specified by a unit vector, $\overrightarrow{u} = (\alpha, \beta, \gamma)$. The rotation matrix, $R(\overrightarrow{u}, \theta)$, is

$$\begin{bmatrix} \cos\theta + \alpha^2(1-\cos\theta) & \alpha\beta(1-\cos\theta) - \gamma\sin\theta & \alpha\gamma(1-\cos\theta) + \beta\sin\theta \\ \alpha\beta(1-\cos\theta) + \gamma\sin\theta & \cos\theta + \beta^2(1-\cos\theta) & \beta\gamma(1-\cos\theta) - \alpha\sin\theta \\ \alpha\gamma(1-\cos\theta) - \beta\sin\theta & \beta\gamma(1-\cos\theta) + \alpha\sin\theta & \cos\theta + \gamma^2(1-\cos\theta) \end{bmatrix} \tag{6.15}$$

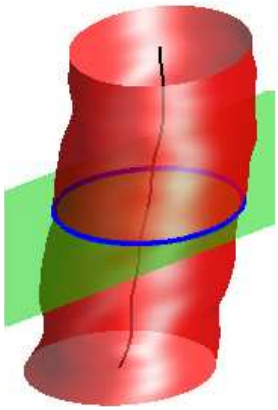

Fig. 6.12: The intersection of a slicing plane (in green) with a 3D surface (in red) is a 3D contour, here represented by the curve in blue.

If $\theta = 0$, the rotation matrix becomes the identity matrix and the direction of the rotation axis has no importance. Otherwise, in our case, $\overrightarrow{u}$ is defined as

$$\overrightarrow{u} = \frac{\overrightarrow{n} \times \overrightarrow{v}}{\| \overrightarrow{n} \times \overrightarrow{v} \|} \tag{6.16}$$

where $\overrightarrow{n} \times \overrightarrow{v}$ is the cross product between vectors $\overrightarrow{n}$ and $\overrightarrow{v}$.

Besides being fast and simple, another advantage of this approach is that the 2D points (x', y'), whose coordinates are computed by equation 6.10, can be directly used to compute some important measures, like lumen or plaque areas at any point of the medial axis of the artery.

Figure 6.12 shows a 3D surface, an arbitrary slicing plane and the sliced contour obtained with the procedure described above.

6.11 Slicing normal to the medial axis of the artery

The analysis of the 3D surfaces reconstructed from the carotid boundaries helps to get a better picture of the plaque distribution along the surface of the artery. It aids to locate points with maximum degree of stenosis and allows the computation of important measures like the area of the lumen or the area of the plaque along the medial axis of the artery. But, to get good estimates of these measures, the

carotid surfaces have to be resliced at planes that are normal to the medial axis of the artery.

The 3D smooth spline curve that links the aligned centroids of the carotid wall is not a very good approximation of the real medial axis. It contains errors both in the location of the axis and in the direction of its tangent vectors. Therefore, this information should not be directly used to define the normal slicing planes, unless the estimation of the medial axis is improved with a proper algorithm. This was the approach followed in [78], where an iterative algorithm was used. At each iteration, the local position, Q, and the tangential direction, $\overrightarrow{e}$, of the medial axis are estimated from the contour points of the current slice. Then, a new slice is obtained a short distance away from point Q and normal to vector $\overrightarrow{e}$. The local direction, $\overrightarrow{e}$, is estimated as the mean of the unit vectors tangential to the wall surface, in the longitudinal direction, at each of the contour points. The mean position of the contour points gives the coordinates of point Q. An important drawback of this algorithm is that the first slicing plane has to be chosen approximately perpendicular to the carotid wall.

We think a better solution is to choose a point of the smooth spline curve that links the centroids and to look for the orientation that minimizes the area inside the contour in the slice that contains the given point. The search may start, for instance, at the orientation of the vector tangent to the spline curve at the chosen point. The initial surface will not, in general, be normal to the medial axis, but the algorithm forces the slicing plane to converge to the normal orientation, where the area is minimal for cylindrical surfaces. The fast Nelder-Mead simplex method [96] was used to solve the minimization problem. Figure 6.13 shows an example with the surface to be sliced, the chosen point of the slicing plane, the initial plane and the plane found by the simplex method.

6.12 3D measures

There are several plaque measures that can be computed using normal reslicing of the reconstructed 3D surfaces of the carotid. Some very interesting examples were proposed in [78], in particular, the cross-sectional area or diameter of the lumen, the volume of the plaque and the percentage stenosis index, S_H, defined as

$$S_H = 100 \times \left(1 - \frac{H_{\text{lumen}}}{H_{\text{ref}}}\right) \tag{6.17}$$

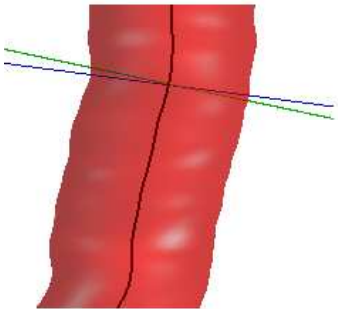

Fig. 6.13: Slicing normal to a 3D surface. The slicing plane has to contain a chosen point of the smooth spline (black curve) that approximates the medial axis. The initial plane is in green and the blue plane gives the minimum area inside the sliced contour.

where H_{lumen} is some measurement of the lumen and H_{ref} is the corresponding reference measurement [78]. As suggested by the authors, these measurements may be either the diameter, the area or the volume. In the case of the area, for instance, H_{lumen} and H_{ref} are the areas inside the lumen and inside the carotid wall, respectively.

The diameter measurements may not be realistic when the lumen is not concentric with the carotid wall. On the other hand, volume quantification gives a single measure, with no information about the spatial distribution of the plaque. Therefore, we did not consider these measurements.

Two very intuitive and informative measures are the plaque area and the stenosis index for the area, computed as functions of the length of the medial axis. These were the measurements adopted in this work.

6.13 Results

Using the proposed algorithms, the carotid wall and lumen surfaces were reconstructed from the contours automatically segmented from two different 3D volumes. The reconstructed surfaces are presented in Fig. 6.14 and Fig. 6.15, respectively. For comparison, we also include, for each case, the surface obtained from a manual segmentation of the same 3D volumes.

Plots of the area inside the carotid wall, the area inside the lumen and the plaque area, as functions of the distance along the longitudinal direction, are given in Fig. 6.16, Fig. 6.17 and Fig. 6.18, respectively. Similar plots of the area percentage

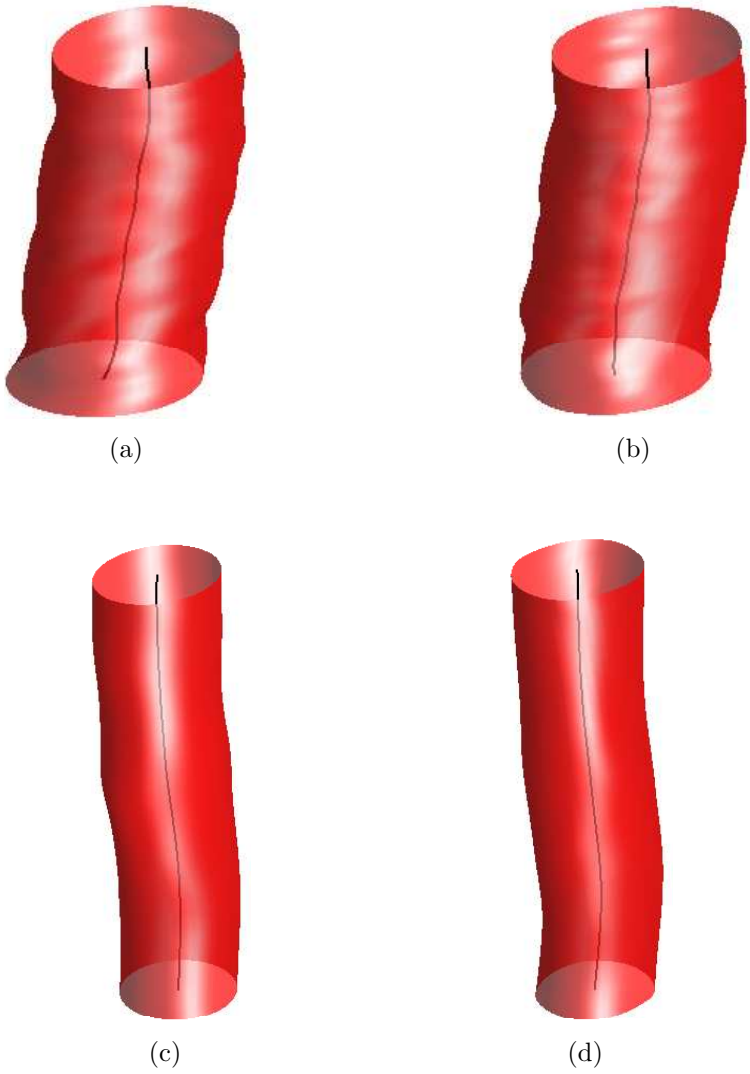

Fig. 6.14: Reconstructed wall surfaces: a) Surface A, with automatic segmentation; b) Surface A, with manual segmentation; c) Surface B, with automatic segmentation; d) Surface B, with manual segmentation.

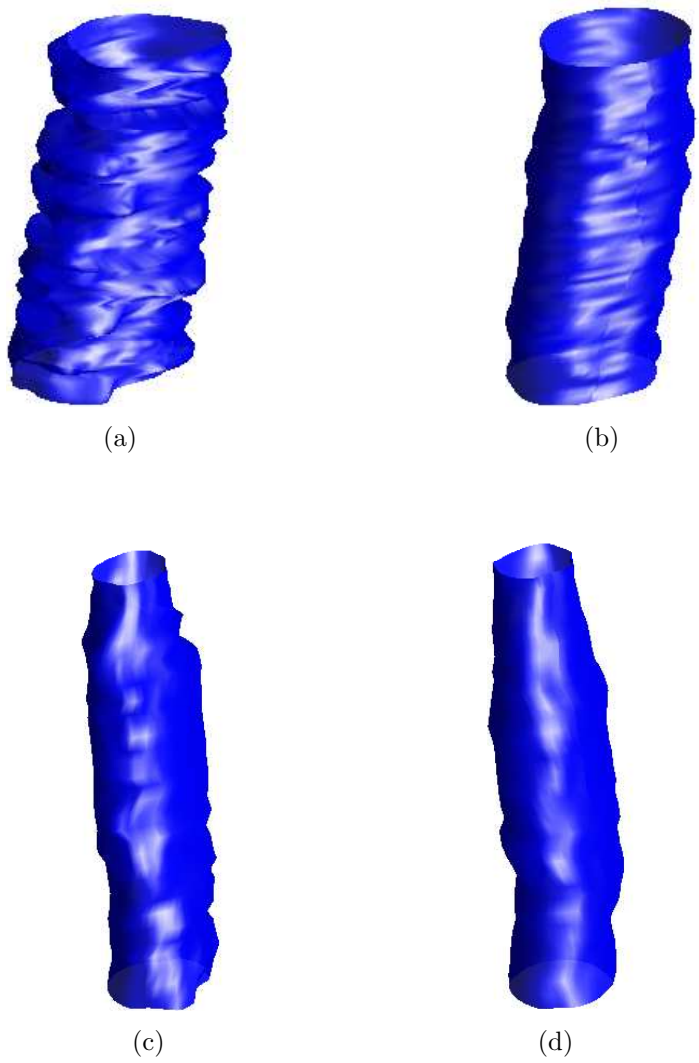

(a) (b)

(c) (d)

Fig. 6.15: Reconstructed lumen surfaces: a) Surface A, with automatic segmentation; b) Surface A, with manual segmentation; c) Surface B, with automatic segmentation; d) Surface B, with manual segmentation.

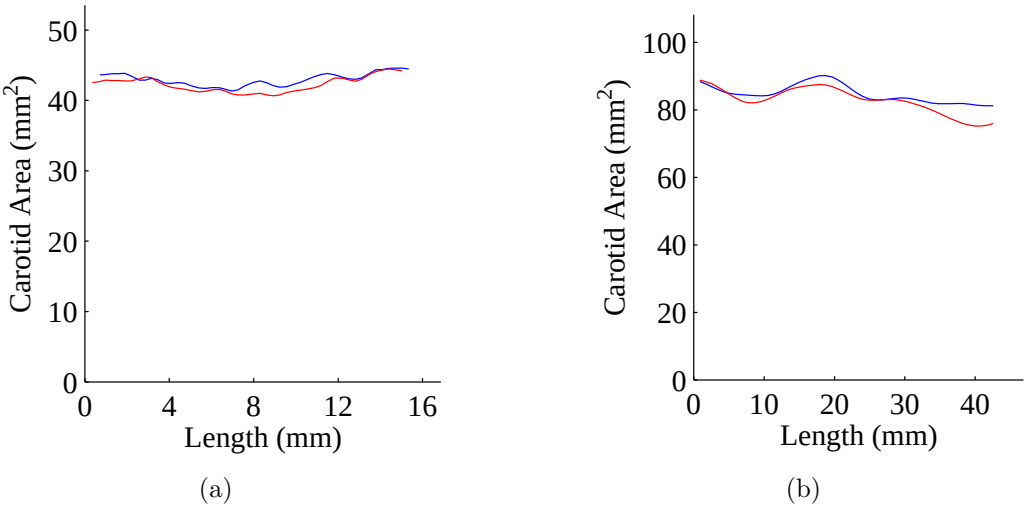

Fig. 6.16: Area inside the carotid wall, along the medial axis: a) For surface A, with automatic (blue) and manual (red) segmentation; b) For surface B, with automatic (blue) and manual (red) segmentation.

stenosis index can be found in Fig. 6.19.

Finally, Fig. 6.20 and Fig. 6.21 present the relative area error, A_{err}, defined in section 4.9, for the carotid wall and lumen surfaces obtained from the automatic segmentations. The surfaces obtained from the manual segmentations were used as the ground truth.

6.14 Concluding remarks

The results presented in the previous section show that the algorithm proposed for the carotid wall segmentation gives good estimates of the CCA wall surfaces. Nevertheless, occasionally, some correction may be required from the expert.

The same conclusion cannot be taken for the lumen boundary. The main cause for the large and frequent errors in the lumen segmentation is the severe hypoechogenicity of the plaque in the exams. We remark that the manual segmentation in these cases are usually supported by some parts of the lumen boundary that are still perceivable, the rest of the curve being inferred as a smooth continuation of these visible edges. It seems the user projects over the image a mental smooth geometrical model that best fits the boundary cues that are visible. However, to correctly locate these boundaries, even a specialist often needs to add the information obtained through a power-Doppler image. More studies and new techniques

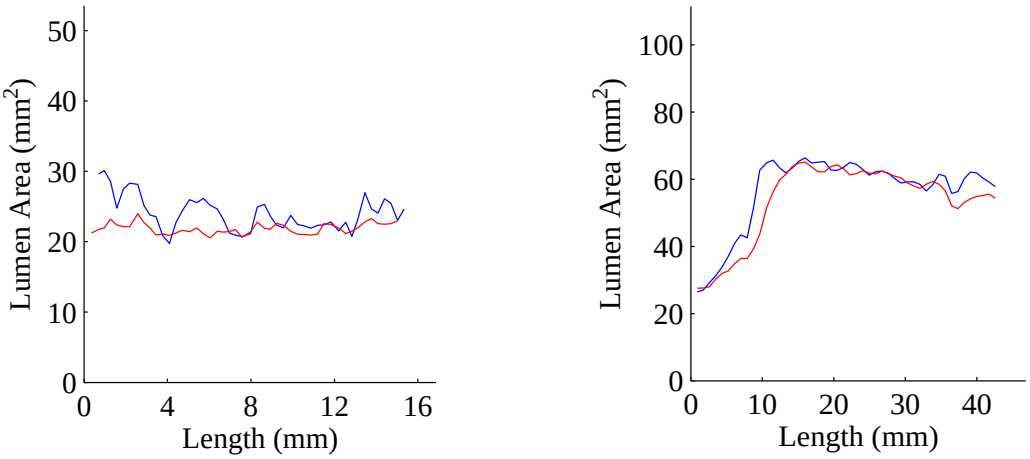

(a) (b)

Fig. 6.17: Lumen area along the medial axis: a) For surface A, with automatic (blue) and manual (red) segmentation; b) For surface B, with automatic (blue) and manual (red) segmentation.

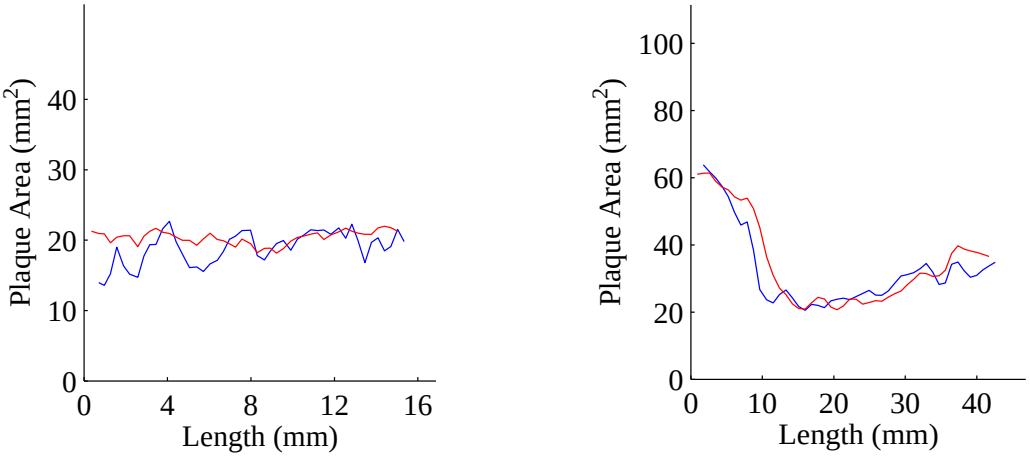

(a) (b)

Fig. 6.18: Plaque area along the medial axis: a) For surface A, with automatic (blue) and manual (red) segmentation; b) For surface B, with automatic (blue) and manual (red) segmentation.

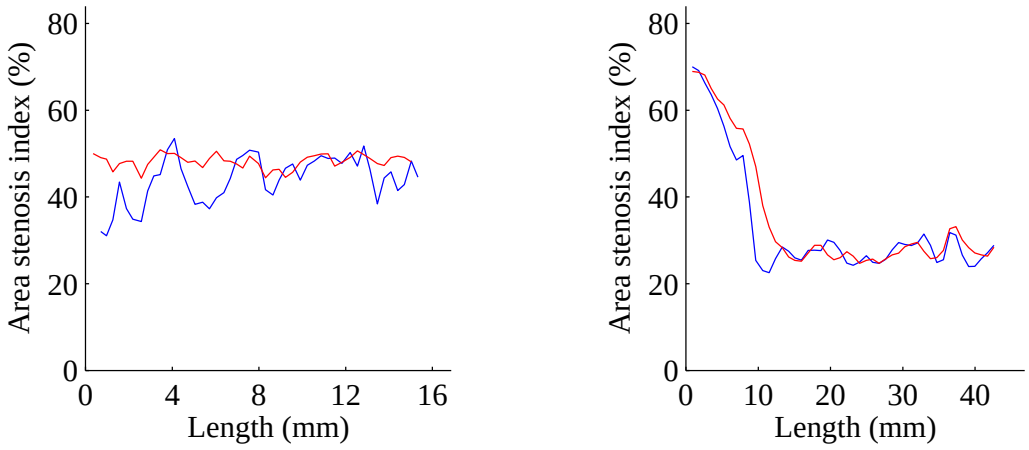

Fig. 6.19: Area stenosis index along the medial axis: a) For surface A, with automatic (blue) and manual (red) segmentation; b) For surface B, with automatic (blue) and manual (red) segmentation.

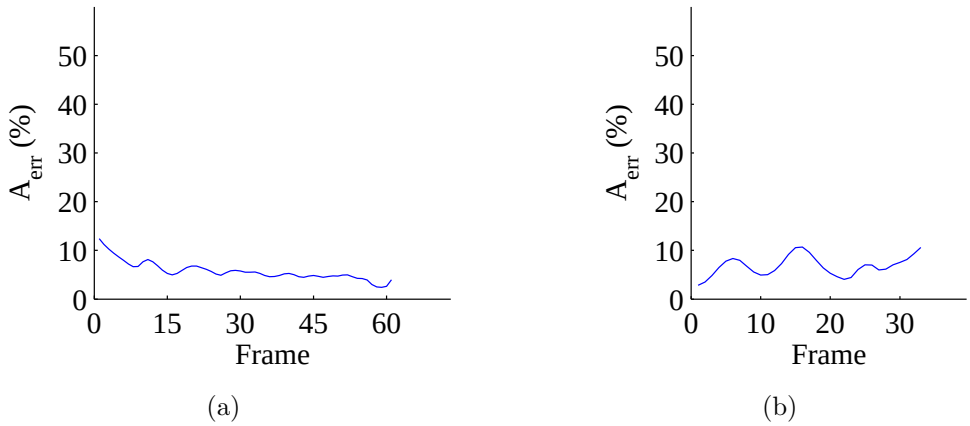

Fig. 6.20: Relative area error for the carotid wall in each frame: a) For surface A; b) For surface B.

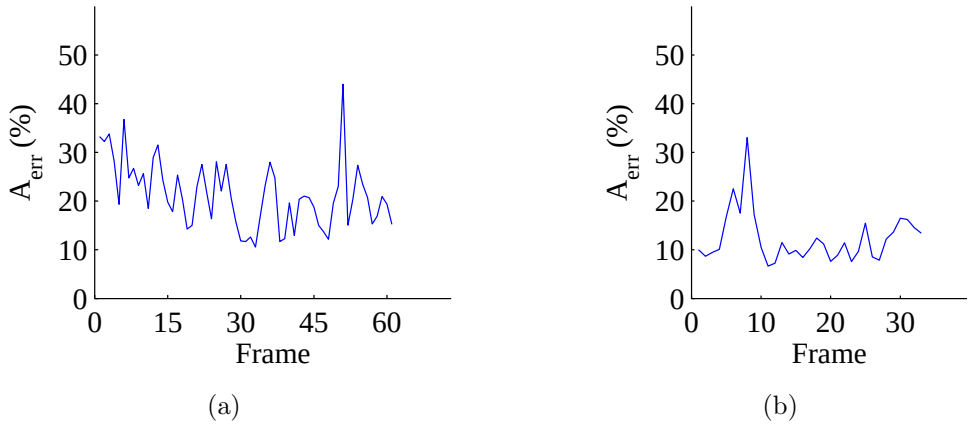

Fig. 6.21: Relative area error for the carotid lumen in each frame: a) For surface A; b) For surface B.

may bring some improvement on the automatic lumen detection in B-mode images, but we believe a sufficiently reliable automatic algorithm should integrate the power-Doppler information as well.

The smoothing of the 3D surfaces after their reconstruction is another problem with the followed approach. We probably get smoother surfaces by simultaneously smoothing and segmenting the whole 3D volume surface, but that does not mean they are more precise. The results confirm that the followed approach is a reasonable solution, as long as the segmentation in each frame is successful, which makes this technique attractive, considering it has several great advantages, like the familiarity of the medical doctor with 2D slices and the savings in computer memory and computational effort.

Chapter 7

CONCLUSIONS AND FUTURE RESEARCH

A complete new approach was presented for the automatic detection of the common carotid wall boundary, in B-mode images. The algorithm is based on a RANSAC search of the best fit of a contour prior in the carotid image. It includes global constraints, making it more powerful and robust to noise than other published approaches that use local constraints. A new non-linear smoothing filter for ultrasound images was also proposed. This filter combines the ICOV edge detector with the local intensity curvature, producing better preservation of important edges than previously published filters.

An ICOV-based dynamic programming model was conceived for the detection of the lumen boundary in longitudinal sections of the carotid, as well as its adaptation to transversal sections, where the boundary is a closed curve. The dynamic programming approach was complemented with a new hybrid geometric active contour, which uses a smooth thresholding surface and the image intensity topology to: reduce some errors left by the dynamic programming segmentation; guide the smoothing of the detected boundary.

The performance of the proposed segmentation algorithms was evaluated in a large set of clinical B-mode images and compared to the manual tracings done by an expert.

The algorithm conceived for the segmentation of the carotid wall proved to be reliable in sections of the CCA. It can also detect the carotid wall in images that include the carotid bulb and parts of the ICA, although, here, the success rate decreases due to the higher complexity of the anatomy. Anyway, it seems some additional information is missing in the segmentation model to avoid perturbations caused by strong nearby tissue boundaries that do not belong to the carotid. These constraints should, probably, be of anatomical and contextual nature. It isn't clear,

however, which information to include and how to do it in an efficient manner. This is an interesting and challenging subject for future studies.

The stiffness of the wall contour prior is a nice way to deal with heavy noise and large wall gaps, but it also limits the ability of the prior to stick to the real boundary at more irregular sections or when the shape of the real boundary deviates too much from the prior model. Fortunately, the last situation is not frequent and the errors involved are normally small. In any case, this limitation could be reduced with a local refinement of the detected wall (e.g., with a ICOV-based active contour), although, perhaps, at the expense of increasing the segmentation errors at regions where the wall boundary is hardly visible or invisible. A more ambitious approach would be to allow some sort of local geometric deformation of the contour prior. But a practical implementation of this idea may not be compatible with the RANSAC search. Due to all the specific difficulties of the carotid segmentation in B-scans, the best segmentation approach is, perhaps, the registration of some sort of discriminating image features with an atlas of the artery. This is probably the way medical experts locate the boundaries of the artery in these images.

The results in the segmentation of the lumen boundary were not so good. There are two main reasons for this. First, the possible presence of carotid plaques hinders the introduction of a geometric prior of the lumen shape. Second, the hypoechogenicity of most plaques often compromises their correct separation from the lumen region. In this case, medical experts often need to analyze multiple B-scans and color-coded duplex sonography to improve the detection. On the other hand, the geometry of some plaque boundaries cannot be correctly detected by the considered dynamic programming algorithms, which are also not particularly suited to the closed contours found in transversal sections of the carotid. Besides, a polar segmentation scheme has always some dependence on the chosen seed point. Therefore, a region-based segmentation of the lumen would be the ideal solution. But its viability depends on the existence of B-mode image features that reliably discriminate the lumen region from the plaque tissues and that can be used for segmentation. Unfortunately, such features do not seem to exist. Perhaps, the power-Doppler mode images could be used as a complementary information to region-based segmentation. Here is another interesting topic for future research.

New approaches were also proposed for the automatic reconstruction of 3D surfaces from the carotid boundaries, previously segmented in a sequence of B-mode images acquired with a 3D ultrasound system. A level set algorithm was introduced for the computation of new slices directly from the reconstructed 3D surfaces.

Finally, to obtain reliable estimates of surface slices normal to the carotid longitudinal axis, a cross sectional area minimization approach was conceived. Examples of 3D surfaces automatically reconstructed from sequences of B-scans, by the introduced methods, were presented and compared to the surfaces obtained from manual segmentations. Some clinically relevant measures were computed from the reconstructed carotid surfaces.

The obtained results show that it is possible to compute good smooth 3D surfaces directly from the carotid boundaries previously segmented in a set of 2D B-scans, acquired with a freehand system. The proposed solution is very fast but is not directly applicable to bifurcations of the carotid. One possibility for future work would be to adapt our algorithm to deal with the bifurcation. More powerful alternatives, like the radial basis functions [110], are much heavier and more complex. But it would be interesting to explore them as well.

Appendix A

ELLIPSE NORMAL

A conic section can be implicitly described as the zero level set of the following function [95]

$$F(x, y) = ax^2 + bxy + cy^2 + dx + ey + f \tag{A.1}$$

where the values of the parameters a, b, c, d, e and f determine if the conic is an ellipse ($b^2 - 4ac < 0$), a parabola ($b^2 - 4ac = 0$) or a hyperbola ($b^2 - 4ac > 0$).

If $b^2 - 4ac < 0$, then $ac > 0$, so a and c cannot be zero and must have the same sign. Therefore, if $a = 1$, c is positive, as well as $\partial^2 F/\partial x^2 = 2a$ and $\partial^2 F/\partial y^2 = 2c$. Finally, $(\partial^2 F/\partial x^2)(\partial^2 F/\partial y^2) - (\partial^2 F/\partial x \partial y)^2 = 4ac - b^2 > 0$, which means $F(x, y)$ is concave [111] and its gradient points outwards the zero level set.

Appendix B

RANSAC PROOF

If we take $\omega = \omega_p$, the minimum number of samples of n points is given by

$$k_p = \left(1 + N\sqrt{1 - \omega_p^n}\right) / \omega_p^n \tag{B.1}$$

where ω_p^n is the probability of a good sample of n points. To simplify, let us assume the number of edge points for each line segment is a constant, m. In this case, P('good point'/'good line segment') $= 1/m$. If P('good line segment') $= \alpha$, then $\omega_p^n = (\alpha/m)^n$ and we may write

$$k_p = \left(1 + N\sqrt{1 - (\alpha/m)^n}\right) / (\alpha/m)^n \tag{B.2}$$

On the other hand, if we take $\omega = \alpha$, the minimum number of samples of n line segments is

$$k_s^* = \left(1 + N\sqrt{1 - \alpha^n}\right) / \alpha^n \tag{B.3}$$

and we have to evaluate m^n samples of n points for each sample of n line segments. Therefore, in this case, the minimum number of samples of n points will be

$$k_s = m^n \left(1 + N\sqrt{1 - \alpha^n}\right) / \alpha^n \tag{B.4}$$

It is easy to show that for $m > 1$ we always have $k_s < k_p$. Therefore, it is more efficient to set $\omega = P$('good line segment') and to evaluate all combinations of n edge points for each sample of n line segments.

Appendix C

PLANE AND NORMAL LINE

The general equation of the plane passing through point $P_0 = (x_0, y_0, z_0)$ and normal to the vector $\overrightarrow{n} = (a, b, c)$ is

$$ax + by + cz + d = 0 \tag{C.1}$$

with $d = -(ax_0 + by_0 + cz_0)$.

The line passing through the origin of the $x - y - z$ reference frame and normal to the plane described above can be written in a parametric form as

$$(x, y, z) = \lambda(a, b, c) \tag{C.2}$$

with $\lambda \in \mathbb{R}$.

The intersection, Q, of this line with the above plane can be obtained by substituting $x = \lambda a$, $y = \lambda b$ and $z = \lambda c$ in the general equation of the plane, giving

$$\left(a^2 + b^2 + c^2\right)\lambda + d = 0 \iff \lambda = -\frac{d}{\|\overrightarrow{n}\|^2} \tag{C.3}$$

which means

$$Q = \lambda\overrightarrow{n} = -\frac{d}{\|\overrightarrow{n}\|^2}\overrightarrow{n}. \tag{C.4}$$

Appendix D

NUMERICAL SCHEME FOR THE IMAGE FILTER

The following partial differential equation

$$\frac{\partial I(x,y;t)}{\partial t} = c(x,y;t)\kappa(x,y;t)\|\nabla I(x,y;t)\| \tag{D.1}$$

can be rewritten as

$$I_t = c\|\nabla I\|\nabla\cdot\left(\frac{\nabla I}{\|\nabla I\|}\right) \tag{D.2}$$

which is equivalent to

$$I_t = c\frac{I_x^2 I_{yy} - 2I_x I_y I_{xy} + I_y^2 I_{xx}}{I_x^2 + I_y^2} \tag{D.3}$$

Denoting the time step by Δt and the image grid size by h, the last equation can be discretized with the following explicit numerical scheme [85]

$$\frac{I_{i,j}^{n+1} - I_{i,j}^n}{\Delta t} = c_{i,j}^n \frac{(D_x I_{i,j}^n)^2 D_{yy} I_{i,j}^n - 2D_x I_{i,j}^n D_y I_{i,j}^n D_{xy} I_{i,j}^n + (D_y I_{i,j}^n)^2 D_{xx} I_{i,j}^n}{(D_x I_{i,j}^n)^2 + (D_y I_{i,j}^n)^2} \tag{D.4}$$

where

$$\begin{aligned}
D_x I_{i,j}^n &= \frac{I_{i+1,j}^n - I_{i-1,j}^n}{2h} \\
D_y I_{i,j}^n &= \frac{I_{i,j+1}^n - I_{i,j-1}^n}{2h} \\
D_{xx} I_{i,j}^n &= \frac{I_{i+1,j}^n - 2I_{i,j}^n + I_{i-1,j}^n}{h^2} \\
D_{yy} I_{i,j}^n &= \frac{I_{i,j+1}^n - 2I_{i,j}^n + I_{i,j-1}^n}{h^2} \\
D_{xy} I_{i,j}^n &= \frac{I_{i+1,j+1}^n - I_{i-1,j+1}^n - I_{i+1,j-1}^n + I_{i-1,j-1}^n}{4h^2}
\end{aligned}$$

Appendix E

NUMERICAL SCHEME FOR THE CHAN-VESE ACTIVE CONTOUR

The Chan-Vese two-phase piecewise constant active contour [97] is described by the following Euler-Lagrange equation

$$\frac{\partial \phi}{\partial t} = \delta_\epsilon(\phi)\left[\mu \mathrm{div}\left(\frac{\nabla \phi}{|\nabla \phi|}\right) - \lambda_1(u_0 - c_1)^2 + \lambda_2(u_0 - c_2)^2\right] \tag{E.1}$$

Denoting the time step by Δt and the image grid size by $h = \Delta x = \Delta y$, equation E.1 can be discretized with the following semi-implicit numerical scheme [98]

$$\phi_{i,j}^{n+1} = \frac{1}{D}\left(\phi_{i,j}^n + m_2 G_{i,j}^n - m_1 F_{i,j}^n\right) \tag{E.2}$$

where

$$\begin{aligned}
m_1 &= \Delta t\, \delta_\epsilon\left(\phi_{i,j}^n\right) \\
m_2 &= \frac{\mu m_1}{h^2} \\
F_{i,j}^n &= \lambda_1(u_0 - c_1)^2 - \lambda_2(u_0 - c_2)^2 \\
G_{i,j}^n &= D_1\phi_{i+1,j}^n + D_2\phi_{i-1,j}^n + D_3\phi_{i,j+1}^n + D_4\phi_{i,j-1}^n \\
D &= 1 + m_1\left(D_1 + D_2 + D_3 + D_4\right) \\
D_1 &= \left[(D_x^+\phi_{i,j}^n)^2 + (D_y^0\phi_{i,j}^n)^2\right]^{-\frac{1}{2}} \\
D_2 &= \left[(D_x^-\phi_{i,j}^n)^2 + (D_y^0\phi_{i-1,j}^n)^2\right]^{-\frac{1}{2}} \\
D_3 &= \left[(D_x^0\phi_{i,j}^n)^2 + (D_y^+\phi_{i,j}^n)^2\right]^{-\frac{1}{2}} \\
D_4 &= \left[(D_x^0\phi_{i,j-1}^n)^2 + (D_y^-\phi_{i,j}^n)^2\right]^{-\frac{1}{2}}
\end{aligned}$$

$$
\begin{aligned}
D_x^- \phi_{i,j}^n &= \frac{\phi_{i,j}^n - \phi_{i-1,j}^n}{h} \\
D_y^- \phi_{i,j}^n &= \frac{\phi_{i,j}^n - \phi_{i,j-1}^n}{h} \\
D_x^0 \phi_{i,j}^n &= \frac{\phi_{i+1,j}^n - \phi_{i-1,j}^n}{2h} \\
D_y^0 \phi_{i,j}^n &= \frac{\phi_{i,j+1}^n - \phi_{i,j-1}^n}{2h} \\
D_x^+ \phi_{i,j}^n &= \frac{\phi_{i+1,j}^n - \phi_{i,j}^n}{h} \\
D_y^+ \phi_{i,j}^n &= \frac{\phi_{i,j+1}^n - \phi_{i,j}^n}{h}
\end{aligned}
$$

Appendix F

SUCCESSFUL SEGMENTATIONS OF THE CAROTID WALL

Several examples of successful segmentations of the carotid wall are presented, for longitudinal and transversal sections. The manually traced contours (green) and the automatically detected contours (red) are shown for each image.

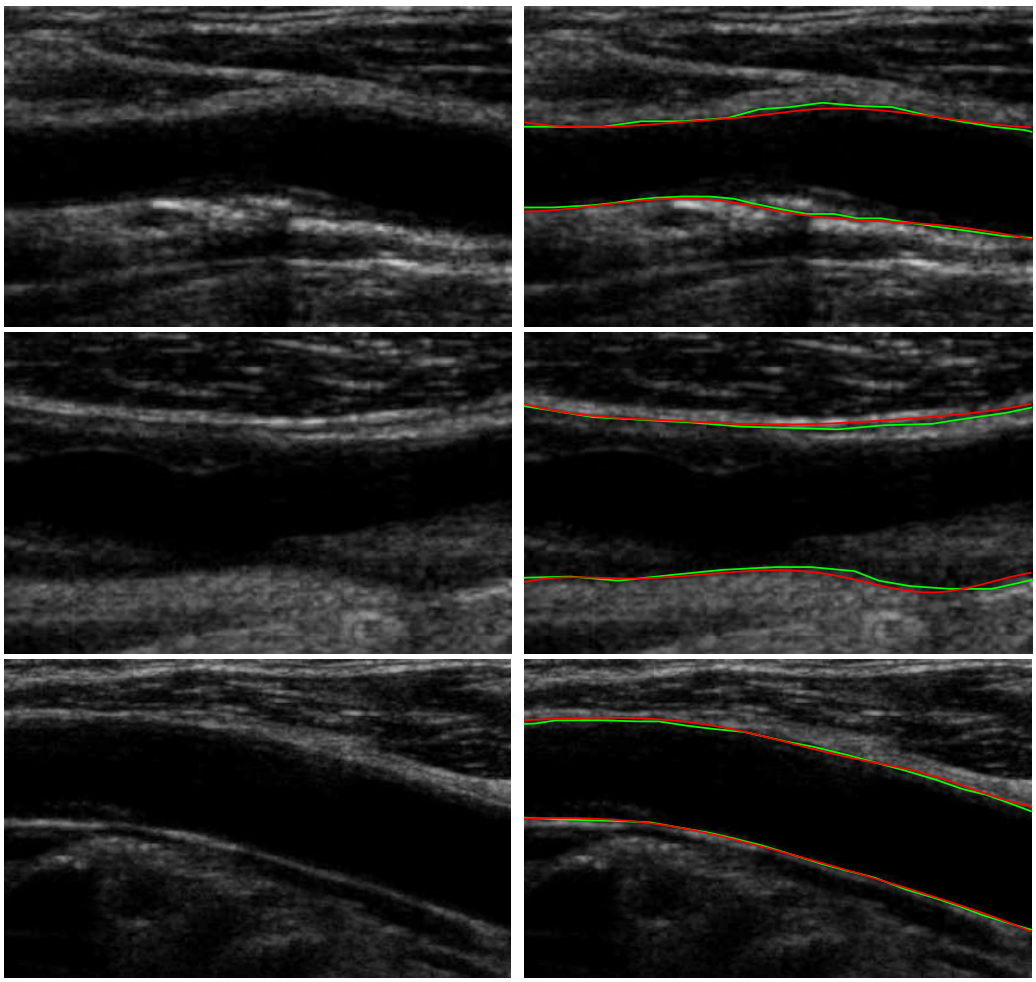

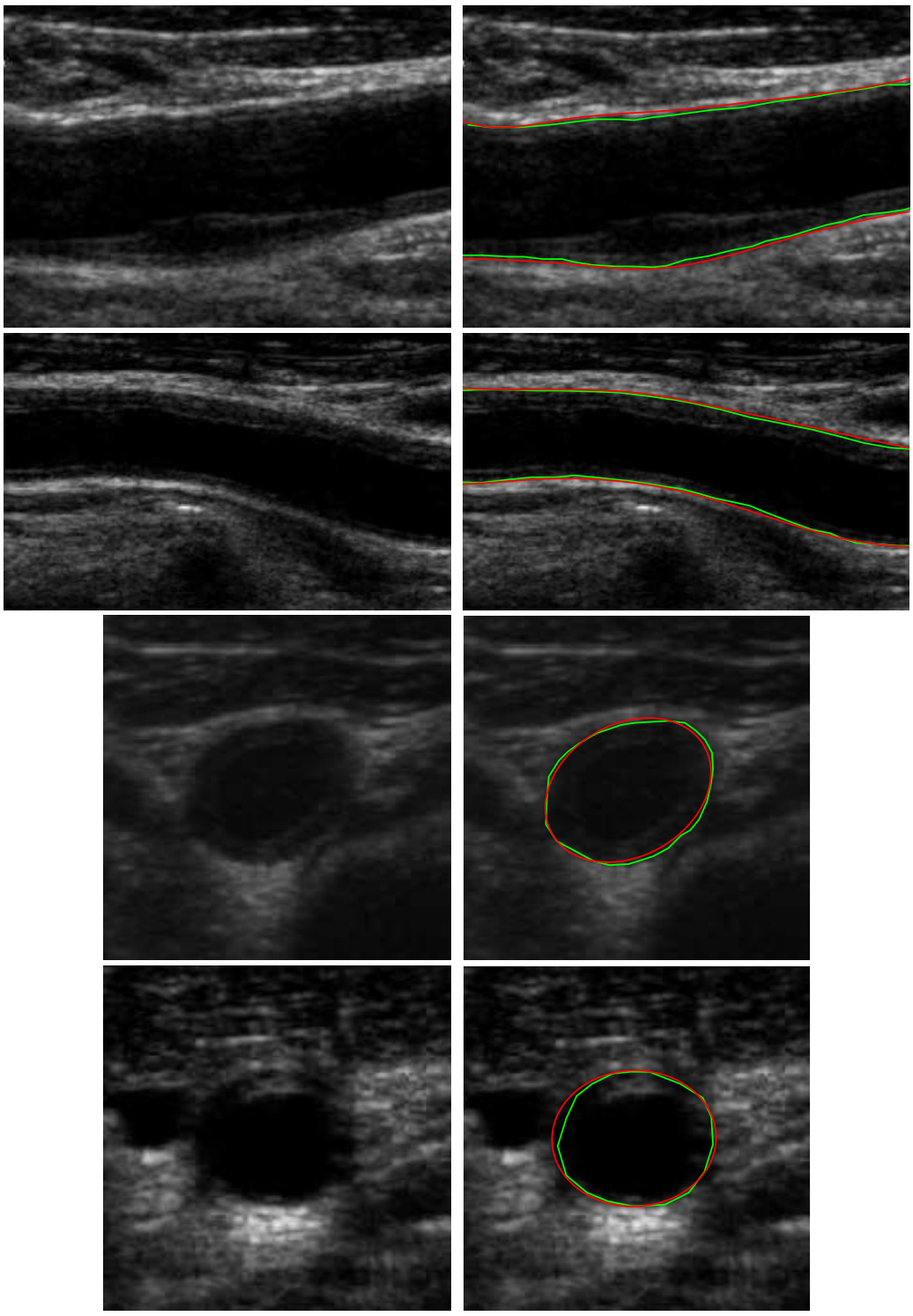

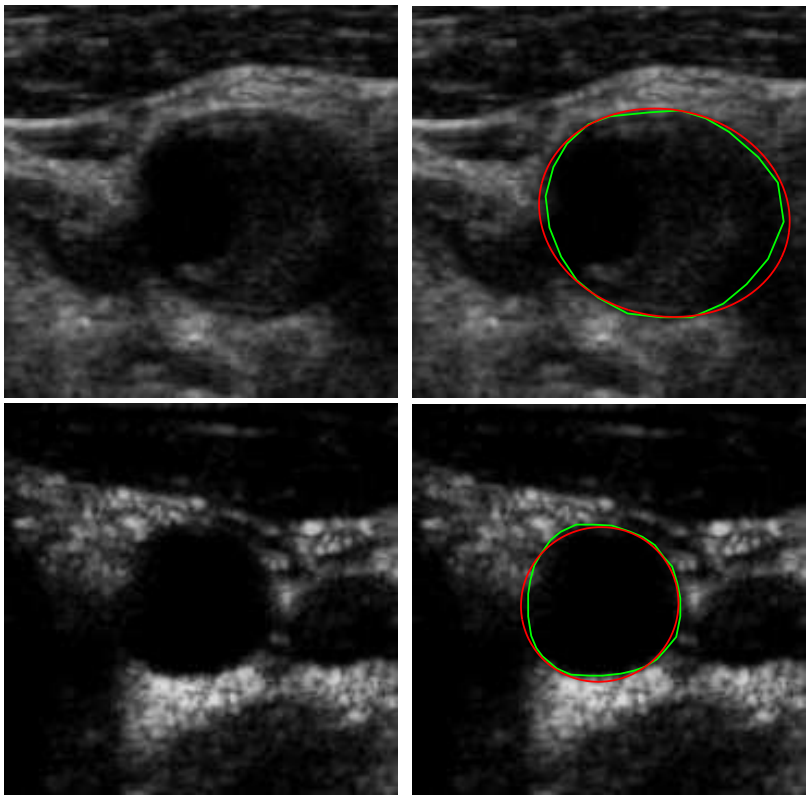

Appendix G

UNSUCCESSFUL SEGMENTATIONS OF THE CAROTID WALL

Several examples of unsuccessful segmentations of the carotid wall are presented, for longitudinal and transversal sections. The manually traced contours (green) and the automatically detected contours (red) are shown for each image.

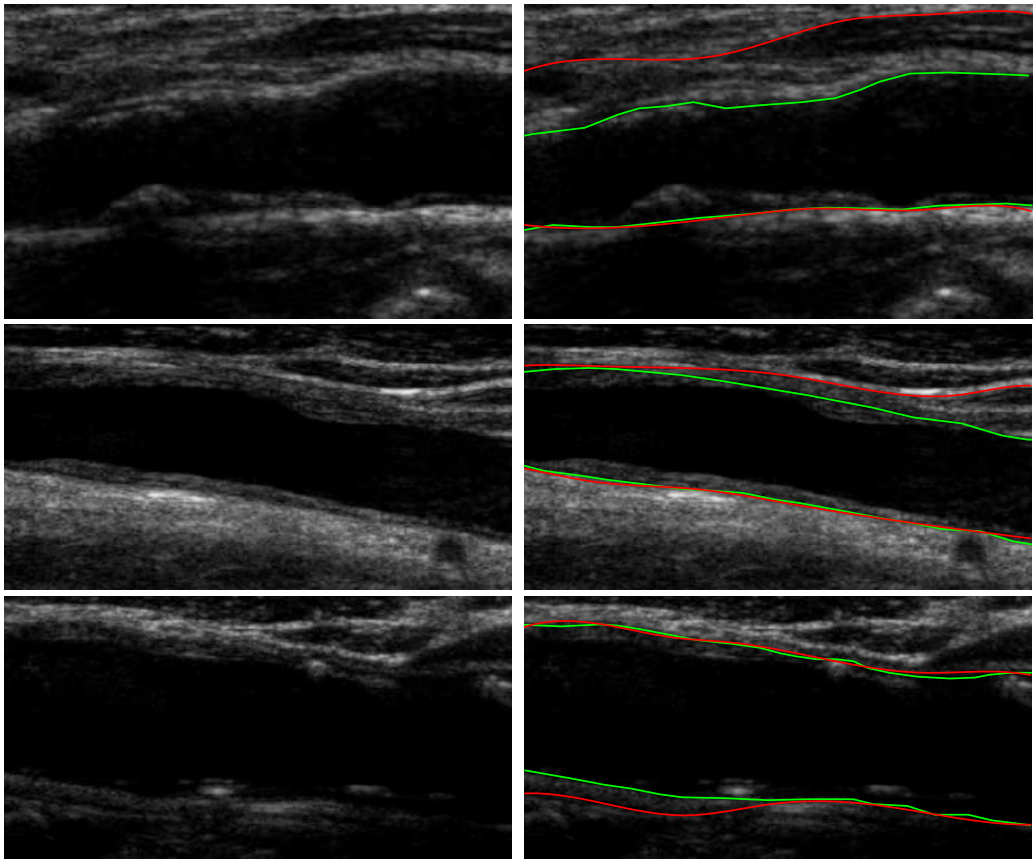

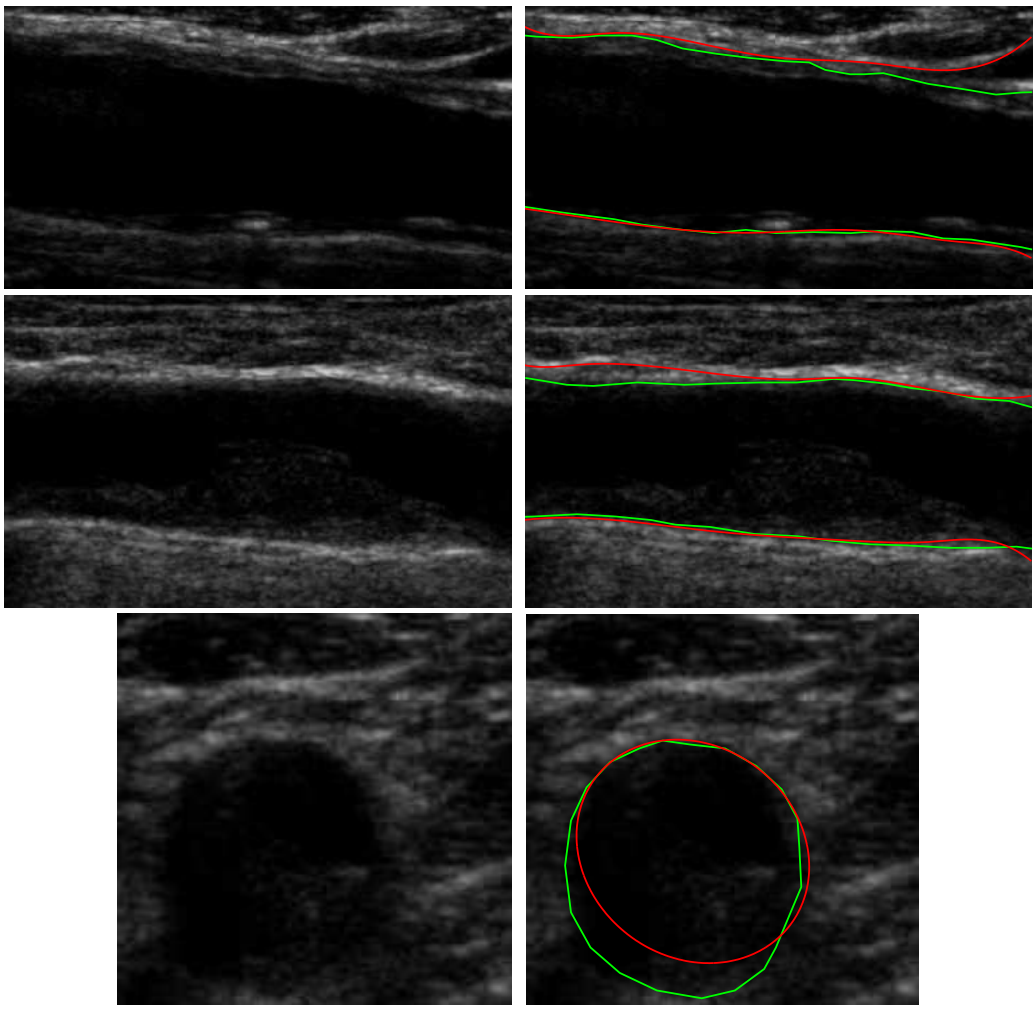

Appendix H

SUCCESSFUL SEGMENTATIONS OF THE CAROTID LUMEN

Several examples of successful segmentations of the carotid lumen are presented, for longitudinal and transversal sections. The manually traced contours (green) and the automatically detected contours (red) are shown for each image.

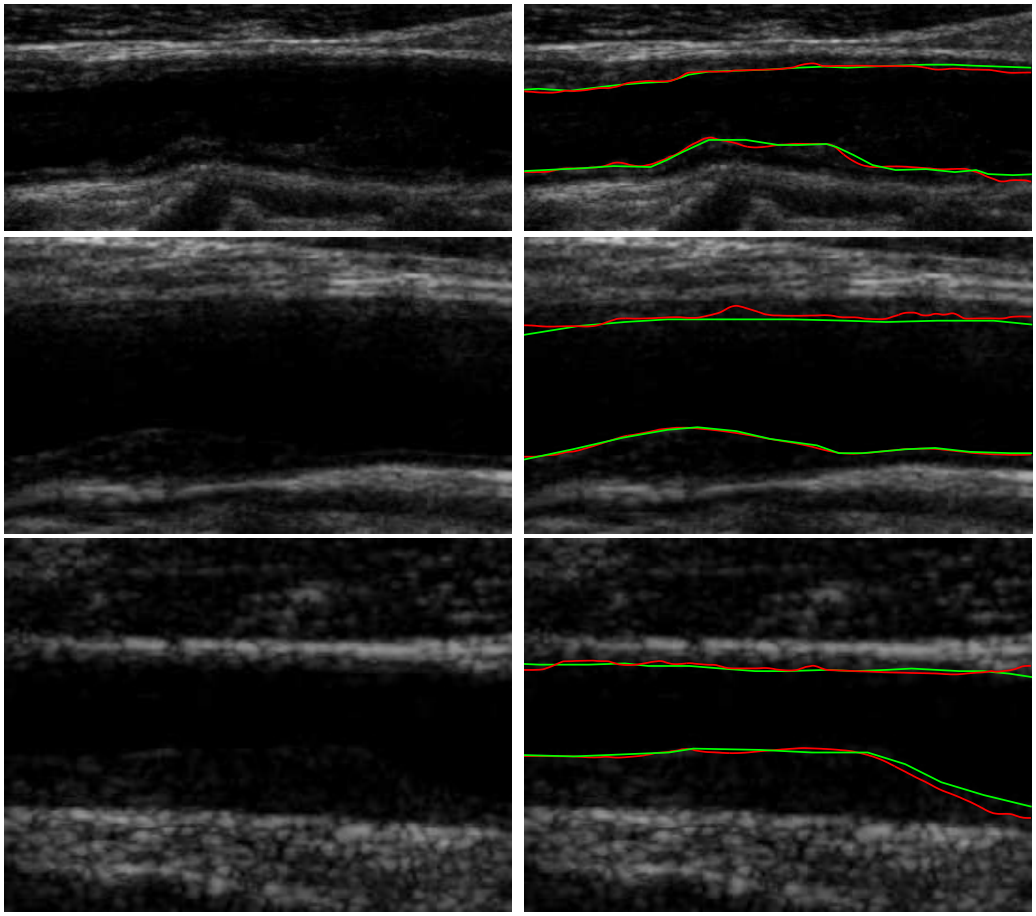

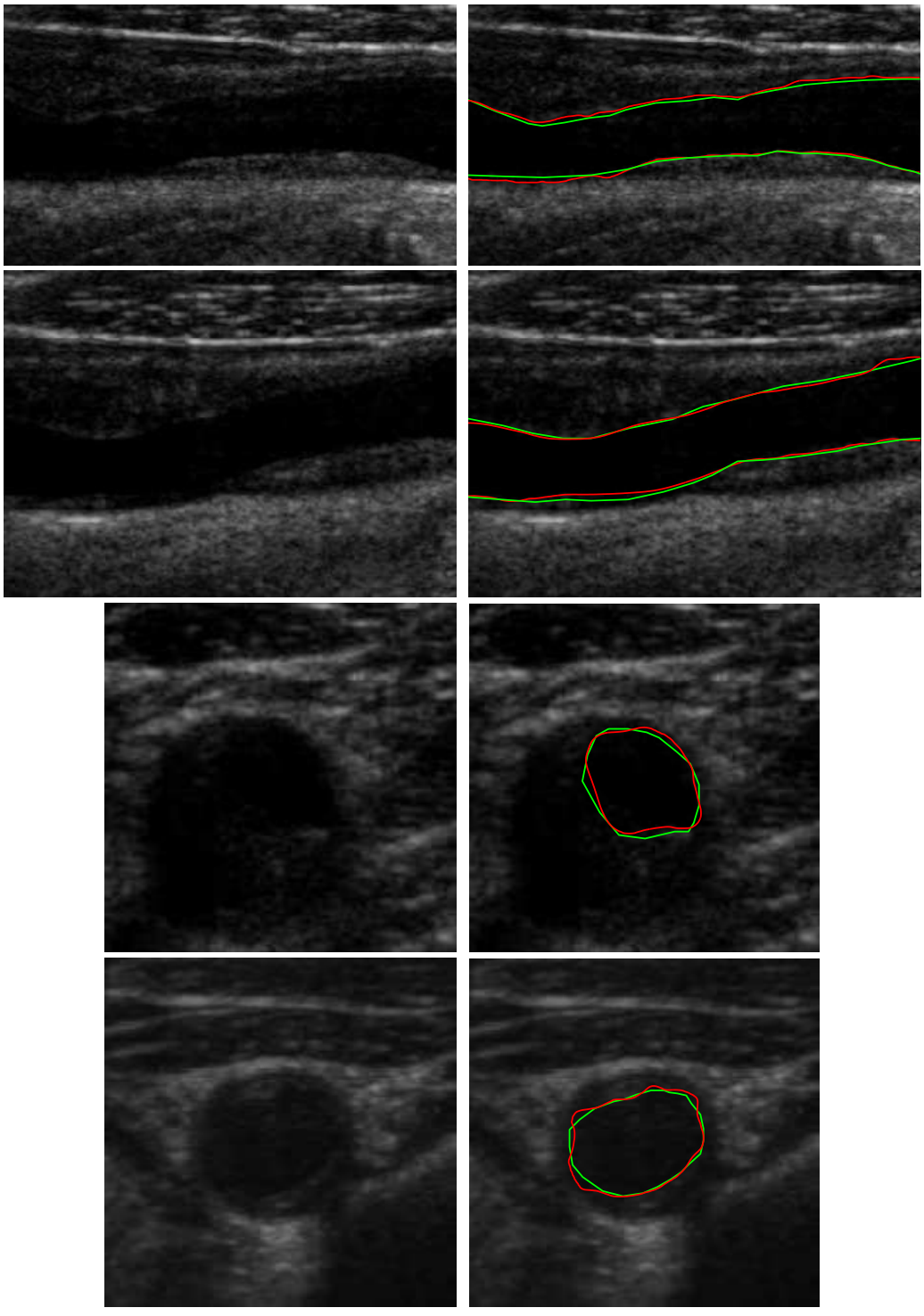

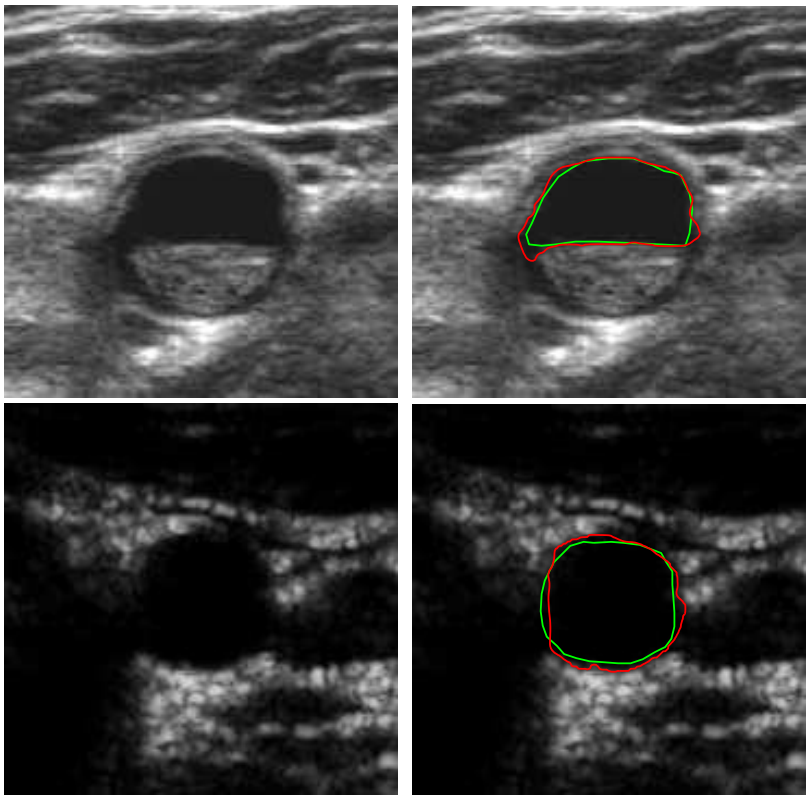

Appendix I

UNSUCCESSFUL SEGMENTATIONS OF THE CAROTID LUMEN

Several examples of unsuccessful segmentations of the carotid lumen are presented, for longitudinal and transversal sections. The manually traced contours (green) and the automatically detected contours (red) are shown for each image.

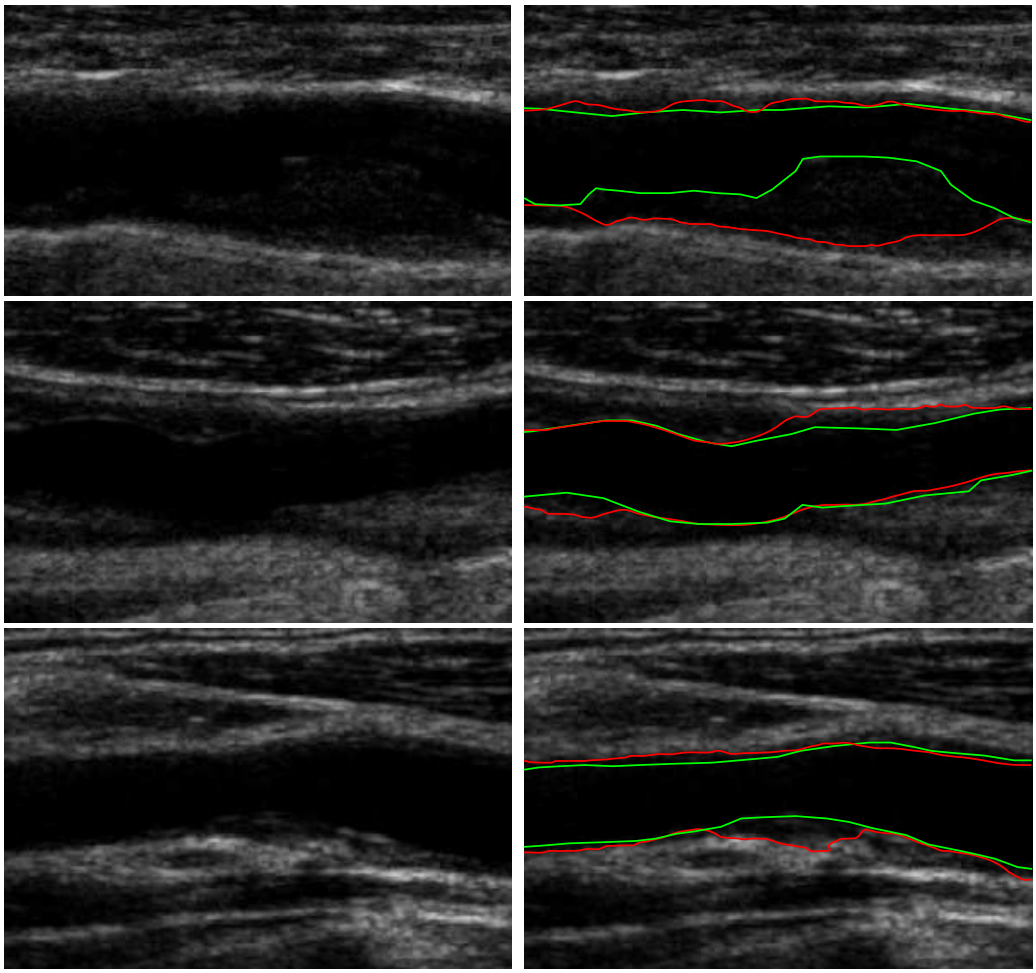

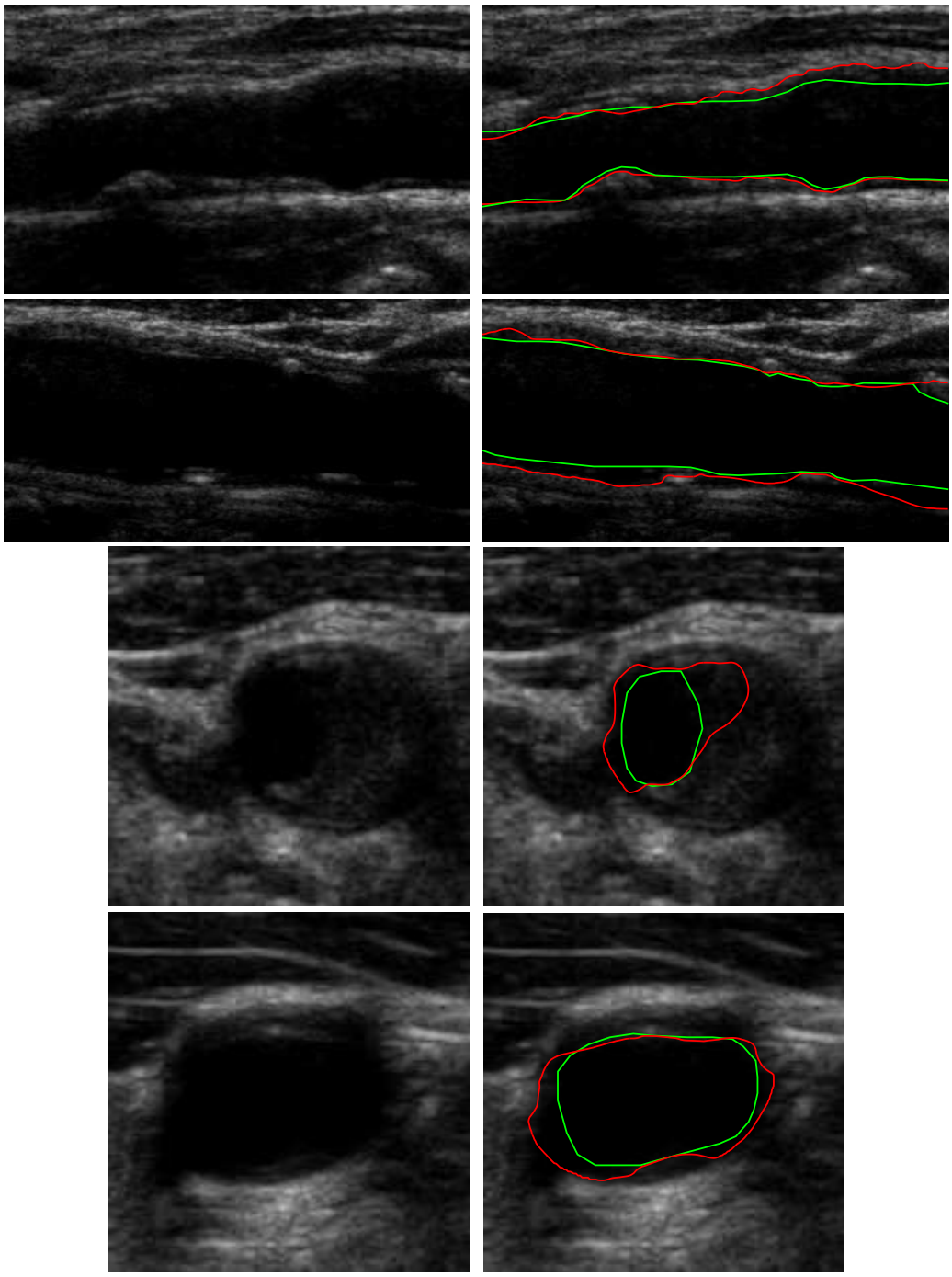

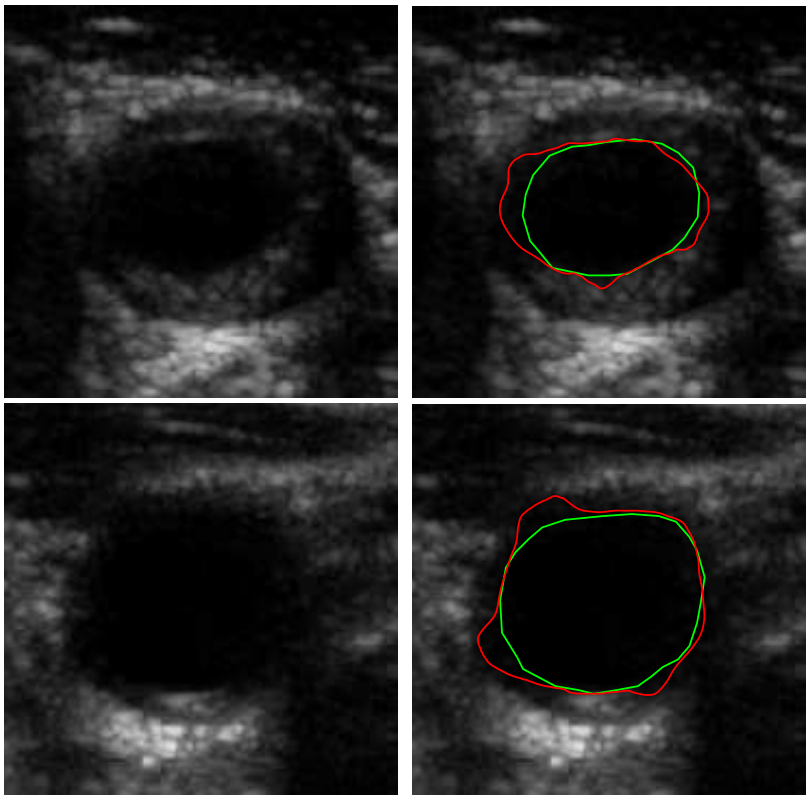

BIBLIOGRAPHY

[1] D. O'Leary, J. Polak, R. Kronmal, T. Manolio, G. Burke, and S. W. Jr., "Carotid-artery intima and media thickness as a risk factor for myocardial infarction and stroke in older adults," *New Engl. J. Med.*, vol. 340, pp. 14–22, 1999.

[2] H. Hodis, W. Mack, L. LaBree, R. Selzer, C. Liu, C. Liu, and S. Azen, "The role of carotid arterial intima-media thickness in predicting clinical coronary events," *Ann. Intern. Med.*, vol. 128, pp. 262–9, February 1998.

[3] P. J. Touboul, P. Prati, P.-Y. Scarabin, V. Adrai, E. Thibout, and P. Ducimetiere, "Use of monitoring software to improve the measurement of carotid wall thickness by B-mode imaging," *J. Hypertension*, vol. 10, no. 5, pp. 37–41, 1992.

[4] J. Gariepy, M. Massonneau, J. Levenson, D. Heudes, A. Simon, and the Groupe de Prevention Cardio-vasculaire en Medecine du Travail, "Evidence for in vivo carotid and femoral wall thickness in human hypertension," *J. Hypertension*, vol. 22, no. 1, pp. 111–118, 1993.

[5] R. H. Selzer, H. N. Hodis, H. Kwong-Fu, W. J. Mack, P. L. Lee, C. R. Liu, and C. H. Liu, "Evaluation of computerized edge tracking for quantifying intima-media thickness of the common carotid artery from B-mode ultrasound images," *Atherosclerosis*, vol. 111, pp. 1–11, 1994.

[6] T. Gustavsson, Q. Liang, I. Wendelhag, and J. Wikstrand, "A dynamic programming procedure for automated ultrasonic measurement of the carotid artery," *Computers in Cardiology*, pp. 297–300, 1994.

[7] R. J. Kozick, "Detecting interfaces on ultrasound images of the carotid artery by dynamic programming," *SPIE*, vol. 2666, pp. 233–241, 1996.

[8] Q. Liang, I. Wendelhag, J. Wikstrand, and T. Gustavsson, "A multiscale dynamic programming procedure for boundary detection in ultrasound artery images," *IEEE Trans. Med. Imag.*, vol. 19, no. 2, pp. 127–142, 2000.

[9] A. Schmidt-Trucksass, D. Cheng, M. Sandrock, J. Schulte-Monting, R. Rauramaa, M. Huonker, and H. Burkhardt, "Computerized analysing system using the active contour in ultrasound measurement of carotid artery intima-media thickness," *Clinical Physiology*, vol. 5, pp. 561–569, 2001.

[10] D. Cheng, A. Schmidt-Trucksass, K. Cheng, M. Sandrock, Q. Pu, and H. Burkhardt, "Automatic detection of the intimal and the adventitial layers of the common carotid artery wall in ultrasound B-mode images using snakes," in *International Conference on Image Analysis and Processing*, pp. 452–457, B. Werner, 1999.

[11] D. Cheng, A. Schmidt-Trucksass, K. Cheng, and H. Burkhardt, "Using snakes to detect the intimal and adventitial layers of the common carotid artery wall in sonographic images," *Computer Methods and Programs in Biomedicine*, vol. 67, pp. 27–37, 2002.

[12] A. Gee, R. Prager, G. Treece, and L. Berman, "Engineering a freehand 3D ultrasound system," *Pattern Recogn. Lett.*, vol. 24, no. 4-5, pp. 757–777, 2003.

[13] R. Rocha, A. Campilho, and J. Silva, "Segmentation of ultrasonic images of the carotid," in *Int. Conf. Image Analysis and Recognition (ICIAR'2005), Toronto, Canada*, vol. 3656, pp. 949–957, Springer LNCS, September 2005.

[14] E. Bartels, *Color-coded Duplex Ultrasonography of the Cerebral Vessels*. F.K.Schattauer,Germany, 1998.

[15] J. M. Thijssen, "Ultrasonic speckle formation, analysis and processing applied to tissue characterization," *Pattern Recogn. Lett.*, vol. 24, no. 4-5, pp. 659–675, 2003.

[16] J. A. Noble and D. Boukerroui, "Ultrasound image segmentation: a survey," *IEEE Trans. Med. Imag.*, vol. 25, no. 8, pp. 987–1010, 2006.

[17] J. Sanches, *Reconstrução 3D bayesiana a partir de sequências ecográficas*. PhD thesis, Instituto Superior Técnico, Lisboa, Março 2003.

[18] M. Sonka, W. Liang, R. Stefancik, and A. Stolpen, *Handbook of Medical Imaging: Medical Image Processing and Analysis*, vol. 2. SPIE, 2000.

[19] D. Baldassarre, M. Amato, A. Bondioli, C. R. Sirtori, and E. Tremoli, "Carotid artery intima-media thickness measured by ultrasonography in normal clinical practice correlates well with atherosclerosis risk factors," *Stroke*, vol. 31, pp. 2426 – 2430, October 2000.

[20] M. Halenka, "Noninvasive measurement of early atherosclerosis by high-resolution B-mode ultrasonography," *Acta- Universitatis Palackianae Olomucensis Facultatis Medicae*, vol. 142, pp. 7–12, 1999.

[21] S. Osher and J. A. Sethian, "Fronts propagating with curvature-dependent speed: Algorithms based on Hamilton-Jacobi formulations," *Journal of Computational Physics*, vol. 79, pp. 12–49, 1988.

[22] J. A. Sethian, *Level Set Methods and Fast Marching Methods.* Cambridge University Press, 1999.

[23] S. Osher and R. Fedkiw, *Level Set Methods and Dynamic Implicit Surfaces.* Springer-Verlag. New York, 2003.

[24] J. Suri, S. Singh, S. Laxminarayan, X. Zeng, K. Liu, and L. Reden, "Shape recovery algorithms using level sets in 2-D/3-D medical imagery: A state of the art review," *IEEE Trans. Information Technology in Biomedicine*, vol. 6, pp. 8–28, March 2002.

[25] A. Tsai, A. J. Yezzi, W. M. W. III, C. Tempany, D. Tucker, A. Fan, W. E. L. Grimson, and A. S. Willsky, "A shape-based approach to the segmentation of medical imagery using level sets.," *IEEE Trans. Med. Imag.*, vol. 22, no. 2, pp. 137–154, 2003.

[26] D. Cremers, T. Kohlberger, and C. Schnorr, "Nonlinear shape statistics in Mumford-Shah based segmentation," in *Proc. European Conference on Computer Vision (ECCV'2002), Copenhagen*, vol. 2351, pp. 93–108, Springer LNCS, 2002.

[27] D. Cremers, N. Sochen, and C. Schnorr, "Towards recognition-based variational segmentation using shape priors and dynamic labeling," in *Proc. European Conference on Computer Vision (ECCV'2003)*, vol. 2695, pp. 388–400, Springer LNCS, 2003.

[28] D. Cremers, S. Osher, and S. Soatto, "Kernel density estimation and intrinsic alignment for knowledge-driven segmentation: Teaching level sets to walk," *Pattern Recognition*, vol. 3175, pp. 36–44, 2004.

[29] J. G. Bosch, S. C. Mitchell, B. P. F. Lelieveldt, F. Nijland, O. Kamp, M. Sonka, and J. H. C. Reiber, "Automatic segmentation of echocardiographic sequences by active appearence motion models," *IEEE Trans. Med. Imag.*, vol. 21, no. 11, pp. 1374–1383, 2002.

[30] M. Mignotte, J. Meunier, and J. C. Tardif, "Endocardial boundary estimation and tracking in echocardiographic images using deformable template and markov random fields," *Pattern Anal. Appl.*, vol. 4, no. 4, pp. 256–271, 2001.

[31] Y. Chen, H. Tagare, S. Thiruvenkadam, F. Huang, D. Wilson, K. S. Gopinath, R. W. Briggs, and E. A. Geiser, "Using prior shapes in geometric active contours in a variational framework," *Int. J. Comput. Vis.*, vol. 50, no. 3, pp. 315–328, 2002.

[32] Y. Chen, F. Huang, H. D. Tagare, M. Rao, D. Wilson, and E. A. Geiser, "Using prior shape and intensity profile in medical image segmentation," in *IEEE Int. Conf. Comput. Vis.*, vol. 2, pp. 1117–1125, 2003.

[33] S. C. Mitchell, J. G. Bosch, B. P. F. Lelieveldt, R. J. van der Geest, J. H. C. Reiber, and M. Sonka, "3-D active appearance models: segmentation of cardiac MR and ultrasound images," *IEEE Trans. Med. Imag.*, vol. 21, no. 9, pp. 1167–1178, 2002.

[34] L. X. Gong, S. D. Pathak, D. R. Haynor, P. S. Cho, and Y. Kim, "Parametric shape modeling using deformable superellipses for prostate segmentation," *IEEE Trans. Med. Imag.*, vol. 23, no. 3, pp. 340–349, 2004.

[35] D. Shen, Y. Zhan, and C. Davatzikos, "Segmentation of prostate boundaries from ultrasound images using statistical shape model," *IEEE Trans. Med. Imag.*, vol. 22, no. 4, pp. 539–551, 2003.

[36] D. Shen, Z. Lao, J. Zeng, W. Zhang, I. A. Sesterhenn, L. Sun, J. W. Moul, E. H. Herskovits, G. Fichtinger, and C. Davatzikos, "Optimized prostate biopsy via a statistical atlas of cancer spatial distribution," *Med. Image Anal.*, vol. 8, pp. 139–150, 2004.

[37] J. Xie, Y. Jiang, and H. T. Tsui, "Segmentation of kidney from ultrasound images based on texture and shape priors," *IEEE Trans. Med. Imag.*, vol. 24, no. 1, pp. 45–57, 2005.

[38] N. Paragios, M. P. Jolly, M. Taron, and R. Ramaraj, "Active shape models and segmentation of the left ventricle in echocardiography," in *Proc. Int. Conf. Scale Space Theories PDEs Methods Computer Vision*, vol. 3459, pp. 131–142, 2005.

[39] L. Fan, P. Santago, W. Riley, and D. M. Herrington, "An adaptive template-matching method and its application to the boundary detection of brachial artery ultrasound scans," *Ultrasound Med. Biol.*, vol. 27, no. 3, pp. 399–408, 2001.

[40] R. F. Wagner, S. W. Smith, J. M. Sandrik, and H. Lopez, "Statistics of speckle in ultrasound B-scans," *IEEE Trans. Sonics Ultrson.*, vol. 30, no. 3, pp. 156–163, 1983.

[41] C. B. Burckhardt, "Speckle in ultrasound B-scans," *IEEE Trans. Sonics Ultrason.*, vol. 25, no. 1, pp. 1–6, 1978.

[42] M. F. Insana, R. F. Wagner, B. S. Garra, D. G. Brown, and T. H. Shawker, "Analysis of ultrasound image texture via generalized rician statistics," *Opt. Eng.*, vol. 25, no. 6, pp. 743–748, 1986.

[43] P. M. Shankar, J. M. Reid, H. Ortega, C. W. Piccoli, and B. B. Goldberg, "Use of non-Rayleigh statistics for the identification of tumors in ultrasonic B-scans of the breast," *IEEE Trans. Med. Imag.*, vol. 12, no. 4, pp. 687–692, 1993.

[44] E. Jakeman, "K-distributed noise," *J. Opt. A: Pure Appl. Opt.*, vol. 1, pp. 784–789, 1999.

[45] V. Dutt and J. F. Greenleaf, "Ultrasound echo envelope analysis using a homodyned K-distribution signal model," *Ultrason. Imag.*, vol. 16, no. 4, pp. 265–287, 1994.

[46] V. Dutt and J. F. Greenleaf, "Statistics of log-compressed echo envelope," *J. Acoust. Soc. Amer.*, vol. 99, no. 6, pp. 3817–3825, 1996.

[47] L. Clifford, P. Fitzgerald, and D. James, "On the statistical characteristics of log-compressed Rayleigh signals: Theoretical formulation and experimental results," *J. Acoust. Soc. Amer.*, vol. 95, no. 3, pp. 1396–1400, 1994.

[48] A. Achim, A. Bezerianos, and P. Tsakalides, "Novel bayesian multiscale method for speckle removal in medical ultrasound images," *IEEE Trans. Med. Imag.*, vol. 20, no. 8, pp. 772–783, 2001.

[49] S. Gupta, R. C. Chauhan, and S. C. Sexana, "Wavelet-based statistical approach for speckle reduction in medical ultrasound images," *Med. Biol. Eng. Comput.*, vol. 42, pp. 189–192, 2004.

[50] X. Zong, A. F. Laine, and E. A. Geiser, "Speckle reduction and contrast enhancement of echocardiograms via multiscale nonlinear processing," *IEEE Trans. Med. Imag.*, vol. 17, no. 4, pp. 532–540, 1998.

[51] Y. Yu and S. Acton, "Speckle reducing anisotropic diffusion," *IEEE Trans. Image Processing*, vol. 11, no. 11, pp. 1260–1270, 2002.

[52] Y. Yu and S. Acton, "Edge detection in ultrasound imagery using the instantaneous coefficient of variation," *IEEE Trans. Image Processing*, vol. 13, no. 12, pp. 1640–1655, 2004.

[53] C. Tauber, *Filtrage anisotrope robuste et segmentation par B-spline snake: application aux images échographiques.* PhD thesis, Institut National Polytechnique de Toulouse, Toulouse, Février 2005.

[54] K. Z. Abd-Elmoniem, A. B. M. Youssef, and Y. M. Kadah, "Real time speckle reduction and coherence enhancement in ultrasound imaging via non-linear anisotropic diffusion," *IEEE Trans. Biomed. Eng.*, vol. 49, no. 9, pp. 997–1014, 2002.

[55] P. M. Shankar, "A general statistical model for ultrasonic backscattering from tissues," *IEEE Trans. Ultrason. Fer. Freq. Control*, vol. 47, no. 3, pp. 727–736, 2000.

[56] P. M. Shankar, V. A. Dumane, J. M. Reid, V. Genis, T. George, F. Forsberg, C. W. Piccoli, and B. B. Goldberg, "Use of K-distribution for classification of breast masses," *Ultrasound Med. Biol.*, vol. 26, no. 9, pp. 1503–1510, 2000.

[57] L. Clifford, P. Fitzgerald, and D. James, "Non-Rayleigh first order statistics of ultrasonic backscatter from normal myocardium," *Ultrasound Med. Biol.*, vol. 19, no. 6, pp. 487–495, 1993.

[58] P. M. Shankar, "Ultrasonic tissue characterization using a generalized Nakagami model," *IEEE Trans. Ultrason. Fer. Freq. Control*, vol. 48, no. 6, pp. 1716–1720, 2001.

[59] P. M. Shankar, V. A. Dumane, J. M. Reid, V. Genis, F. Forsberg, C. W. Piccoli, and B. B. Goldberg, "Classification of ultrasonic B-mode images of breast masses using Nakagami distribution," *IEEE Trans. Ultrason. Fer. Freq. Control*, vol. 48, no. 2, pp. 569–580, 2001.

[60] P. M. Shankar, V. A. Dumane, T. George, C. W. Piccoli, J. M. Reid, F. Forsberg, and B. B. Goldberg, "Classification of breast masses in ultrasonic B-scans using Nakagami and K-distributions," *Phys. Med. Biol.*, vol. 48, no. 14, pp. 2229–2240, 2003.

[61] P. M. Shankar, "The use of the compound probability density function in ultrasonic tissue characterization," *Phys. Med. Biol.*, vol. 49, pp. 1007–1015, 2004.

[62] J. E. Wilhjelm, M. L. Gronholdt, B. Wiebe, S. K. Jespersen, L. K. Hansen, and H. Sillesen, "Quantitative analysis of ultrasound B-mode images of carotid atherosclerotic plaque: correlation with visual classification and histological examination," *IEEE Trans. Med. Imag.*, vol. 17, pp. 910–922, December 1998.

[63] C. I. Christodoulou, C. S. Pattichis, M. Pantziaris, and A. Nicolaides, "Texture based classification of atherosclerotic carotid plaques.," *IEEE Trans. Med. Imag.*, vol. 22, no. 7, pp. 902–912, 2003.

[64] K. L. Chan, "Ultrasonic tissue characterization using fractal feature," in *IEE Conf. Acoustic Sensing and Imaging*, no. 369, pp. 183–188, 1993.

[65] D. Gabor, "Theory of communication," *J. of the Institute of Electical Engineers*, vol. 93, pp. 429–457, 1946.

[66] J. G. Daugman, "Uncertainty relation for resolution in space, spatial frequency, and orientation optimized by twodimensional visual cortical filter," *J. Opt. Soc. Am. A*, vol. 2, no. 7, pp. 1160–1169, 1985.

[67] J. Canny, "A computational approach to edge detection," *IEEE Trans. Pattern Analysis and Machine Intelligence*, vol. 8, no. 6, pp. 679–698, 1986.

[68] T. Gustavsson, R. Abu-Gharbieh, G. Hamarneh, and Q. Liang, "Implementation and comparison of four different boundary detection algorithms for quantitative ultrasonic measurements of the human carotid artery," *Computers in Cardiology*, pp. 69–72, 1997.

[69] P. Detmer, G. Bashein, and R. Martin, "Matched filter identification of left-ventricle endocardial borders in transesophageal echocardiograms," *IEEE Trans. on Med. Imag.*, vol. 9, no. 4, pp. 396–404, 1990.

[70] M. Kass, A. Witkin, and D. Terzopoulos, "Snakes: Active contour models," *International Journal of Computer Vision*, pp. 321–331, 1988.

[71] A. R. Abdel-Dayem and M. R. El-Sakka, "Carotid artery contour extraction from ultrasound images using multi-resolution analysis and watershed segmentation scheme," in *Graphics, Vision and Image Processing (GVIP'2005), Cairo, Egypt*, December 2005.

[72] A. R. Abdel-Dayem and M. R. El-Sakka, "Carotid artery ultrasound image segmentation using fuzzy region growing," in *Int. Conf. Image Analysis and Recognition (ICIAR'2005), Toronto, Canada*, vol. 3656, pp. 869–878, Springer LNCS, September 2005.

[73] J. D. Gill, H. M. Ladak, D. A. Steinman, and A. Fenster, "Accuracy and variability assessment of a semiautomatic technique for segmentation of the carotid arteries from three-dimensional ultrasound images," *Med. Phys.*, vol. 27, no. 6, pp. 1333–1342, 2000.

[74] A. Zahalka and A. Fenster, "An automated segmentation method for three-dimensional carotid ultrasound images," *Phys. Med. Biol.*, vol. 46, no. 4, pp. 1321–1342, 2001.

[75] C. Baillard, C. Barillot, and P. Bouthemy, "Robust adaptive segmentation of 3D medical images with level sets," tech. rep., IRISA, Campus Universitaire de Beaulieu, France, 2000.

[76] G. Celeux and J. Diebolt, "L'algorithme SEM: un algorithme d'apprentissage probabiliste pour la reconnaissance de mélanges de densités," *Revue de statistiques appliquées*, vol. 34, no. 2, pp. 35–51, 1986.

[77] G. Celeux, D. Chauveau, and J. Diebolt, "On stochastic versions of the em algorithm," tech. rep., IRISA, Campus Universitaire de Beaulieu, France, 1995.

[78] D. Barratt, B. Ariff, K. Humphries, S. Thom, and A. Hughes, "Reconstruction and quantification of the carotid artery bifurcation from 3-D ultrasound images," *IEEE Trans. Med. Imag.*, vol. 23, pp. 567–583, May 2004.

[79] J. C. Seabra, "Reconstrução e diagnóstico 3D ecográfico da lesão aterosclerótica," Master's thesis, Instituto Superior Técnico, Lisboa, 2007.

[80] J. C. Seabra, J. Sanches, L. Pedro, and J. F. Fernandes, "Three-dimensional ultrasonic assessment of atherosclerotic plaques," in *Iberian Conf. Patt. Recognition and Image Analysis (IbPRIA'2007)*, June 2007.

[81] C. Xu and J. L. Prince, "Snakes, shapes, and gradient vector flow," *IEEE Trans. Image Processing*, vol. 7, no. 3, pp. 359–369, 1998.

[82] M. A. Fischler and R. C. Bolles, "Random sample consensus: a paradigm for model fitting with applications to image analysis and automated cartography," *Commun. ACM*, vol. 24, no. 6, pp. 381–395, 1981.

[83] L. Rudin, S. Osher, and E. Fatemi, "Nonlinear total variation based noise removal algorithms," in *Proceedings of the Eleventh Annual International Conference of the Center for Nonlinear Studies on Experimental Mathematics: Computational Issues in Nonlinear Science*, pp. 259–268, Elsevier North-Holland, Inc., 1992.

[84] L. Rudin and S. Osher, "Total variation based image restoration with free local constraints," in *Proceedings of IEEE International Conference on Image Processing (ICIP'94)*, vol. 1, pp. 31–35, 1994.

[85] A. Marquina and S. Osher, "Explicit algorithms for a new time dependent model based on level set motion for nonlinear deblurring and noise removal," *SIAM J. Sci. Comput.*, vol. 22, no. 2, pp. 387–405, 2000.

[86] G. W. Zack, W. E. Rogers, and S. A. Latt, "Automatic measurement of sister chromatid exchange frequency," *Journal of Histochemistry and Cytochemistry*, vol. 25, no. 7, pp. 741–753, 1977.

[87] D. Hearn and M. P. Baker, *Computer Graphics*. Prentice Hall, 1994.

[88] H. Breu, J. Gil, D. Kirkpatrick, and M. Werman, "Linear time Euclidean distance transform algorithms," *IEEE Trans. Pattern Analysis and Machine Intelligence*, vol. 17, pp. 529–533, May 1995.

[89] P. Perona and J. Malik, "Scale-space and edge detection using anisotropic diffusion," *IEEE Trans. Pattern Analysis and Machine Intelligence*, vol. 12, no. 7, pp. 629–639, 1990.

[90] M. J. Black, G. Sapiro, D. H. Marimont, and D. Heeger, "Robust anisotropic diffusion," *IEEE Trans. Image Processing*, vol. 7, no. 3, pp. 421–432, 1998.

[91] Z. Guo and R. W. Hall, "Parallel thinning with two-subiteration algorithms," *Commun. ACM*, vol. 32, no. 3, pp. 359–373, 1989.

[92] O. Chum, J. Matas, and J. Kittler, "Locally optimized RANSAC," *Lecture Notes in Computer Science - Pattern Recognition, Springer Berlin/Heidelberg*, vol. 2781, pp. 236–243, 2003.

[93] D. A. Forsyth and J. Ponce, *Computer Vision: A Modern Approach*. Prentice Hall, 2003.

[94] R. Burden and J. D. Faires, *Numerical Analysis*. Brooks Cole, 2000.

[95] A. Fitzgibbon, M. Pilu, and R. B. Fisher, "Direct least square fitting of ellipses," *IEEE Trans. Pattern Analysis and Machine Intelligence*, vol. 21, no. 5, pp. 476–480, 1999.

[96] G. Smirnov and V. Bushenkov, *Curso de Optimização*. Escolar Editora, 2005.

[97] T. Chan and L. Vese, "Active contours without edges," *IEEE Trans. Image Processing*, vol. 10, pp. 266–277, February 2001.

[98] L. A. Vese and T. F. Chan, "A multiphase level set framework for image segmentation using the Mumford and Shah model," *Int. J. Comput. Vision*, vol. 50, no. 3, pp. 271–293, 2002.

[99] M. Sezgin and B. Sankur, "Survey over image thresholding techniques and quantitative performance evaluation," *J. of Electronic Imaging*, vol. 13, no. 1, pp. 146–168, 2004.

[100] J. Kittler and J. Illingworth, "Minimum error thresholding," *Pattern Recognition*, vol. 19, no. 1, pp. 41–47, 1986.

[101] J. N. Kapur, P. K. Sahoo, and A. K. C. Wong, "A new method for gray-level picture thresholding using the entropy of the histogram," *Comput. Vis. Graph. Image Process*, vol. 29, no. 3, pp. 273–285, 1985.

[102] P. Sahoo, C. Wilkins, and J. Yeager, "Threshold selection using Renyi's entropy," *Pattern Recogn.*, vol. 30, no. 1, pp. 71–84, 1997.

[103] J. C. Yen, F. J. Chang, and S. Chang, "A new criterion for automatic mutilevel thresholding," *IEEE Trans. Image Processing*, vol. 4, no. 3, pp. 370–378, 1995.

[104] N. Otsu, "A threshold selection method from gray-level histograms," *IEEE Trans. Syst. Man Cybern.*, vol. 9, no. 1, pp. 62–66, 1979.

[105] S. D. Yanowitz and A. M. Bruckstein, "A new method for image segmentation," *Comput. Graph. Image Process.*, vol. 46, pp. 82–95, 1989.

[106] C. Li and C. Lee, "Minimum cross entropy thresholding," *Pattern Recogn.*, vol. 26, pp. 617–625, April 1993.

[107] C. Nicolini, A. M. Malvezzi, A. Tomaselli, D. Sposito, G. Tropiano, and E. Borgogno, "DNASER I: Layout and data analysis," *IEEE Trans. Nanobioscience*, vol. 1, no. 2, pp. 67–72, 2002.

[108] C. de Boor, *A Practical Guide to Splines*. Springer-Verlag, 1978.

[109] D. Mumford and J. Shah, "Optimal approximations by piecewise smooth functions and associated variational problems," *Communications on Pure and Applied Mathematics*, vol. 42, no. 5, pp. 577–685, 1989.

[110] Y. Zhang, R. Rohling, and D. Pai, "Direct surface extraction from 3D freehand ultrasound images," in *IEEE Visualization 2002*, pp. 45–52, 2002.

[111] M. R. Spiegel and L. Abellanas, *Fórmulas e Tabelas de Matemática Aplicada*. McGraw-Hill, 1990.